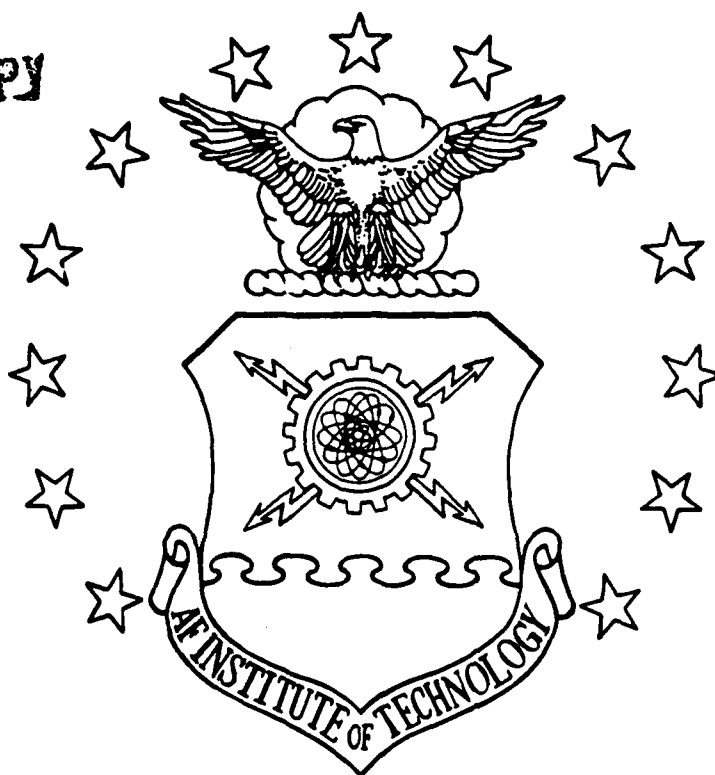AD-A216 414

Fluctuating Wind Forces Measured on a

Bluff Body Extending from a Cavity

Thesis

Brian W. King
Captain, U. S. Air Force

AFIT/GAE/ENY/89D-19

DEPARTMENT OF THE AIR FORCE

AIR UNIVERSITY

AIR FORCE INSTITUTE OF TECHNOLOGY

Wright-Patterson Air

'90 01 02 102

DTIC
ELECT
JAN 0 3 1990
S
D

Fluctuating Wind Forces Measured on a

Bluff Body Extending from a Cavity
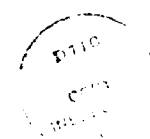
Thesis

Brian W. King
Captain, U. S. Air Force

AFIT/GAE/ENY/89D-19

AFIT/GAE/ENY/89D-19

FLUCTUATING WIND FORCES MEASURED ON A

BLUFF BODY EXTENDING FROM A CAVITY

THESIS

Presented to the Faculty of the School of Engineering

of the Air Force Institute of Technology

Air University

In Partial Fulfillment of the

Requirements for the Degree of

Master of Science in Aeronautical Engineering

Brian W. King, B. S.

Captain, USAF

December, 1989

Approved for public release; distribution unlimited

<u>A</u> Dedication

This thesis is dedicated to my beautiful and loving wife, Lauren King. As a new bride put in the middle of the AFIT experience, she has shown great patience with the late nights of study and provided the encouragement needed to make it through. I am looking forward to getting to know her again and enjoy our new life together.

Preface

In this study, I have investigated the effects of air flow over a bluff body extending from a cavity. This was a change of pace from my normal area of air breathing propulsion and proved to be a challenge.

I would like to thank my thesis advisor Lt Col Paul I. King for his guidance and for allowing me to learn from my mistakes throughout my 18 month adventure at AFIT. His encouragement had helped to keep me motivated, despite all of the complications encountered in this experimental study. In addition, I wish to thank the other members of my thesis committee, Drs. William C. Elrod and Milton E. Franke for their support. My thanks also goes out to Professor Emeritus Harold C. Larson who provided ideas for this study based on his many years of experience in tunnel testing.

Support for this project originated from the Air Force Weapons Laboratory under the guidance of Capt Thomas G. Gates. The technical and financial support was greatly appreciated.

The modal analysis of the model was conducted by graduate assistant Robert McCall. The data he generated provided a better understanding of the test results and is greatly appreciated.

Shop support cannot be over-looked either. Under the direction of Jack Tiffany, John Brohas and Joe Hofele constructed the delicate load cell unit, while Jan LeValley and Ron Ruley modified the ground board that fondly became known as the "wash tub".

In the area of logistics and technical operations, I wish to recognize Nick Yardich and his technical team of Jay Anderson, Dan Rioux,

Mark Derriso, and Tim Major for their continuing support throughout this study.

Many hours were spent in preparing this report; from software development, to calibrations and testing, and to the final data reduction. It all come together with my wife's expertise on Chiwriter word processing, and most importantly, by God's grace.

<div align="right">Brian W. King</div>

Table of Contents

List of Figures

.

List of Tables

List of Symbols

A	Reference Area of Model (8.00 in. x 8.00 in. = 64.00 in^2 = 0.444 ft^2)
A_{xy}	Moment Arm along the X or Y axis from the LCU Centroid to the Edge of the Model
A_z	Moment Arm along the Z-axis from the LCU Centroid to Load Center on Model
B_x	Moment Arm along the X-axis from Base Load Cells to LCU Centroid
B_{xy}	Moment Arm from the X-Y plane Load Cells to the LCU Centroid
B_y	Moment arm along the Y-axis from Base Load Cells to LCU Centroid
β	Angular Rotation about the Y-axis of the Tunnel Coordinates Relative to the Wind Coordinates
C	Load Cell Compression
C_{D_x}	Drag Force Coefficient
C_{D_y}	Side Force Coefficient
C_{D_z}	Lift Force Coefficient
CHK	Check Load Data File Prefix
C_{M_y}	Rolling Moment Coefficient
C_{M_y}	Pitching Moment Coefficient
C_{M_z}	Yawing Moment Coefficient
Deg F	Degrees Fahrenheit
Deg R	Degrees Rankine
$\dfrac{\delta EC_1}{\delta F_i}$	Partial Derivative of Combined Load Cell Output Voltages for Primary X Force Loading with Respect to i Axis Force (mV/lb$_f$)

$\dfrac{\delta EC_2}{\delta F_i}$ — Partial Derivative of Combined Load Cell Output Voltages for Primary Y Force Loading with Respect to i Axis Force (mV/lb_f)

$\dfrac{\delta EC_3}{\delta F_i}$ — Partial Derivative of Combined Load Cell Output Voltages for Primary Z Force Loading with Respect to i Axis Force (mV/lb_f)

$\dfrac{\delta EC_4}{\delta F_i}$ — Partial Derivative of Combined Load Cell Output Voltages for Primary X Moment Loading with Respect to i Axis Force (mV/lb_f)

$\dfrac{\delta EC_5}{\delta F_i}$ — Partial Derivative of Combined Load Cell Output Voltages for Primary Y Moment Loading with Respect to i Axis Force (mV/lb_f)

$\dfrac{\delta EC_6}{\delta F_i}$ — Partial Derivative of Combined Load Cell Output Voltages for Primary Z Moment Loading with Respect to i Axis Force (mV/lb_f)

$\dfrac{\delta EC_1}{\delta M_i}$ — Partial Derivative of Combined Load Cell Output Voltages for Primary X Force Loading with Respect to i Axis Force $(mV/in-lb_f)$

$\dfrac{\delta EC_2}{\delta M_i}$ — Partial Derivative of Combined Load Cell Output Voltages for Primary Y Force Loading with Respect to i Axis Force $(mV/in-lb_f)$

$\dfrac{\delta EC_3}{\delta M_i}$ — Partial Derivative of Combined Load Cell Output Voltages for Primary Z Force Loading with Respect to i Axis Force $(mV/in-lb_f)$

$\dfrac{\delta EC_4}{\delta M_i}$ — Partial Derivative of Combined Load Cell Output Voltages for Primary X Moment Loading with Respect to i Axis Force $(mV/in-lb_f)$

$\dfrac{\delta EC_5}{\delta M_i}$ — Partial Derivative of Combined Load Cell Output Voltages for Primary Y Moment Loading with Respect to i Axis Force $(mV/in-lb_f)$

$\dfrac{\delta EC_6}{\delta M_i}$ — Partial Derivative of Combined Load Cell Output Voltages for Primary Z Moment Loading with Respect to i Axis Force $(mV/in-lb_f)$

ΔEC — Change in Load Cell Output Voltage (mV)

E — Load Cell Voltage Output (mV)

EC_1	Combined Load Cell Output Voltages for Primary X Force (mV)
EC_2	Combined Load Cell Output Voltages for Primary Y Force (mV)
EC_3	Combined Load Cell Output Voltages for Primary Z Force (mV)
EC_4	Combined Load Cell Output Voltages for Primary X Moment (mV)
EC_5	Combined Load Cell Output Voltages for Primary Y Moment (mV)
EC_6	Combined Load Cell Output Voltages for Primary Z Moment (mV)
f	Frequency (Hz)
f_{F_y}	Side Load Force Frequency (lb_f)
F_{LC}	Individual Load Cell Force (lb_f)
F_x	Drag Force (lb_f)
F_{xy}	X or Y Force applied to model to create a Z Moment (lb_f)
F_y	Side Force (lb_f)
F_z	Lift Force (lb_f)
45C	45RO Configuration Data File Prefix
45RO	45 Degree Rotation Configuration
g	Acceleration Due to Gravity (32.174 ft/s^2)
γ	Angular Rotation about Z' axis of the LCU Coordinates Relative to Tunnel Coordinates; Specific Heat Ratio
h	The Barrier Width for Strouhal Number (Blockage Width of Model Perpendicular to the Wind)
h_{man}	Height of Manometer Fluid (Inches of Water)
i	Axis of Loading Moment Subscript (X, Y, or Z)
in-lb_f	Moment Units of and Inch-Pound Force

ℓ	Width of Model (8.00 in = 0.6667 ft)
lb_f	Pounds Force
lb_m	Pounds Mass
LCP	Load Cell Point of Loading
LCU	Load Cell Unit
LSB	Least Significant Bit
M	Mach Number; Moment
mV	Millivolts
M_x	X Moment
M_y	Y Moment
M_z	Z Moment
NORO	No-Rotation Configuration
P_{Bar}	Barometric Pressure (lb_f/ft^2)
P_{Static}	Static Pressure (lb_f/ft^2)
P_{Total}	Total Pressure (lb_f/ft^2)
ρ_{Air}	Density of Air ($lb_f s^2/ft^4$)
ρ_{man}	Density of Manometer Fluid (lb_m/ft^3)
q, Q	Dynamic Pressure (lb_f/ft^2)
q_{local}	Local Dynamic Pressure (lb_f/ft^2)
q_{tunnel}	Tunnel Dynamic Pressure (lb_f/ft^2)
R	Gas Constant for Air (1721.39 ft^2/Deg R s^2)
Re	Reynolds Number
S	Strouhal Number; Load Cell Shear Load

T	Load Cell Tension
T_{Static}	Static Temperature (Deg R)
T_{Total}	Total Temperature (Deg R)
V	Volts; Velocity (ft/s)
VEL	Velocity (ft/s)
W	Blockage Width for the Strouhal Number (NORO Configuration = 8.00 in = 0.6667 ft)
X, Y, Z	Tunnel Coordinates
X', Y', Z'	LCU Coordinates
X", Y", Z"	Wind Coordinates
00C	NORO Configuration Data File Prefix

AFIT/GAE/ENY/89D-19

Abstract

The effect of wind forces measured on a bluff body extending from a cavity was investigated. This was accomplished by measuring wind induced vibratory inputs to a plexiglas bluff body model. The model extended from a ground board cavity installed in the AFIT 5-Foot Wind Tunnel.

Forces and moments were measured from an 8 element load cell unit (LCU) built and installed in the base of a plexiglas model. Three different size cavity openings were tested for both a no-rotation and 45 degree rotation referenced to the wind. Data was taken at individual speed points between 55 ft/s and 180 ft/s, producing Reynolds number based on model width in the range of 1.5×10^5 to 5.0×10^5. Baseline data for a closed cavity configuration was collected and compared to previous studies conducted at the USAF Academy. Force and moment coefficient data are presented, comparing cavity opening and model rotation effects. Results of shedding frequency analysis are presented based on transient data recorded.

xviii

I. Introduction

Air flow around bluff bodies is commonplace in our everyday lives, from wind blowing past the buildings we work in, to the drag forces on a moving truck. The study of incompressible fluid flow around bluff bodies is important to the understanding of problems in man-made structures exposed to surface winds. The collapse of the Tacoma Narrows Bridge in Seattle, Washington is one of the most famous examples of a structural design in which fluid-structural interaction was of real importance, but not adequately taken into account.

The Air Force Weapons Laboratory has an interest in the fluctuating wind forces on a bluff body building intended to house a land-based telescope. The desire is to predict the vibratory loadings on the building in order to develop dampening systems to prevent telescope vibrations. In the search for existing data, many studies were found to have been conducted in the area of air flow over bluff bodies.

The majority of the previous studies conducted on flow over bluff bodies have dealt with turbulent flows over two-dimensional bodies. These turbulent flows are actual boundary layer profiles designed to simulate atmospheric surface winds. In a report by Vickery (1:481-494) the effects of large-scale turbulence in the flow field were shown to have a significant impact on both the mean and fluctuating forces acting on a long cylinder of square cross section. The impact on the fluctuating side loads was a reduction of about 50% over values for the uniform flow case. Other two-dimensional studies have dealt with flat plate bluff bodies attached to flat walls. These studies included infinite

1

width plates mounted perpendicular to a wall (2:1126-1133), infinite width plates mounted at an angle to a wall (3:71-78), and finite width plates attached perpendicular to a wall (4:98-104). Information on drag pressures and vortex shedding are available from these flat plate studies; however, not in regards to side loadings on the structures.

Information on the vibratory side loadings is more prevalent in the studies involving three dimensional bodies. In a study by Castro and Robins (5:301-335), results for both uniform and turbulent flows over a cube are presented. This data includes mean surface pressures on the cube along with the mean and fluctuating velocities in its wake; however, no correlation between fluctuating velocities and force input to the body is given. A similar study was conducted by Sakamoto and Arie (6:275-293), producing time averaged data for the pressure distributions around the cube while varying the cube's rotation angle relative to the wind. Again, these results do not lead to force fluctuations with time on the bluff body.

Since the needed data was not found from these previous works, the Air Force Weapons Laboratory conducted a test to characterize the vibration input to a body due to wind loads. This testing was conducted at the United State Air Force (USAF) Academy, Colorado Springs, Colorado (7:1-12). In this study, force and moment data was acquired for several three dimensional bluff body shapes tested in the subsonic wind tunnel. Models were mounted on a 6-element sting balance extending from the flat floor of the tunnel. The primary model was an 8 inch cube with square corners. Results were presented as a function of the Strouhal number

and as force and moment coefficients versus tunnel speed. A difficulty encountered during the USAF Academy testing was the excitation of the model's natural frequency. As airflow velocity is increased, over a bluff body model, the shedding frequency from the model increases. A synchronization with the model's natural frequencies can occur when the shedding frequencies match the natural frequency. Once these frequencies are synchronized, the model will tend to vibrate at this excited frequency, locking on to the frequency value. When this "lock-on" occurs, increases in shedding frequencies can not be detected from the model. Thus, representation of the true shedding frequencies in the USAF Academy test data may be questionable at speeds producing shedding vortices at a frequency close to the model natural frequencies.

The objective and scope of this thesis was to characterize the vibration input to a bluff body similar to the USAF Academy test, with the additional parameter of a variable size cavity around the bluff body model. Three cavity configurations were tested at two different model rotation (0 and 45 degrees). The first series of tests were conducted on the three no-rotation (NORO) configurations where the model faces were normal and parallel to the flow. Three 8 inch deep cavity inserts were used, starting with a 1/4 inch gap size (closed configuration), then moving to the 4 inch and 8 inch cavities. After the NORO configuration testing, the cavity and model assembly was rotated 45 degrees to the wind creating the 45RO configuration. Again, all three inserts were tested, starting with the closed configuration.

3

Force and moment data depicting the vibration inputs to a bluff body were measured from an 8×8×16 inch (length × width × height) plexiglas model mounted in the cavity. An 8-element load cell unit (LCU) was mounted in the base of the plexiglas model to provide the loading information. This loading information was recorded in transient format and processed as both mean and standard deviation values. Air flow speeds around the model ranged from 55 ft/s to 180 ft/s, producing Reynolds numbers based on model width in the range of 1.5×10^5 to 5.0×10^5.

II Theory

As mentioned in Chapter I, many structures in our everyday lives have the non-aerodynamic shape of a bluff body. The fluid flow separation from the aft portion of these structures and the induced forces on these structures depend on parameters such as velocity of the fluid and abruptness of the contour.

In studying flow over a bluff body, one should have an understanding of flow over a circular cylinder due to the similarities in flow separation and vortex formation. Figure 2.1 is an example of flow over a cylinder for various Reynolds numbers (8:29-8). The Reynolds number is used to non-dimensionalize the effects of fluid viscosity, model size, and fluid velocity. At low Reynolds values, flow remains attached to the body and the wake is steady and parallel to the flow. As the Reynolds number increases, the disturbances in the wake become more prevalent. Vortices alternately form and shed from the aft contours of the body, resulting in the familiar downstream Von Karman vortex street. As these vortices shed from the bluff body, side loads are transmitted to the body, lending to wind-induced oscillations.

In the case of flow over a square cylinder bluff body, So and Savkar (9:399) state there are two features which render such a flow significantly different from the circular cylinder case. First, the point of separation on the square cylinder is generally fixed even though such cylinders are prone to separation with reattachment prior to full separation. However, this behavior is not as much a function of Reynolds number as is the case with the circular cylinder where such

5

VIBRATION OF STRUCTURES INDUCED BY FLUID FLOW

$Re < 5$ REGIME OF UNSEPARATED FLOW

$5\ TO\ 15 < Re < 40$ A FIXED PAIR OF FÖPPL VORTICES IN WAKE

$40 < Re < 90\ AND\ 90 < Re < 150$ TWO REGIMES IN WHICH VORTEX STREET IS LAMINAR

$150 < Re < 300$ TRANSITION RANGE TO TURBULENCE IN VORTEX

$300 < Re \gtrsim 3 \times 10^5$ VORTEX STREET IS FULLY TURBULENT

$3 \times 10^5 < Re < 3.5 \times 10^6$

LAMINAR BOUNDARY LAYER HAS UNDERGONE TURBULENT TRANSITION AND WAKE IS NARROWER AND DISORGANIZED

$3.5 \times 10^6 < Re$

REESTABLISHMENT OF TURBULENT VORTEX STREET

Reference (8:29-8)

Figure 2.1 Regimes of Fluid Flow Across Circular Cylinders

6

behavior is sometimes observed in transition flows. Second, the square cylinder can be rotated relative to the wind, creating a steady lift force due to the asymmetric flow around the cylinder not seen in the circular case. Despite these differences, the bluff body still produces the shedding vortices as seen in the circular cylinder case.

The first experimental observation of the shedding phenomenon was conducted in 1878 by Strouhal. From his experimental results, Strouhal derived a relationship between the shedding frequency of a vibrating wire in the wind to the wind velocity and wire diameter. This relation is known as the Strouhal number, and is defined as:

$$S = \frac{f\ h}{V} \tag{2.1}$$

where S is the Strouhal number, h the barrier width, f the shedding frequency, and V the mean free stream velocity (10:14-17). For circular cylinders, square cylinders, and most bluff body sections, the Strouhal number generally falls in the range of 0.14 to 0.25 (8:29-7).

The primary goal of this thesis is the characterization of these wind-induced force vibrations, particularly for a cube shape extending from an open cavity. The parameters used for this characterization include the Strouhal number equation (2.1) along with force and moment coefficients. Force coefficients are defined as:

$$C_{D_i} = \frac{F_i}{q_{local}A} \tag{2.2}$$

where q_{local} is the local mean dynamic pressure, F the applied load, i the axis of loading (X, Y, or Z), and A the model reference area. The

7

reference area chosen for this research is the frontal area of the model, as suggested in Hoerner (11:1-9). This choice also coincides with definitions used in the study at the USAF Academy (7:1-12). Thus, when the square model is rotated 45 degrees to the wind, the reference area becomes 1.414 times the head-on reference area of 0.444 square feet.

In a similar manner, the moment coefficients are defined as:

$$C_{M_i} = \frac{M_i}{q_{local} A \ell} \tag{2.3}$$

where q_{local} and A are defined as in equation (2.2), M is the applied moment, i the moment axis (X, Y, or Z), and ℓ the model width.

The q_{local} values for equations (2.2) and (2.3) are converted from the three pitot-static probes mounted in front of the model. These values are measured in inches of water and then converted to units of pressure using the integrated form of Bernoulli's equation for steady frictionless flow of an incompressible fluid (12:112). This form of Bernoulli's equation is given by

$$\frac{P_1}{\rho} + \frac{V_1^2}{2} + gh_1 = \frac{P_2}{\rho} + \frac{V_2^2}{2} + gh_2 = constant \tag{2.4}$$

where the subscripts designate station points 1 and 2 along a uniform streamline. Applying equation (2.4) to the static conditions of the U-tube manometer connected to the pitot-static probe results in the familiar manometer equation

$$P_{Total} - P_{Static} = g \, \rho_{man} \Delta h_{man} \tag{2.5}$$

8

which also defines the local equal to the dynamic pressure. Thus,

$$q_{local} = g \, \rho_{man} \Delta h_{man} \qquad (2.6)$$

The manometer fluid density ρ_{man} for each of these equations is a function of the manometer room temperature.

Local velocities used in this thesis are determined through an iterative process based on the local q values calculated from (2.6). The first step of this process is the calculation of a local air density, ρ_{Air}. The assumption used in this calculation is that there are no inlet losses in the tunnel, thus the tunnel total pressure is equal to the barometric pressure. Using the corrected barometric pressure read from the tunnel mercury barometer and the total temperature measured at the tunnel inlet, air density is calculated from the Ideal Gas Law,

$$\rho_{Air} = \frac{P_{Total}}{R \, T_{Total}} = \frac{P_{Bar}}{R \, T_{Total}} \qquad (2.7)$$

where:

$$P_{Total} = P_{Bar} = \text{Barometric Pressure inch Hg (Corrected)}$$
$$\times \left(\frac{70.704 \; lb_f/ft^2}{inch \; hg} \right)$$

$$R = 1721.39 \; \frac{ft^2}{s^2 Deg \, R}$$

and,

$$T_{Total} = \text{Tunnel Temperature (Deg F)} + 459.67$$

The next step is the calculation of an initial velocity based on equation (2.4) using q_{local} and the assumed density from equation (2.7).

$$V = \sqrt{\frac{2 \, q}{\rho_{Air}}} \qquad (2.8)$$

9

After calculating this initial velocity, isentropic relationships are used to arrive at a new ρ_{Air} value based on static properties. These calculations start with the Mach Number

$$M = \frac{V}{\sqrt{\gamma R T_{Total}}} \qquad (2.9)$$

where

$$\gamma = 1.4$$

Once the Mach number is calculated, the static properties of pressure and temperature are found using

$$T_{Static} = \frac{T_{Total}}{\left[1 + \frac{\gamma - 1}{2} M^2\right]} \qquad (2.10)$$

and

$$P_{Static} = P_{Total} - \frac{\rho_{Air} V^2}{2} \qquad (2.11)$$

From these static properties, a new air density is given by

$$\rho_{Air} = \frac{P_{Static}}{R \, T_{Static}} \qquad (2.12)$$

The final step for the local velocity calculation is to use this new air density value in equation (2.8), arriving at the velocity used in this thesis.

If the density iteration defined by equations (2.9) through (2.12) is not used, then the induced error on the velocity measurement is still less than 1/2 percent. However, since the equations are easy enough to program, the iteration is included for the data processing in order to eliminate this minor error.

10

III EXPERIMENTAL HARDWARE

This chapter includes details of the experimental hardware. Included are separate sections describing the AFIT 5-Foot Wind Tunnel, the ground board and cavity, plexiglas model, load cell unit (LCU), instrumentation, and the data acquisition system.

AFIT 5-Foot Wind Tunnel

The AFIT 5-Foot Wind Tunnel was constructed in 1919 at McCook Field in Dayton, Ohio (13:1-5). It has a circular test section 5 feet in diameter, 18 feet long, and is constructed entirely of wood. The entrance contraction ratio is 3.7 to 1. The tunnel is open at both ends and is located inside a large building which serves as both inlet plenum and a discharge chamber (see Fig. 3.1).

The flow is driven by two 12 foot counter-rotating fans each powered by two 400-horsepower DC electric motors. The tunnel is capable of velocities up to 293 ft/sec for a maximum unit Reynolds number of approximately 1.878×10^6/ft. Total pressure is atmospheric, and static pressure is measured by a manifold containing eight static ports, 30 inches downstream from the tunnel entrance and 6.5 feet upstream of the test section. Dynamic pressure is measured by a micromanometer and is controlled by varying the speed of the DC motors driving the fans.
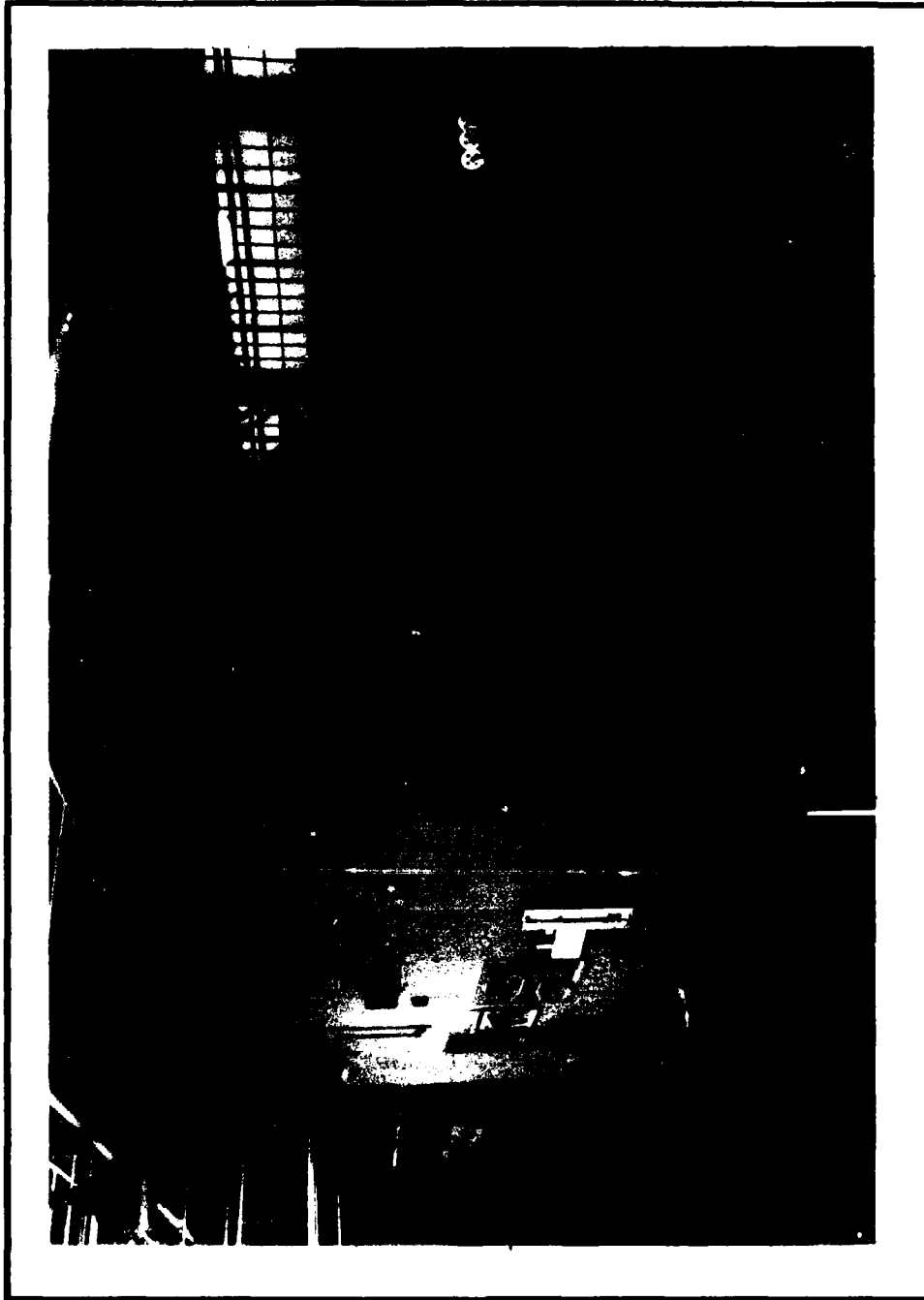
Figure 3.1 AFIT 5-Foot Wind Tunnel

Ground Board and Cavity

Figures 3.2 and 3.3 are front view pictures of the ground board and cavity assembly installed in the AFIT 5-Foot Wind Tunnel. The ground board provided the flat test section and means to install the cavity. This ground board was modified from a previous thesis study in the AFIT 5-Foot Wind Tunnel by U.S. Army Major Laywn C. Edwards. The modifications included the installation of a 34 inch diameter cavity, three pitot-static tube mounts up stream of the cavity, and a 12 x 48 inch adjustable flap near the trailing edge. The following paragraphs describe these changes.

The original ground board was made from 3/4 inch plywood board reinforced to 1.5 inches at the edge and tapered from the top surface width of 57 inches to a narrower width to accommodate the radius of the tunnel walls. An elliptical leading edge was used to reduce turbulence levels as the stream lines separate between the upper and lower portions of the tunnel. This leading edge is a 4:1 elliptic shape machined from 2x4's and glued to the leading end of the ground board. Figure 3.4 is a cutaway view of the modified ground board and cavity assembly. Modification of the ground board started with a 36 inch diameter hole centered 42.5 inches back from the leading edge. A 1 inch groove was routed along the top edge of this hole to provide a 1 inch lip to support the cavity unit. The bottom side of this lip was reinforced with a 2 inch wide, 1/4 inch thick, aluminum ring screwed and epoxied to the ground board.

13
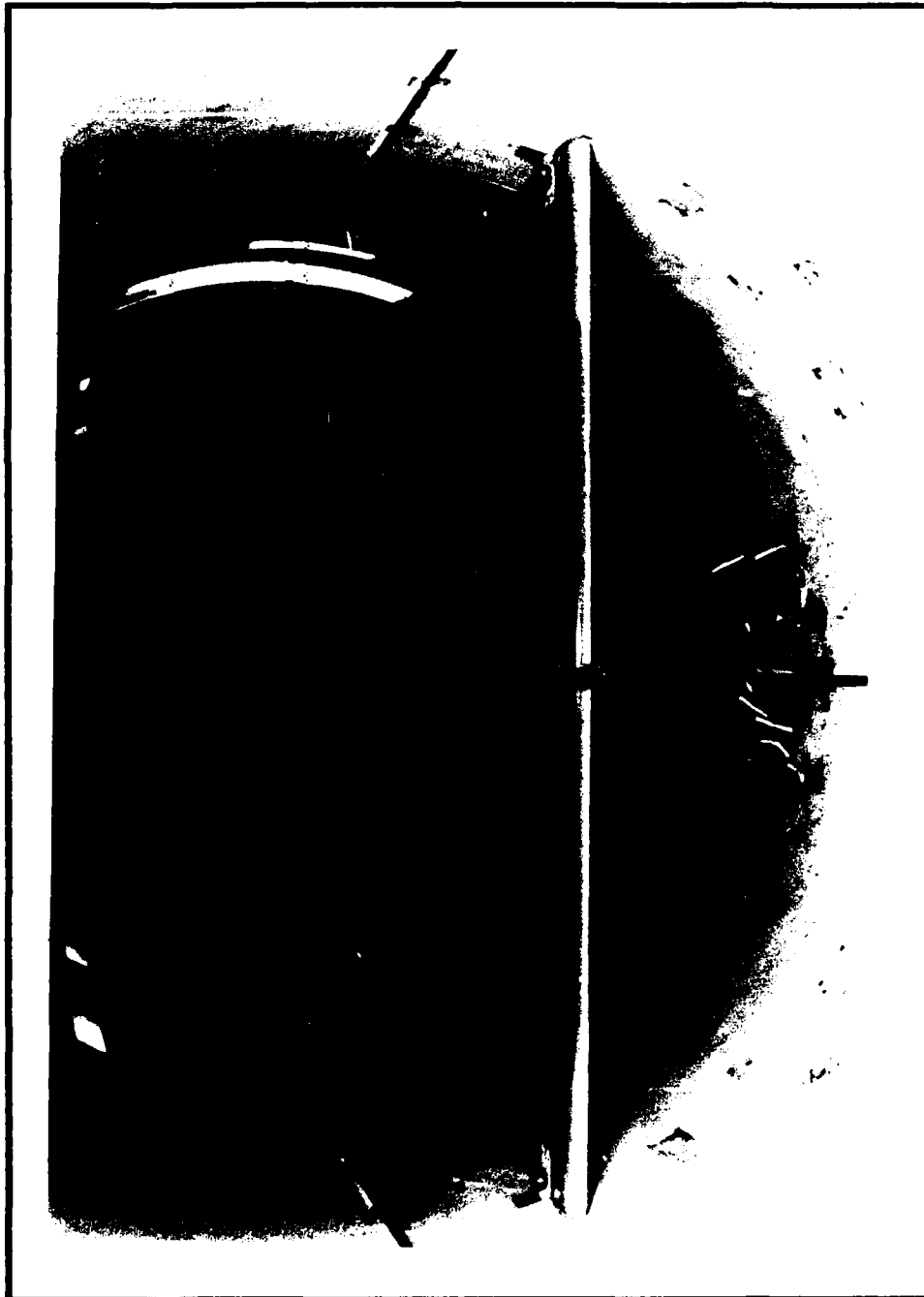
Figure 3.2 Front View of Ground Board and Cavity Assembly in AFIT 5-Foot Wind Tunnel (Top Half)

Figure 3.3 Front View of Ground Board and Cavity Assembly in AFIT 5-Foot Wind Tunnel (Bottom Half)

Plexiglas Model

Slider Ring

Plywood
Ground Board

Aluminum Support
Ring

Nylon Spacer
on Support
Lip

Aluminum Cavity

Load Cell Unit

LCU Steel Base
Plate

Steel Base
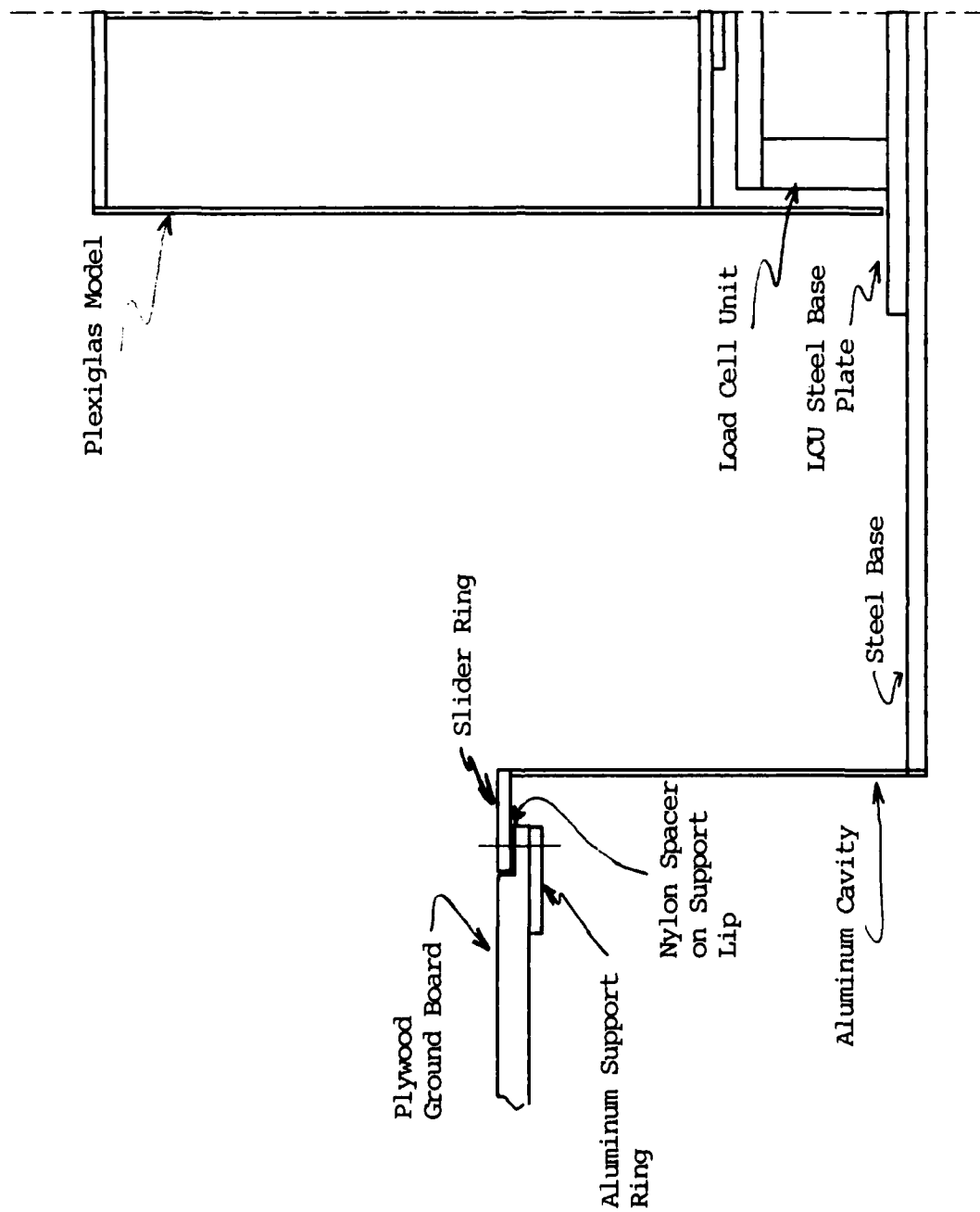
Figure 3.4 Outaway Cross Section of Ground Board and Cavity Assembly

The cavity unit, as seen extending from the bottom of the ground board in Figure 3.3, is a 34 inch inner diameter aluminum and steel "wash tub". Side walls are 1/8 inch thick aluminum approximately 8.5 inches high, attached to a 3/8 inch steel base. A 2 inch wide slider ring is attached to the top of the cavity sides, serving to support the cavity in the ground board (see Figure 3.4). The cavity is held in place by 1/4 inch flat head screws which pass through this slider ring and thread into the aluminum support ring. The 3/8 inch steel base of the cavity was Blanchard ground flat and parallel to a ± 0.001 inch tolerance, thus providing the LCU with a non-distorting surface to mount.

Three different inserts to the ground board cavity are available, ranging from the closed configuration (actually a 1/4 inch gap on all sides) to 4 inch and 8 inch cavity configurations. These cavity inserts provide a squared cavity, parallel with the faces of the model from top to bottom. Figure 3.5 shows how the inserts are installed.

The ground board is attached to the tunnel in six locations. Four brackets are used to clamp the ground board corners to the tunnel walls as seen in Figure 3.6. Two remaining attachments connect the base of the cavity and back end of the ground board to the tunnel floor using jackscrew assemblies (Figure 3.7). Both jackscrew assemblies consist of a ball-and-socket joint attached to the board and a pivoting base plate. These joints allowed for the minor axial misalignments encountered during installation.

17
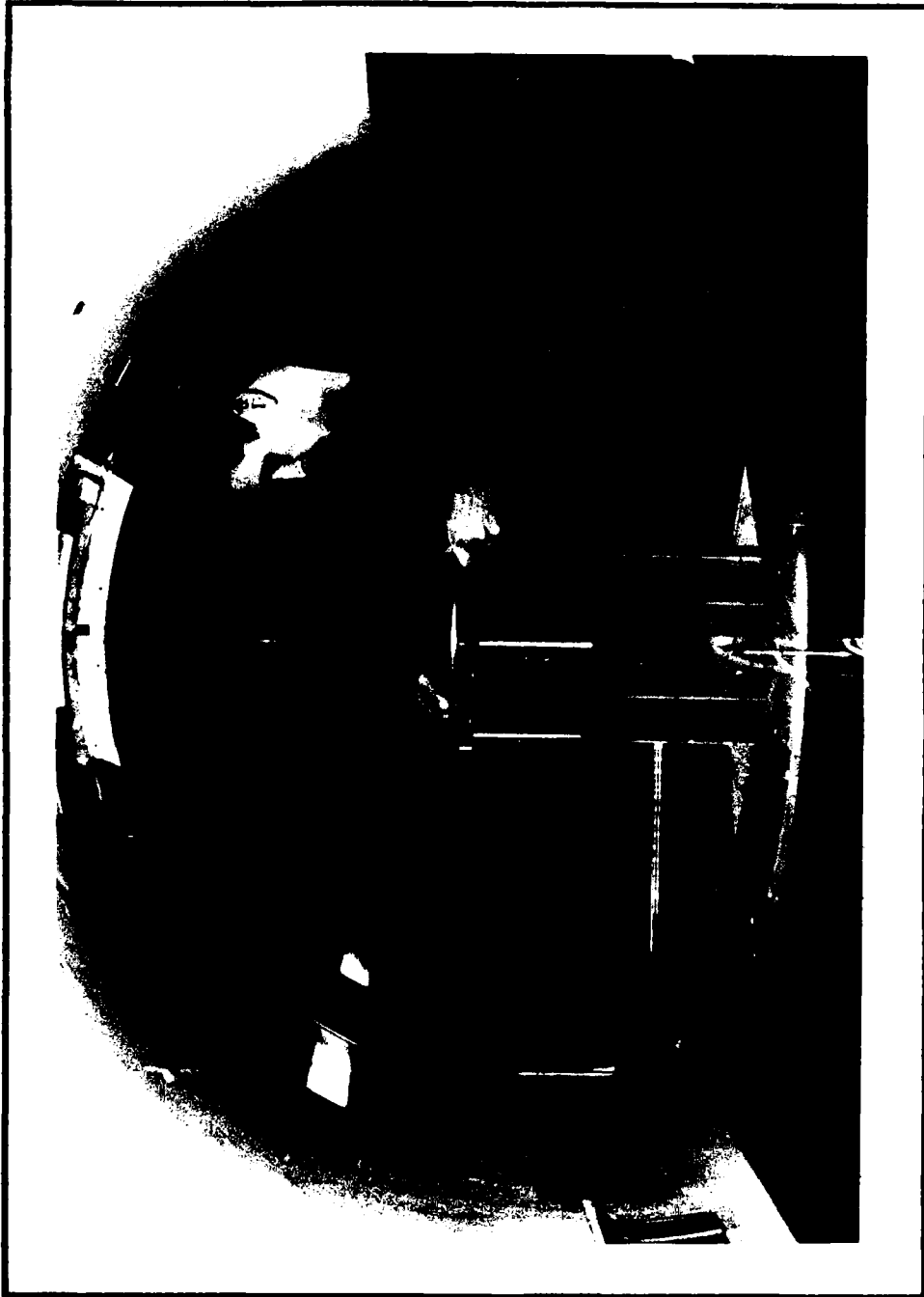
Figure 3.5   Author Installing Cavity Insert
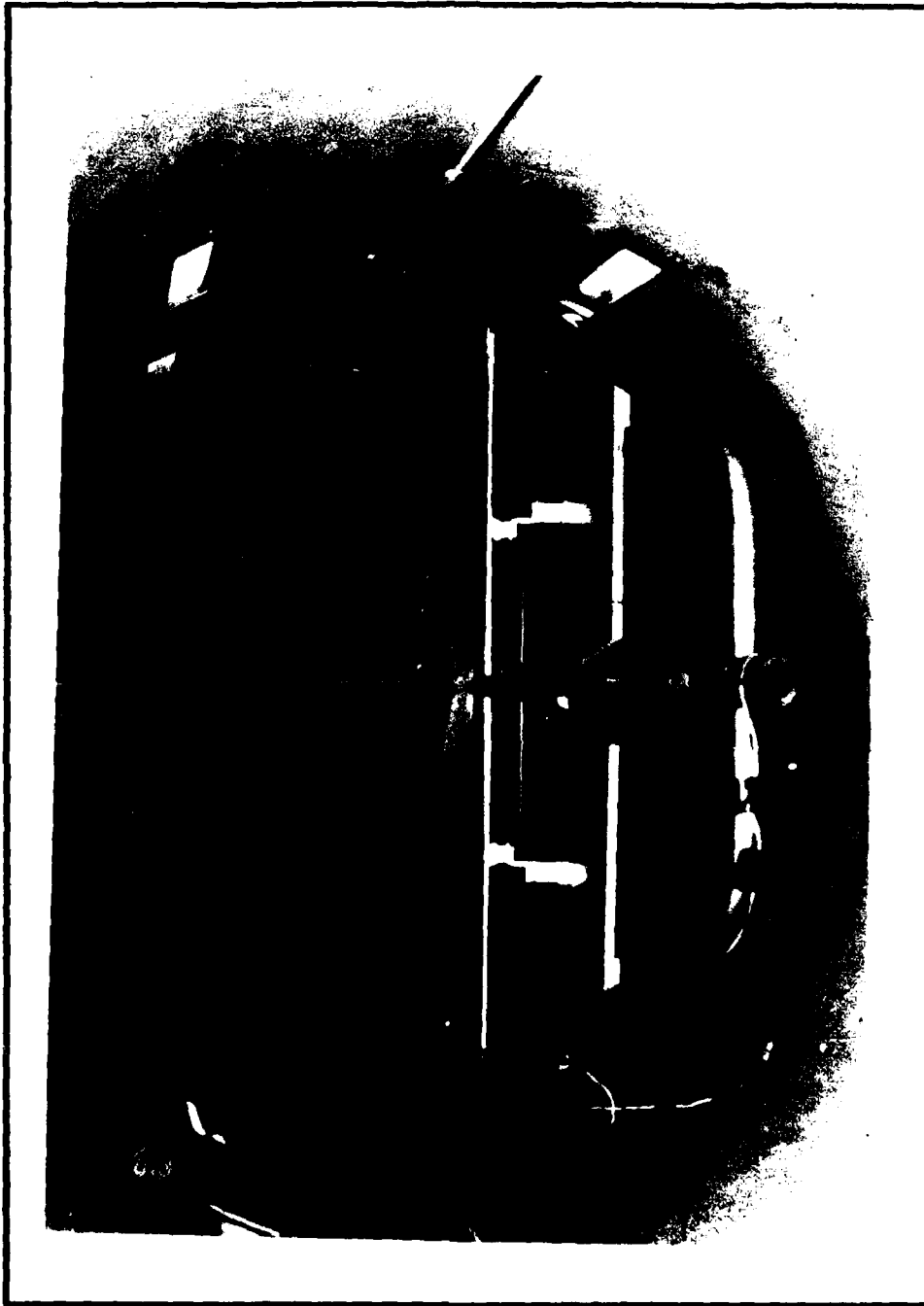
Figure 3.6 Aft View of Ground Board and Cavity Assembly in AFIT 5-Foot Wind Tunnel (Top Half)
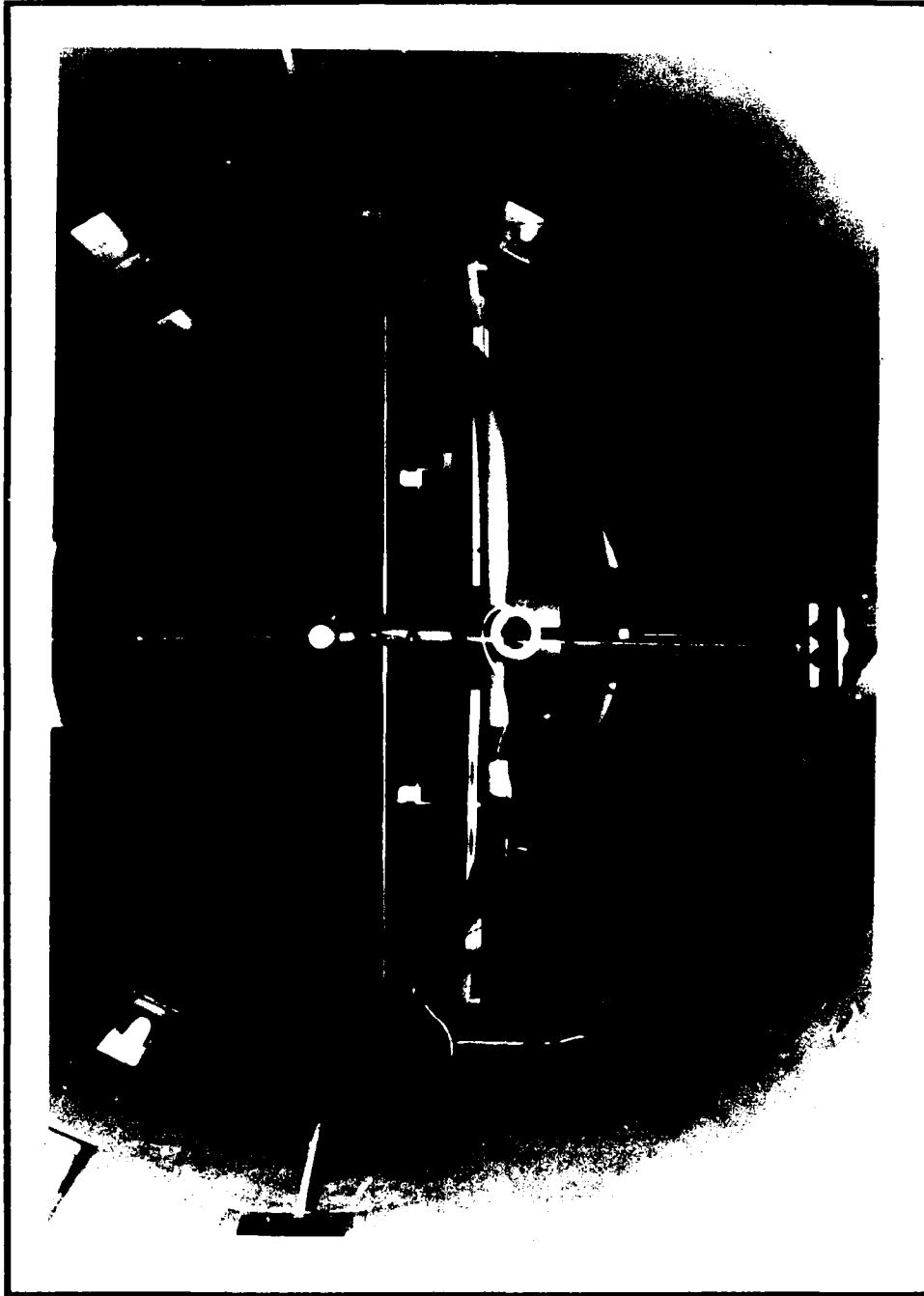
Figure 3.7 Aft View of Ground Board and Cavity Assembly in AFIT 5-Foot Wind Tunnel (Bottom Half)

In order to accommodate the installation of three pitot-static probes in front of the cavity, three holes were drilled through the ground board allowing installation of mounting taps. The three probes are spaced 6 inches apart along a line perpendicular to the center line, approximately 6 inches upstream of the inside lip of the cavity (See Figure 3.8).

Blockage on the bottom side of the ground board is approximately 11%. To compensate for this blockage and prevent streamline distortion, a trailing edge flap was added to the top side of the ground board. The flap is made from 3/8 inch aluminum plate and attaches to the ground board with a piano hinge and two "1/4 moon" sliders which pass through the board. These sliders are machined from 3/8 inch aluminum with a center travel slot. Two mounting blocks attached to the board serve to guide the sliders and provide a locking surface for angle setting. Figure 3.9 shows this flap configuration.

Model

Figure 3.10 shows the lightly sanded plexiglas cube model mounted to the calibration bench. The model outside dimensions are 8.0 x 8.0 x15.62 inches (length x width x height). All walls and interior structure are made of 1/8 inch thick plexiglas, with both the top and base plate being 1/4 inch plexiglas. Two interlocking ribs provide internal stiffness to the side panels between the top and base plates. The base plate is located 3.4 inches from the bottom edges of the model. This creates a cavity in the base of the model structure for installation of the load cell unit (LCU). All forces and moments are transmitted from
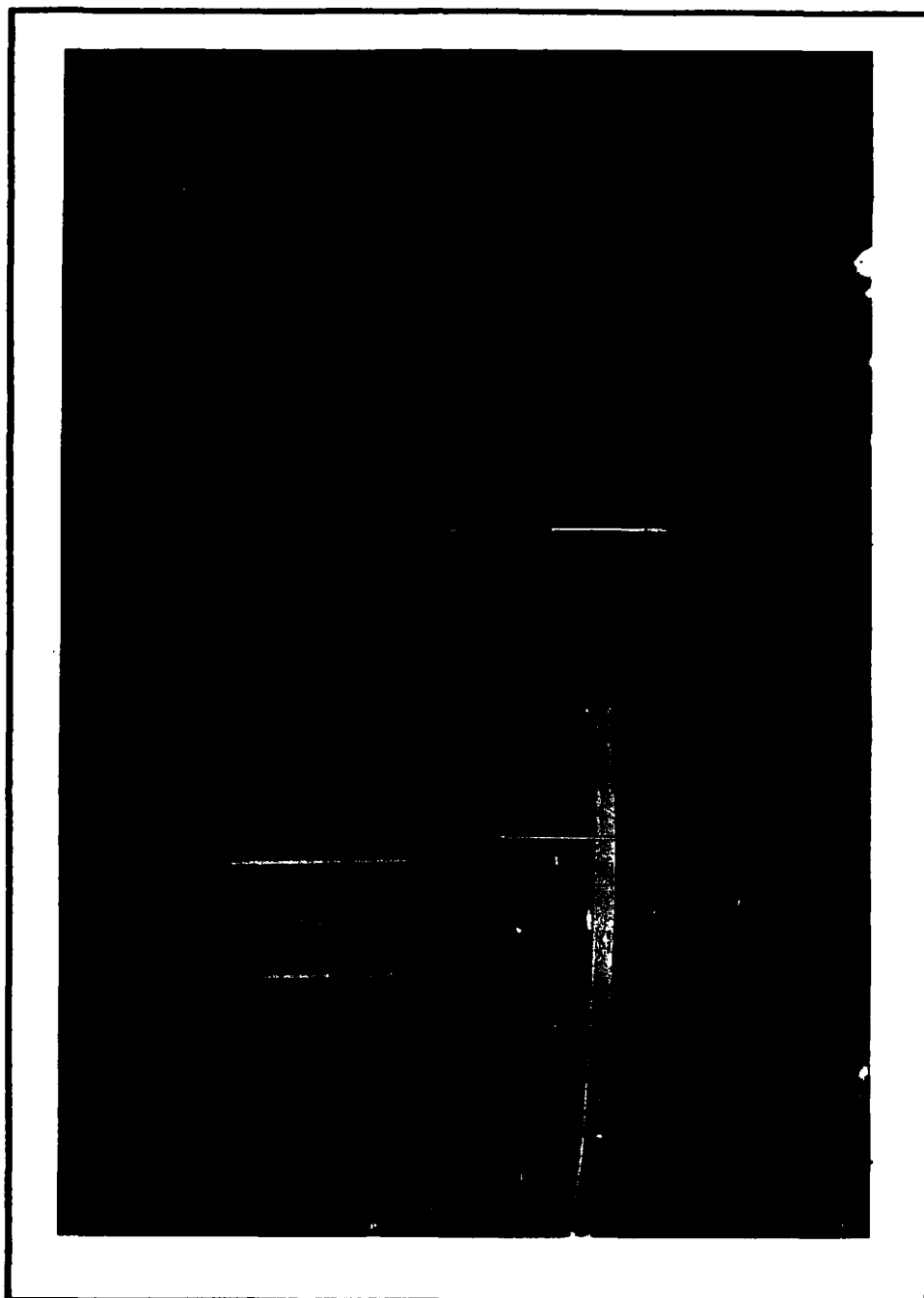
Figure 3.8 Pitot-Static Tubes In Front of Model (4 Inches above Ground Board)

22

Flap

Piano Hinge

Ground Board

$\frac{1}{4}$ Moon Slider

Lock Block
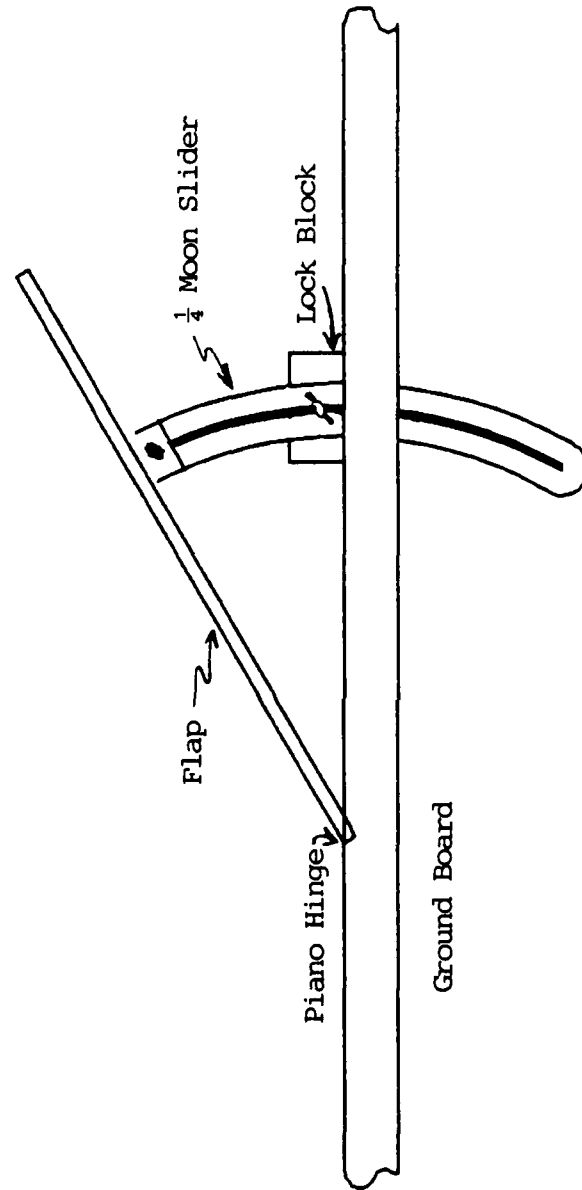
Figrue 3.9   Side View of Ground Board Flap Assembly

23
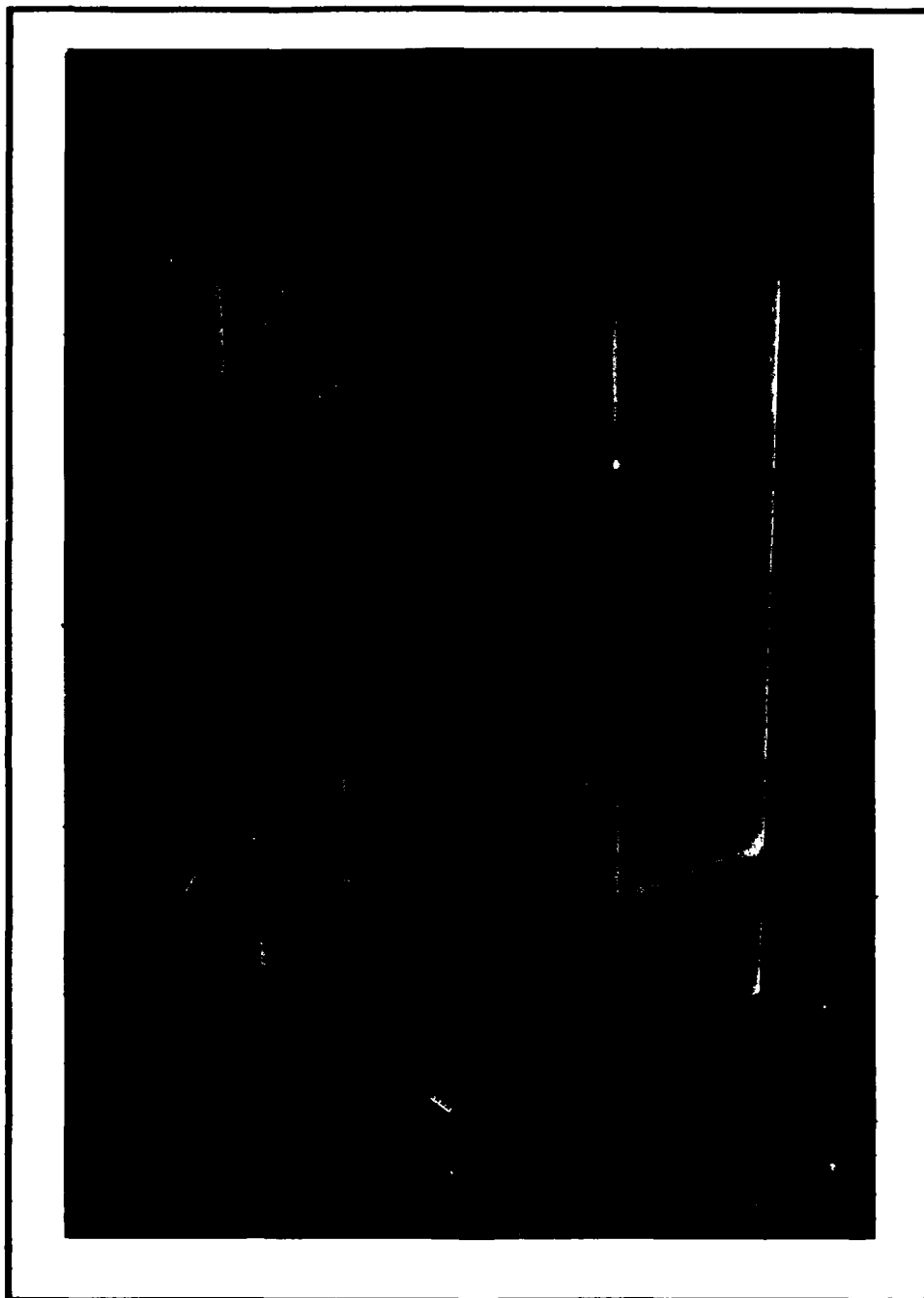
Figure 3.10   Plexiglas Cube Model

24

the model to the LCU through the base plate. Four symmetrical 1/4-28 flathead screws are used to connect the model to the LCU. Since the entire model was glued together, the four cavities created by the internal rib structure required venting. This was achieved by drilling small vent holes through the axial centers of the mounting screws.

The plexiglas material was selected to provide a light weight model with a high natural frequency modes, in an attempt to avoid modal excitations in the low frequency regions of interest.

Load Cell Unit (LCU)

Figure 3.11 is a picture of the assembled LCU detached from the model. The LCU consists of eight Interface SM-25 load cells to measure the six force and moment components of the model. Eight load cells were used in this design to provide symmetric loading on the individual load cells. In the upper X-Y plane of the LCU (Figure 3.12), four load cells are configured to measure the X and Y forces as well as the Z moment. Two load cells measure the X-forces, two measure the Y forces, and all four measure the Z-moment. The four remaining load cells act as legs to support the X-Y load cell plane and measure the primary Z force along with X and Y moments (Figure 3.13). These base load cells attach to a 12×12 inch base plate for mounting in the cavity. Due to the interactive nature of this LCU, forces and moments are measured not only by their primary load cells, but also by the secondary contributions of the other load cells. Details of this interaction and how it is handled is provided in Appendix A.

25
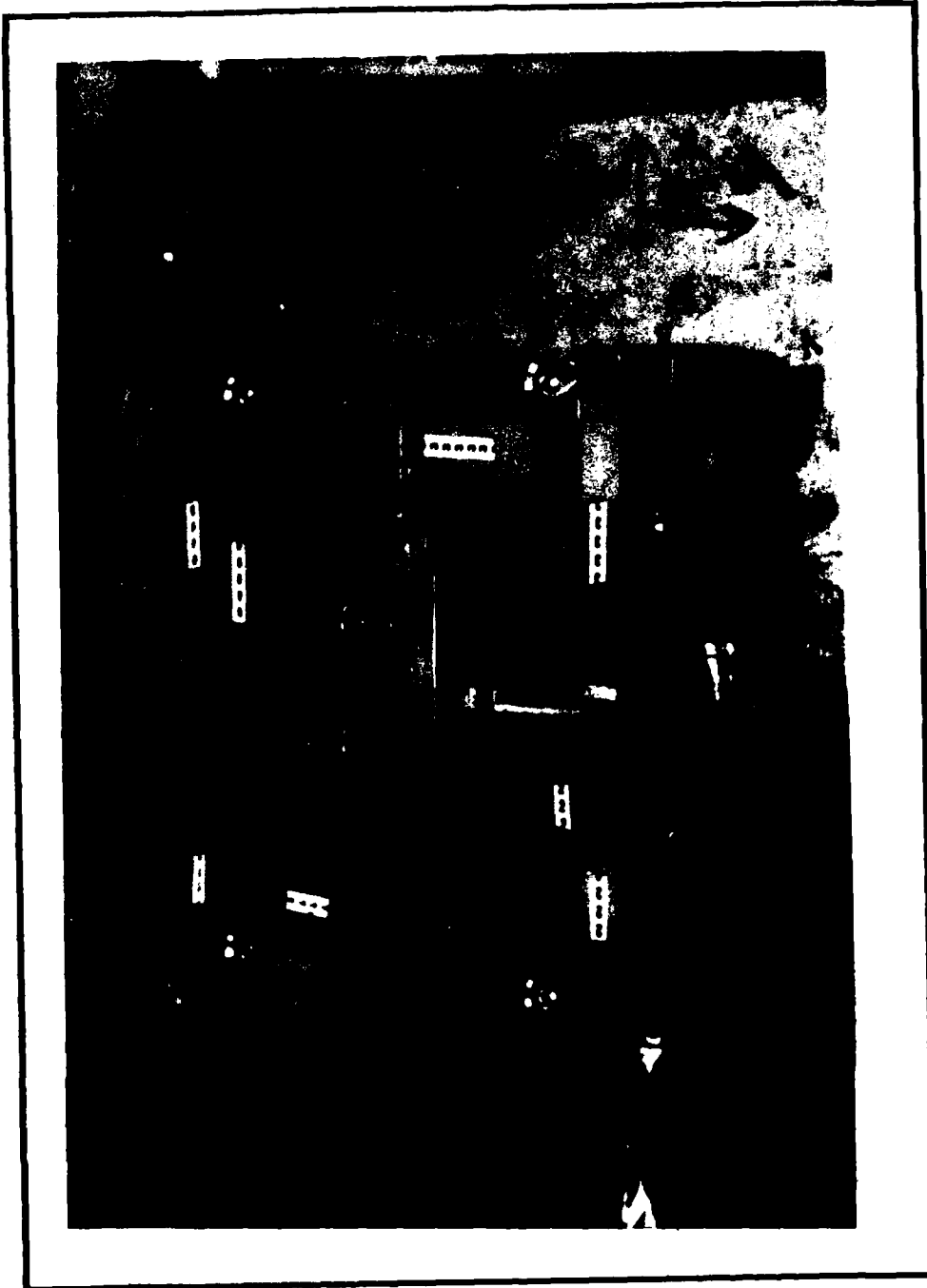
Figure 3.11 Assembled Load Cell Unit (LCU)
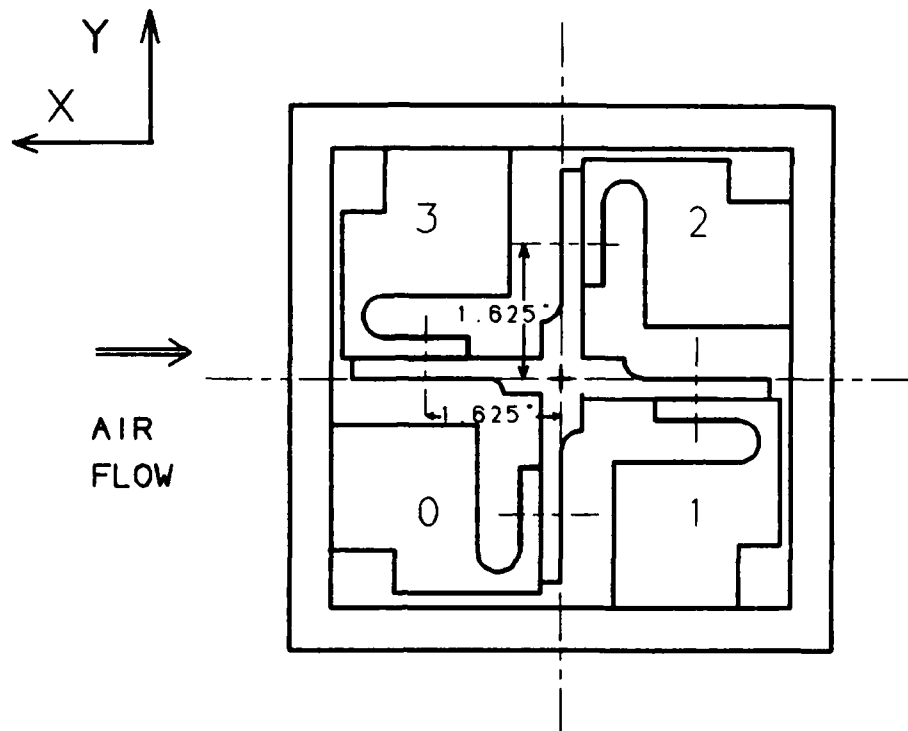
Figure 3.12 Coordinates of LCU X-Y Plane
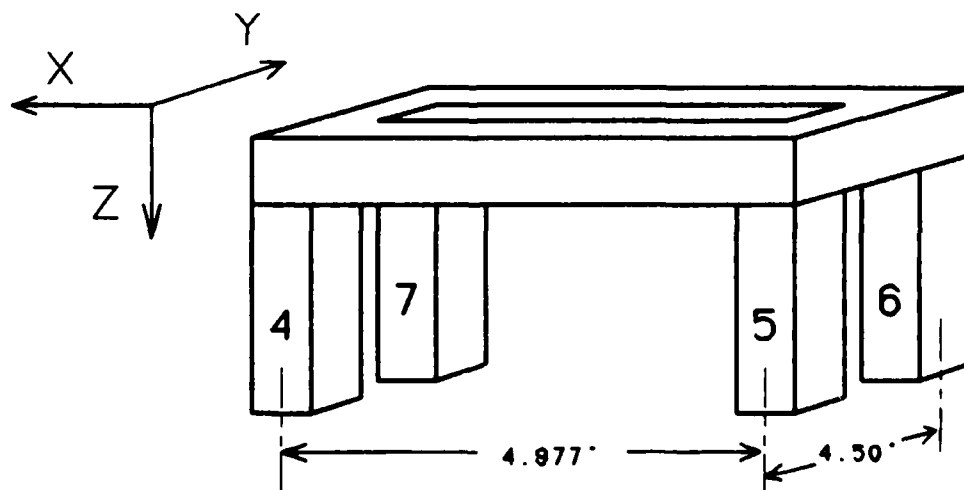
Figure 3.13 Coordinates of LCU Base Plane

27

The sensitivity of each load cell is ± 0.003 inches over the load cell range of the ± 25 lb$_f$. Assembly of the first design of the LCU showed a significant pre-loading on the base load cells when attached to the base plate. This was due to warping of the 1/4 inch aluminum base plate. A redesign made the base plate from 3/8 inch steel, Blanchard ground flat and parallel to ± 0.001 inches. The steel plate proved to limit the pre-loading effect encountered with the aluminum plate.

In addition to the four base load cells, pre-loading was also encountered in the X-Y plane of the LCU. To determine these pre-loads, a zero load voltage output from each load cell was recorded prior to assembly of the LCU. Using these zero load voltages, the pre-loads from the LCU assembly were determined and then used to establish operating limits of the load cells.

Calibration of the LCU was conducted twice due to a calibration shift which occurred during initial testing. Figure 3.14 shows the original calibration assembly used with the model mounted to the steel optical bench. Results of this calibration proved the capability of the LCU to resolve applied forces and moments. However, during initial runs in the tunnel, a significant shift in zero points and load responses was noticed. Examination of the LCU revealed load cell #3 in the X-Y plane had pivoted approximately 5 degrees about its axis and a mounting screw for load cell #1 was loose. As a result, LCU modifications were required.
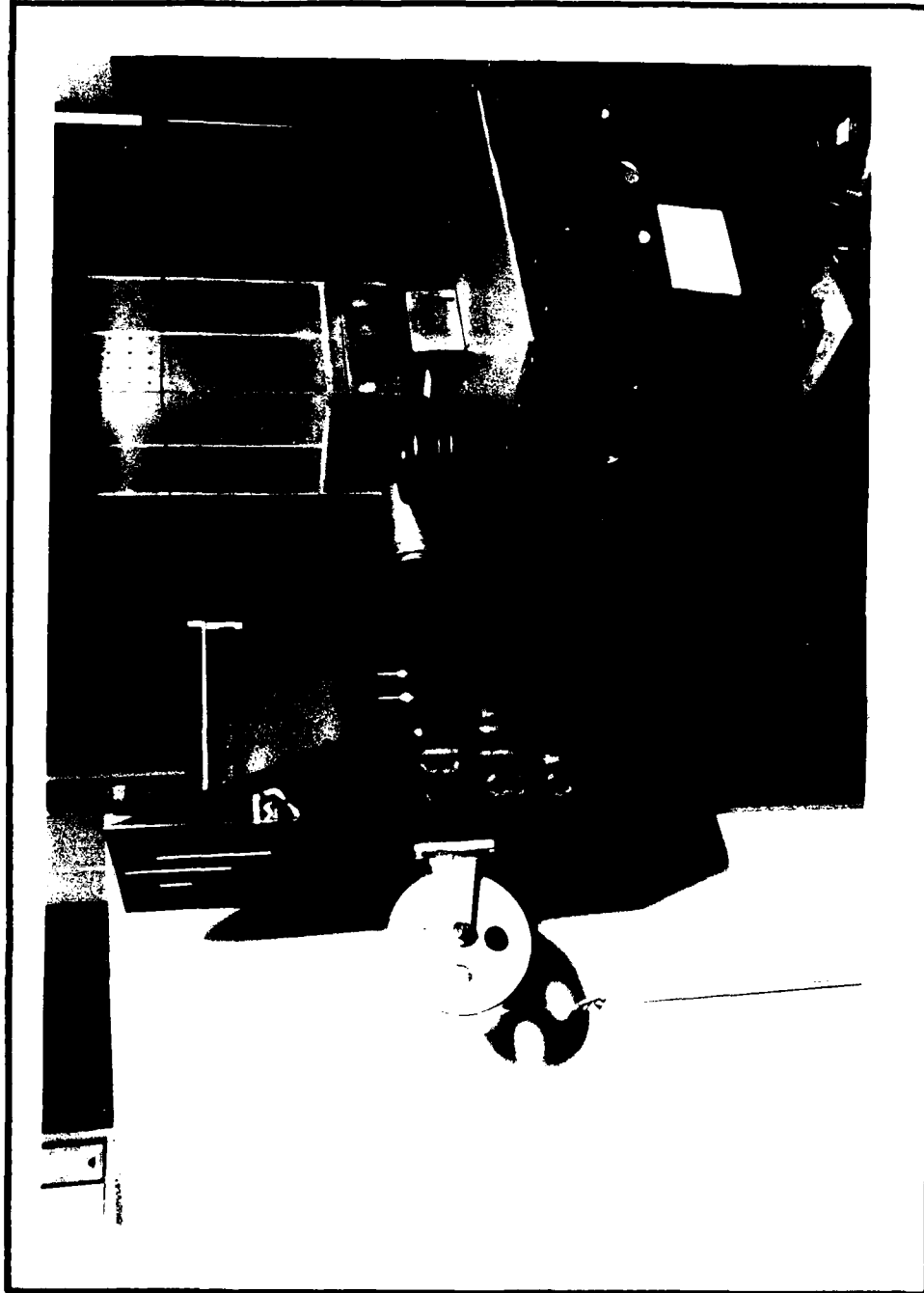
Figure 3.14 Calibration Assembly on Steel Optical Bench

Modifications to the LCU included the addition of 7/64 inch socket head screws into the bases of the four X-Y plane load cells and the conversion of flat head screws to socket head screws. A 7/64 inch socket head screw was installed parallel to the mounting screw of each load cell to prevent pivoting about the load axis. The conversion to socket head screws helped to eliminate some misalignment problems while allowing for better tightening of the mount screws. In addition, "locktight" was applied during assembly to help ensure no repeats of the initial failure.

After the LCU modifications were completed, new load cell limits were established (Table 3.1) and the second calibration was conducted. Figure 3.15 shows the assembly used to calibrate the LCU in the tunnel. Results of this calibration proved to hold through the remainder of the test program. Details of the calibration set up and procedures are found in Appendix A.

Instrumentation

The parameters measured during this investigation included more than just the force and moment data measured through the LCU. Local dynamic pressure was monitored on a bank of water manometers (Figure 3.16) connected to the three upstream ground board pitot-static probes. Barometric pressure was measured daily at the beginning and end of each run using the mercury barometer located in the tunnel building. Tunnel flow temperature was measured using the tunnel inlet thermocouple.

Table 3.1   LCU Operating Limits

Channel	Preload Outputs Volts	Zero Outputs Volts	True Preload Volts	Limits			
				30 lb		35 lb	
				Low Volts	High Volts	Low Volts	High Volts
0	-3.5250E-03	7.4000E-05	-3.5990E-03	-3.2401E-02	3.5990E-02	-3.8401E-02	4.5599E-02
1	-6.5040E-03	3.4000E-05	-6.5380E-03	-2.9462E-01	4.2538E-02	-3.5462E-02	4.8538E-02
2	-5.2620E-03	-1.5000E-05	-5.2770E-03	-3.0723E-02	4.1277E-02	-3.6723E-02	4.7277E-02
3	-1.0255E-02	-2.9000E-05	-1.0284E-02	-2.5716E-02	4.6284E-02	-3.1716E-02	5.2284E-02
4	1.2510E-03	3.4320E-03	-4.6830E-03	-3.1317E-02	4.0683E-02	-3.7317E-02	4.6683E-02
5	-1.1440E-03	1.1520E-03	-2.2960E-03	-3.3704E-02	3.0960E-02	-3.9704E-02	4.4296E-02
6	1.6940E-03	4.5160E-03	-6.2400E-03	-2.9790E-02	4.2210E-02	-3.5790E-02	4.8210E-02
7	-7.8700E-04	8.2100E-04	-1.6080E-03	-3.4392E-02	3.7608E-02	-4.0392E-02	4.3608E-02

True Preload	=	Preload - Zero
1.2mV/lbf	--	Approx Calibaration per Load Cell
30 lbf	--	0.036
35 lbf	--	0.042

30 lbf Low Limit = -0.0360-True Preload
30 lbf High Limit = +0.0360-True Preload
35 lbf Low Limit = -0.042-True preload
35 lbf High Limit = +0.042-True Preload
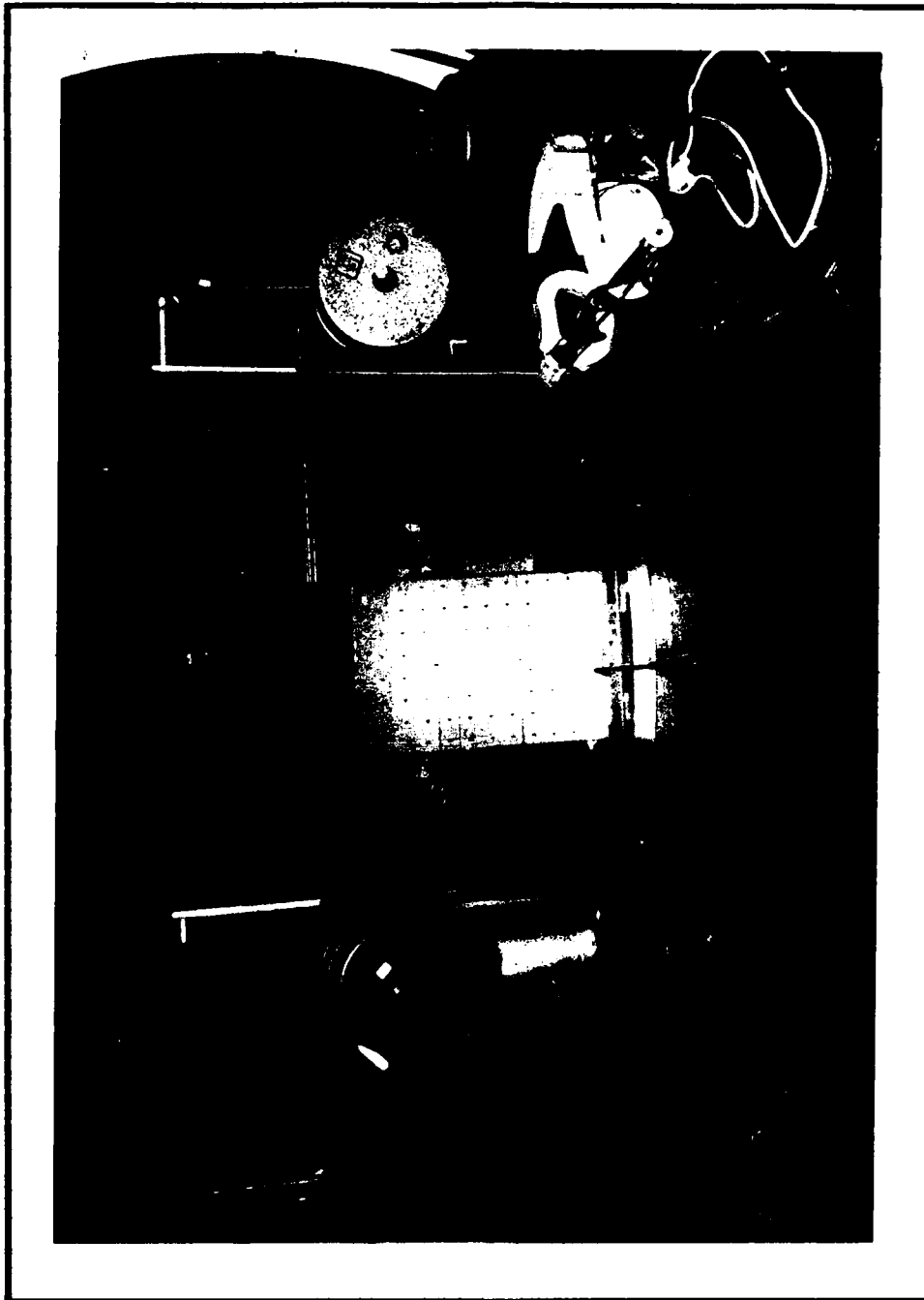
Figure 3.15 Calibration Assembly in AFIT 5-Foot Wind Tunnel
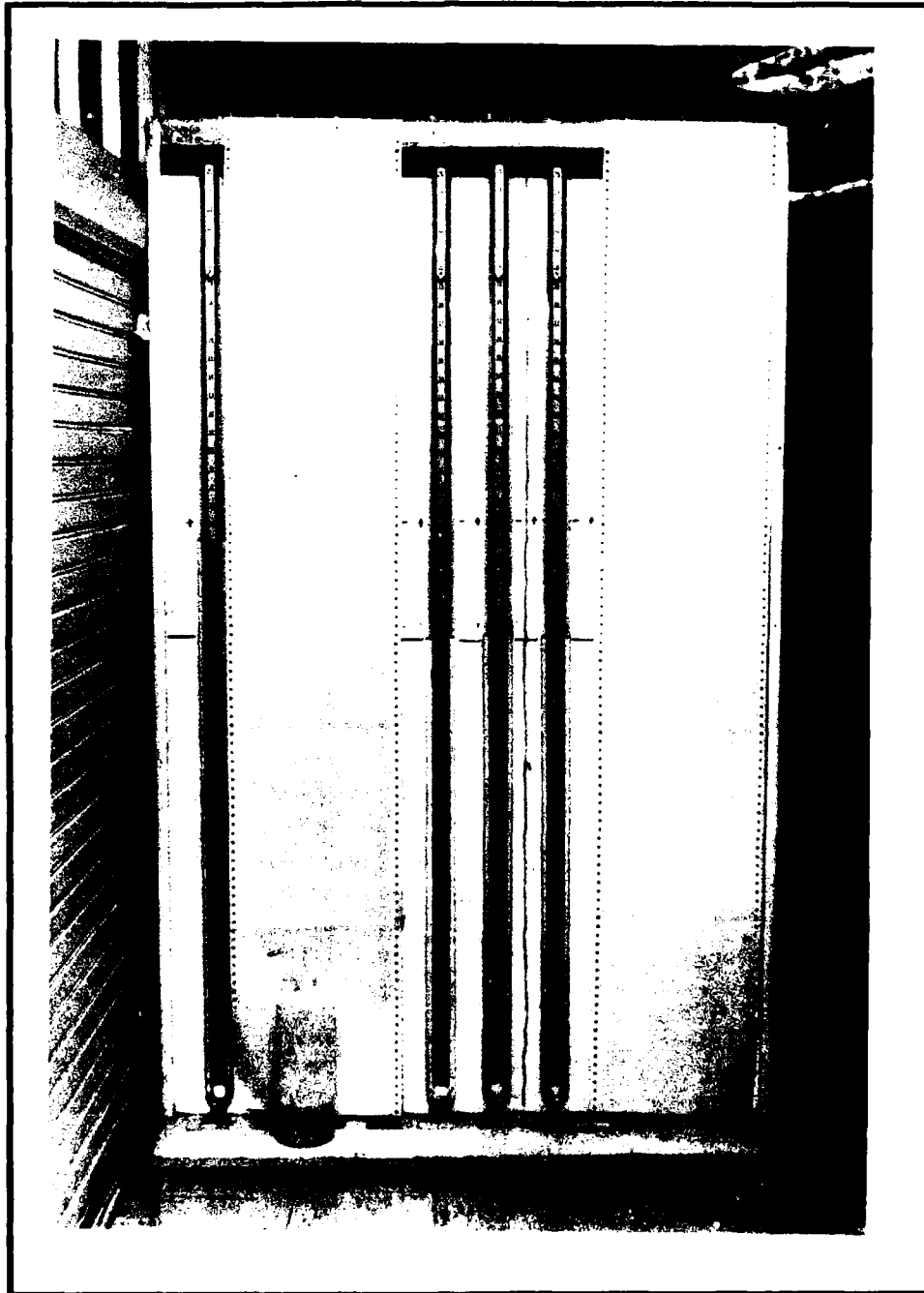
Figure 3.16   Pitot-Static Tube Water Manometer

33

Data Acquisition System

The data acquisition system is shown in Figure 3.17. This data system consists of an Acurex Model 7000-II Modular Data Acquisition System (MDAS) connected to a Zenith Z-248 Personnel Computer. LCU signals were processed through Endevco Models 4423/4225 signal conditioners prior to transmission to the MDAS. Communication between the MDAS and Zenith units was accomplished using the IEEE-488 COMM Port of the MDAS, connected to a National Instruments GPIB interface board installed in the Z-248. The software used to control the MDAS, and to acquire data was written using Microsoft Quick Basic 4.5.

The Endevco signal conditioners provided a clean and steady + 10 VDC excitation voltage to the LCU. Two Endevco power supplies (model 4423) were used, each powering four of the required eight signal conditioners (model 4225). Signals from the LCU were amplified with a hardware gain ot 50 selected on the front of the signal conditioners. BNC cables connected these signal conditioners to the "F2" input cards of the MDAS.

The "F2" input card is an "Anti-Aliasing" voltage input card with sample and hold for the MDAS. This card consists of two analog voltage input channels "A" and "B" and a low pass filter on each channel. This filter is a 7-pole elliptic filter characterized by an very sharp gain roll off past the cutoff frequency. The elliptic filter reaches an attenuation of 72 dB at approximately 1.8 times the cutoff frequency (14: RM-314).
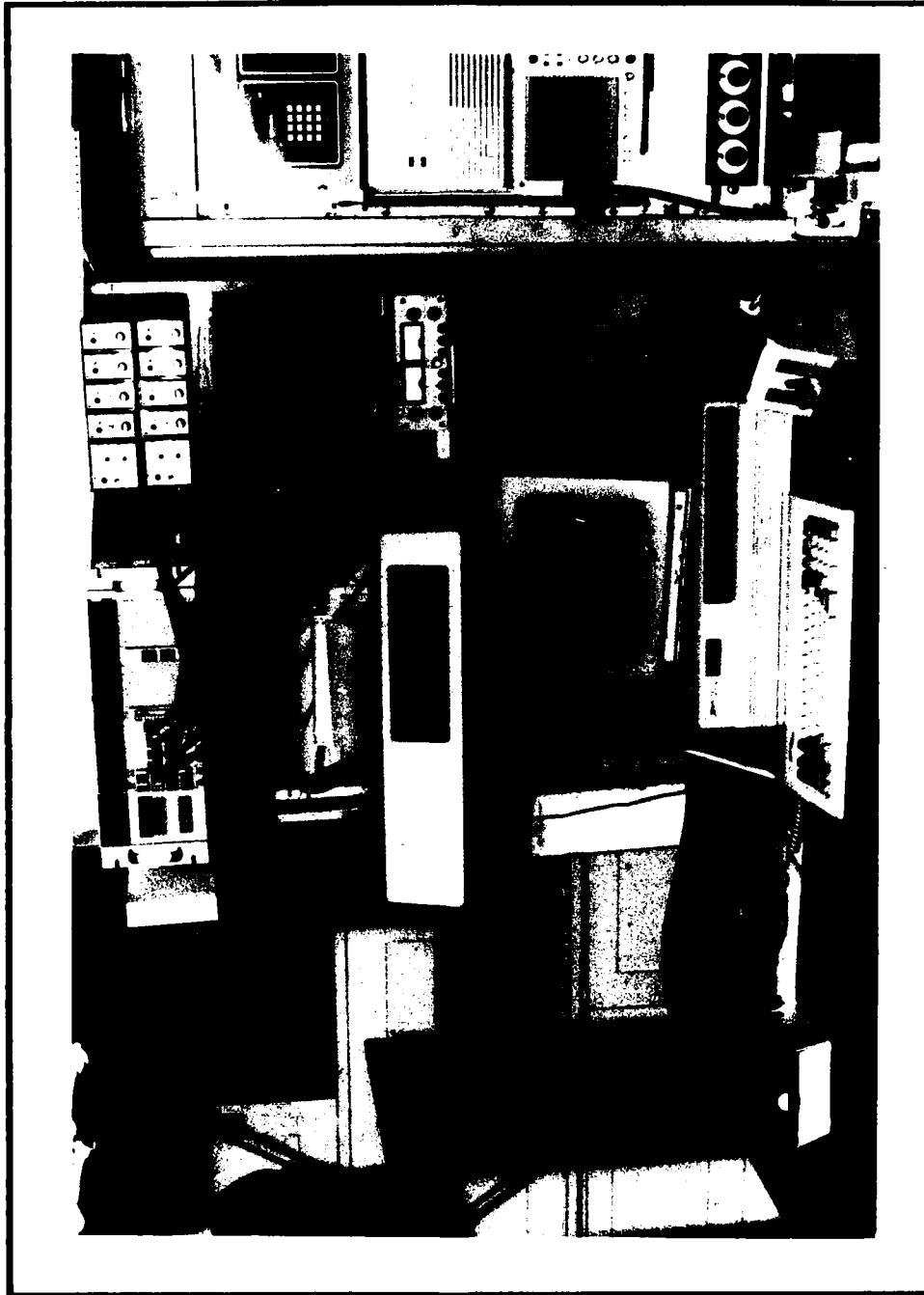
Figure 3.17 Data Acquisition Setup at AFIT 5-Foot Wind Tunnel

For this research, four "F2" cards were installed in the MDAS (slots 3, 4, 5, and 6). The single-ended inputs from the Endevco amplifiers were connected to the "Hi" and "Ground" terminals of the "F2" card, while a jump wire connected the "Lo" and "Ground" terminals.

Hardware gains on the "F2" instrumentation amplifier were set to unity and the cutoff frequency was set at 200 Hz through the software. This cutoff frequency was selected to eliminate any high frequency noise above the expected shedding frequencies. In addition, this setting helps to eliminate possible aliasing problems from noise levels which may be more than half the sample rate of 1000 Hz.

Following the signal conditioning of the "F2" card, the signals were passed to the MDAS A/D converter. Here, a software gain of four amplified the signals prior to the A/D conversion (Appendix B provides more detail in the selection of the signal gains used in the research). After the A/D conversion, the amplified signals were reduced to their original levels as sensed at the load cells. This reduction was computed by the MDAS using the hardware and software gain values programmed into the command software.

Processed signals were stored in digital form on both the MDAS and Zenith hard drives. Data storage files for each data point were divided between the MDAS and Zenith to increase the speed of data storage during testing. This file division was required due to a data transfer limitation between the MDAS and Zenith systems using the Quick BASIC software driver with the GPIB interface. A data point consisted of a one second time sample (1000 Hz sample rate) of the LCU outputs. Each data

point was saved as a text file (x_1.DAT), an average value raw data file (x_2.DAT), and a transient raw data file (x_3.DAT). Here, the "x" was defined as by 00C (for NORO) or 45C (for 45RO) followed by a three digit data point number. The first two files were written directly to the Zenith hard drive while the transient data file of 8000 points was written to the MDAS hard drive. Writing the transient data file to the MDAS hard drive saved time during the run by postponing this transfer until testing was finished. For post processing, the MDAS raw data files were transferred to the Zenith after the daily runs. The details involved in the post processing are presented in the Chapter IV of this thesis. To summarize the data path, Table 3.2 provides the layout of the signal path including individual hardware I.D. numbers.

Table 3.2 Signal Path Infromation

Channel	Load Cell	Endevco Signal Model #442	Conditioners Model #4425	Gain Setting	Excitation Voltage	MDAS "F2" Card F2" Card	MDAS "F2" Card Slot
0	B48764	BA58	AF84	50	9.960+/-0.005	F201	A3
1	B48833	BA56	AF84	50	9.971+/-0.005	F201	B3
2	B48835	BA57	AF84	50	9.981+/-0.005	F202	A4
3	B48835	BA55	AF84	50	10.038+/-0.005	F202	B4
4	B48766	BA61	AF83	50	8.929+/-0.005	F203	A5
5	B48757	BA60	AF83	50	9.918+/-0.005	F203	B5
6	B48762	BA62	AF83	50	9.973+/-0.005	F204	A6
7	B48832	BA59	AF83	50	9.999+/-0.005	F204	B6

MDAS 7000 ISERIAL #   A64221

38

IV Experimental Procedures

Pre-Test Model Analysis

A structural modal analysis was conducted on the model assembly (model/LCU combination) to determine natural frequencies. This testing involved tapping a side of the model with a tap hammer, measuring the vibratory response of the model assembly. An accelerometer was placed on the same side of the model that was tapped in order to measure the vibratory response. Due to the high dampening nature of the plexiglas structure, responses could not be picked up if the accelerometer was placed on a face other than the one tapped. The spectrum dynamic analyzer used for this testing is shown in Figure 4.1. Original testing was conducted with the model attached to the steel optical table as shown in this figure. Results from the analysis showed two modes present in the frequency range of interest. The first mode was detected at 23.2 Hz with a second mode at 87.4 Hz. The next mode detected was at 450 Hz, well above the frequency of interest.

After the LCU rebuild (discussed in Chapter III), natural frequencies were checked again to see if the rebuild shifted any of the natural frequencies to a higher level. This time, the model assembly was tested after being installed in the tunnel. Results indicated no significant changes in frequency levels of the first two modes. Sample plots of these results are shown in Figures 4.2 and 4.3. Both figures show the first two modes as measured on the negative Y face of the model for two different tap locations. Accelerometer and tap point coordinates are
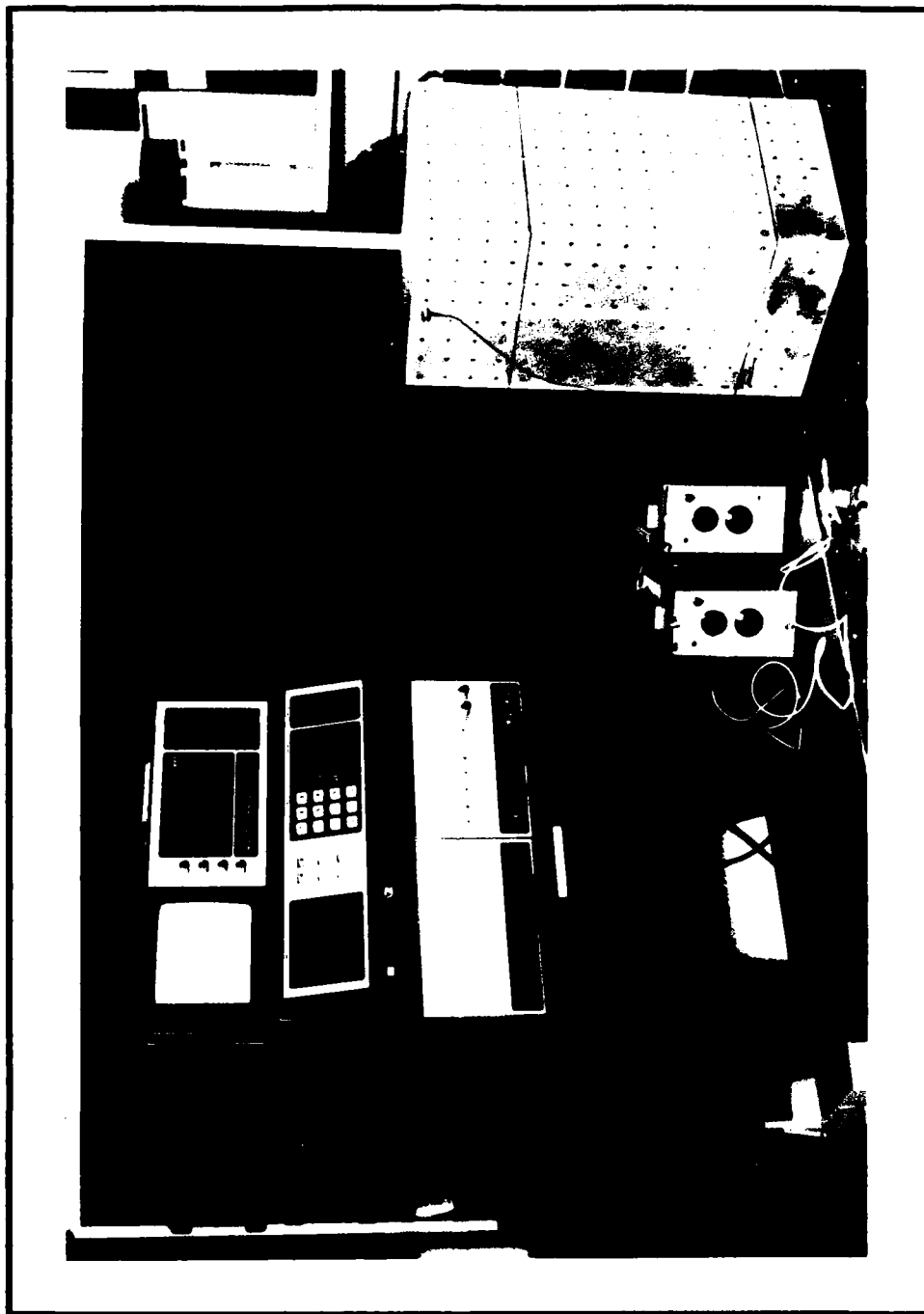
Figure 4.1   Modal Analysis System

40
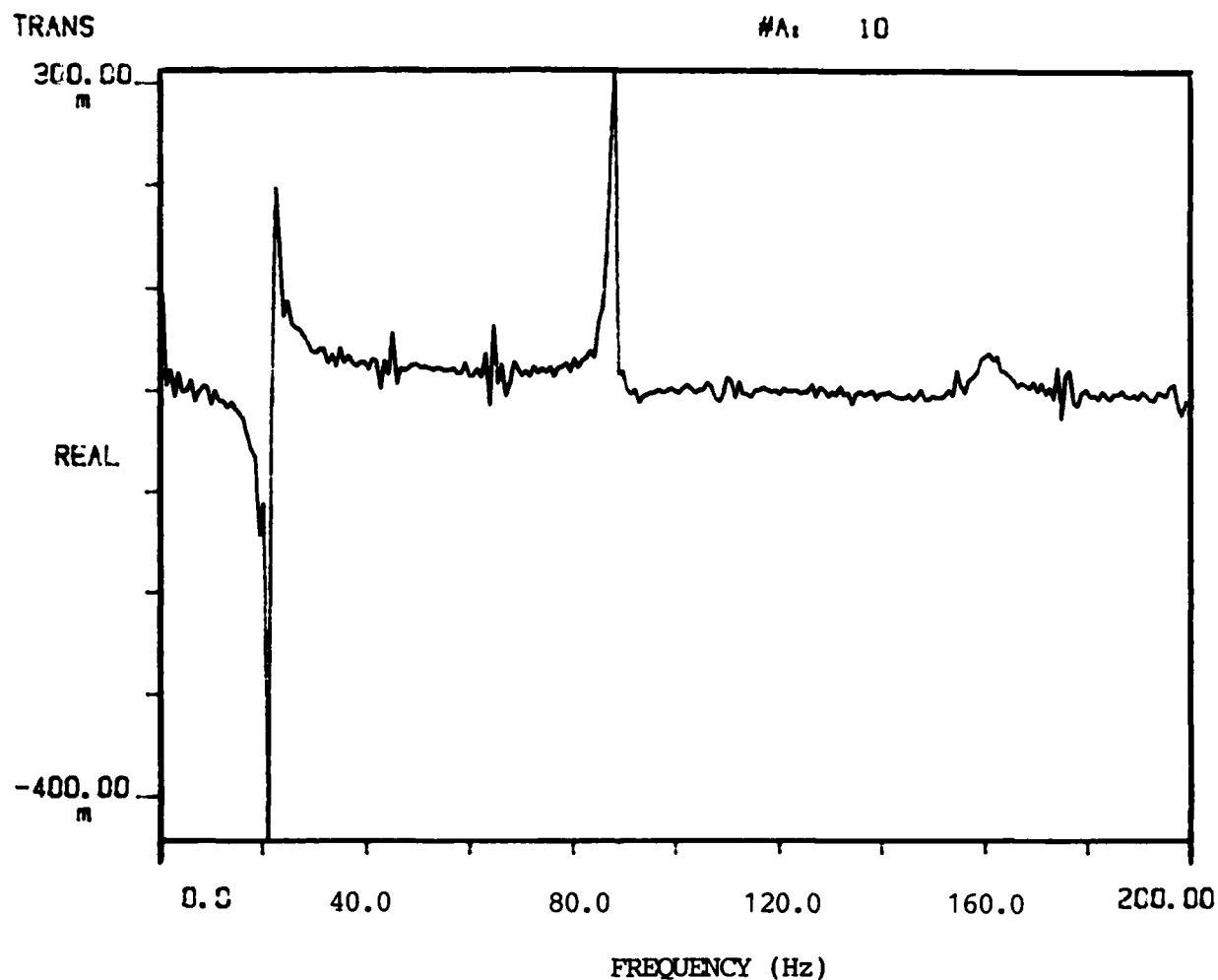
(Tap and Accelerometer Locations Referenced to Top and Side Edges)

Tap Point # 18   Accelerometer

    11.5" Down   1" Down

    3.5" In from Left   1.5" In from Right

    FIRST MODE AT 22.6 HZ

    SECOND MODE AT 88.3 HZ

Figure 4.2   Modal Analysis for Negative Y Face of Model   (PT 18)

1.5000

REAL

-500.00
m

0.0   40.0   80.0   120.0   160.0   200.00

FREQUENCY (Hz)
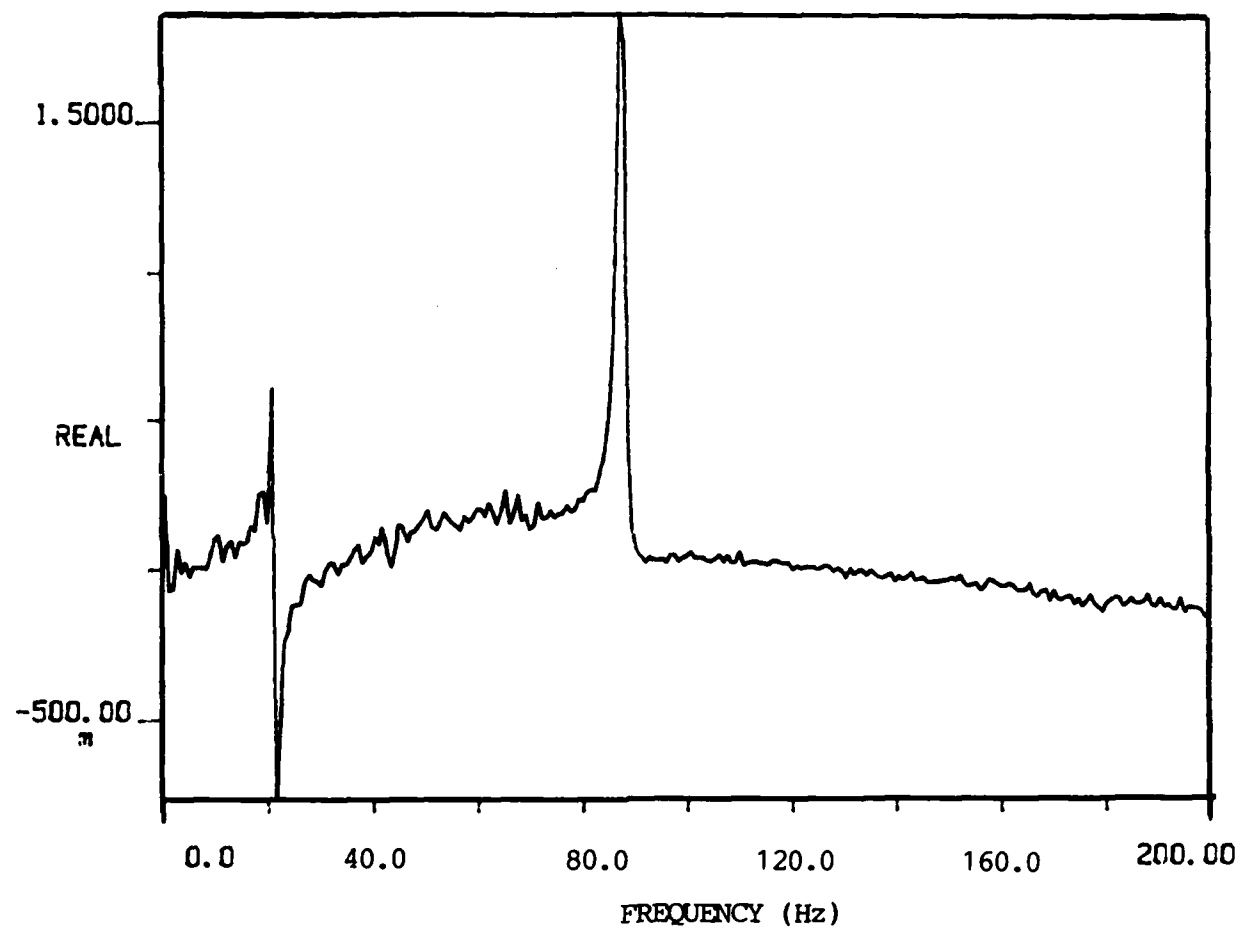
(Tap and Accelerometer Locations Referenced to Top and Side Edges)

Tap Point # 11   Accelerometer

2.5" Down   1" Down

1.5 " In from Left   1.5" In from Right

FIRST MODE AT 21.1 HZ

SECOND MODE AT 88.3 HZ

Figure 4.3   Modal Analysis for Negative Y Face of Model (PT 11)

42

provided with each figure, referenced from the top and side edges of the negative Y-face.

Trailing Edge Flap Adjustment

Initial testing served as a "shake down" of the test setup. Tunnel speeds between 70 ft/s and 130 ft/s were used to adjust the trailing edge flap to align flow stream lines over the ground board. This adjustment was accomplished by observing a series of tufts attached to a vertical string stretched between the top and bottom of the tunnel, just in front of the ground board (see Figure 4.4). Adjustments were made to the flap until the tufts streamed parallel to the ground board, indicating no leading edge spillage due to bottom side blockage. The curved strings seen in the figure are tangled strings which wrapped around the vertical string when the tunnel was first started. An approximate flap angle of 24 degrees seemed to equalize upper and lower blockages, and was the setting used for the remainder of testing.

Local Dynamic Pressure

The tunnel velocities measured by the tunnel upstream static taps described in Chapter III do not represent the true local velocities at the model. Acceleration effects due to the ground board blockage results in a shift to higher values of the local velocities, or dynamic pressures (q) as they are measured. The amount of this shift is proportional to the tunnel speed. As tunnel speed increases, the difference between the q_{tunnel} and q_{local} also increases. To account for this

43
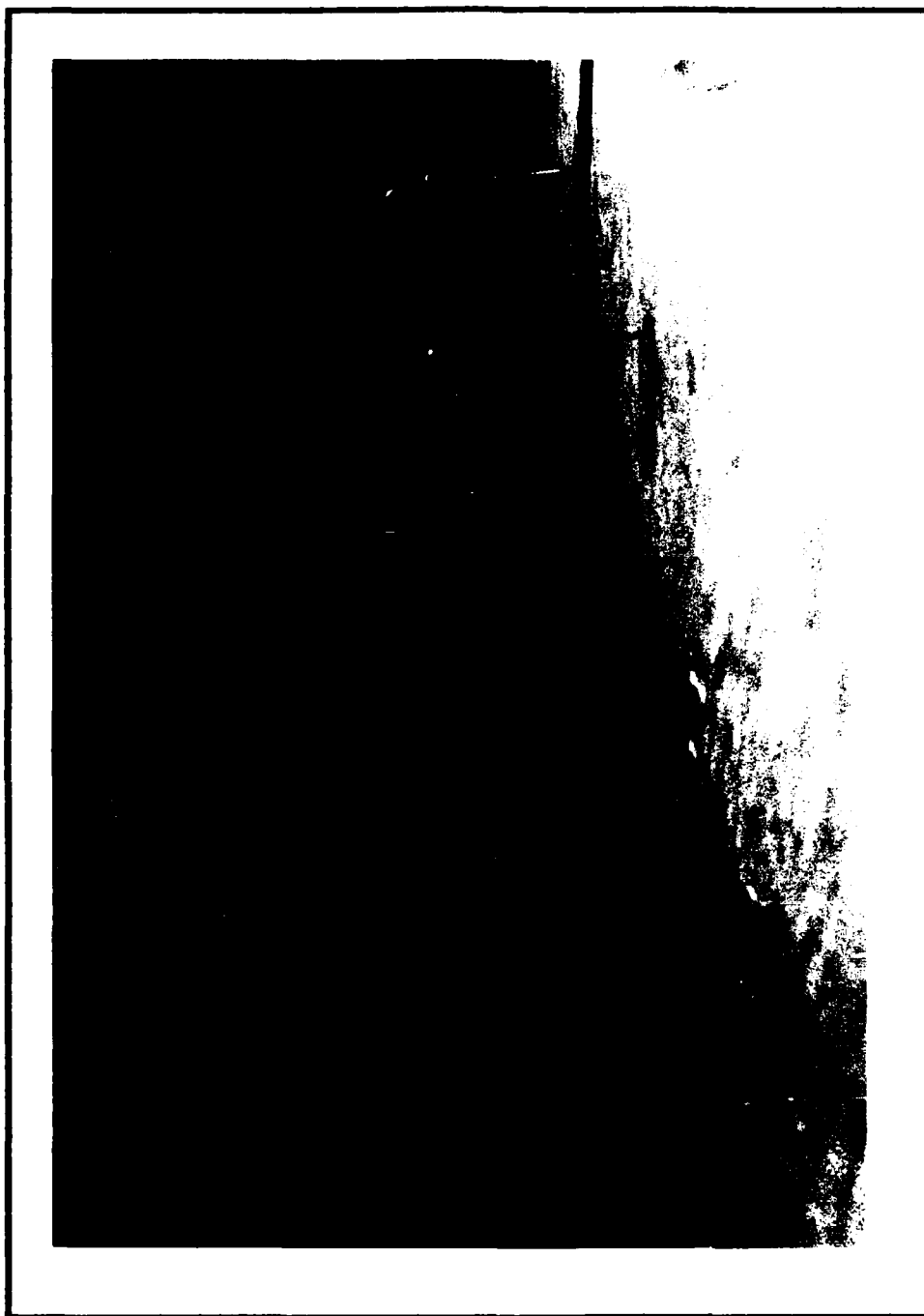
Figure 4.4 Ground Board Leading Edge Stream Line Tufts String

blockage effect, values from the three ground board mounted pitot-static probes were used to determine the q_{local}.

A survey of the local dynamic pressure was conducted using the ground board pitot-static probes. The first check was to determine variations in q_{local} due to probe height variations. Figure 4.5 is a plot of the average q_{local} versus q_{tunnel}, as measured by the ground board pitot-static probes at three different elevations. The shift in q_{local} compared to q_{tunnel}, as described above, is shown by the data points above the 45 degree line (representing $q_{local} = q_{tunnel}$). The q_{local} variation due to probe height appears negligible at the 2 and 4 inch level, with a slight increase over these values appearing at the 8 inch level. This increase in q_{local} at the 8 inch level is due to the reduced blockage effects from the model which is 8 inches high. From these results, an average probe height of 4 inches was selected for measurement of the local dynamic pressure.

The second check was a comparison of q_{local} variation across the ground board, normal to the wind (i.e. along the Y-axis). Figure 4.6 shows the span wise variation of q_{local} at 4 inches above the ground board versus q_{tunnel}. These results indicate non-uniformity in q_{local} across the Y-axis span from right to left, aft looking forward. The center probe displays a lower q_{local} compared to q_{tunnel} due to the blockage effects of the model. As for the two outside probes, the model influence is not as significant since these probes are spaced wider than the model. The variations in these values show an apparent non-symmetry in the tunnel flow field. Since the cross section of the tunnel test
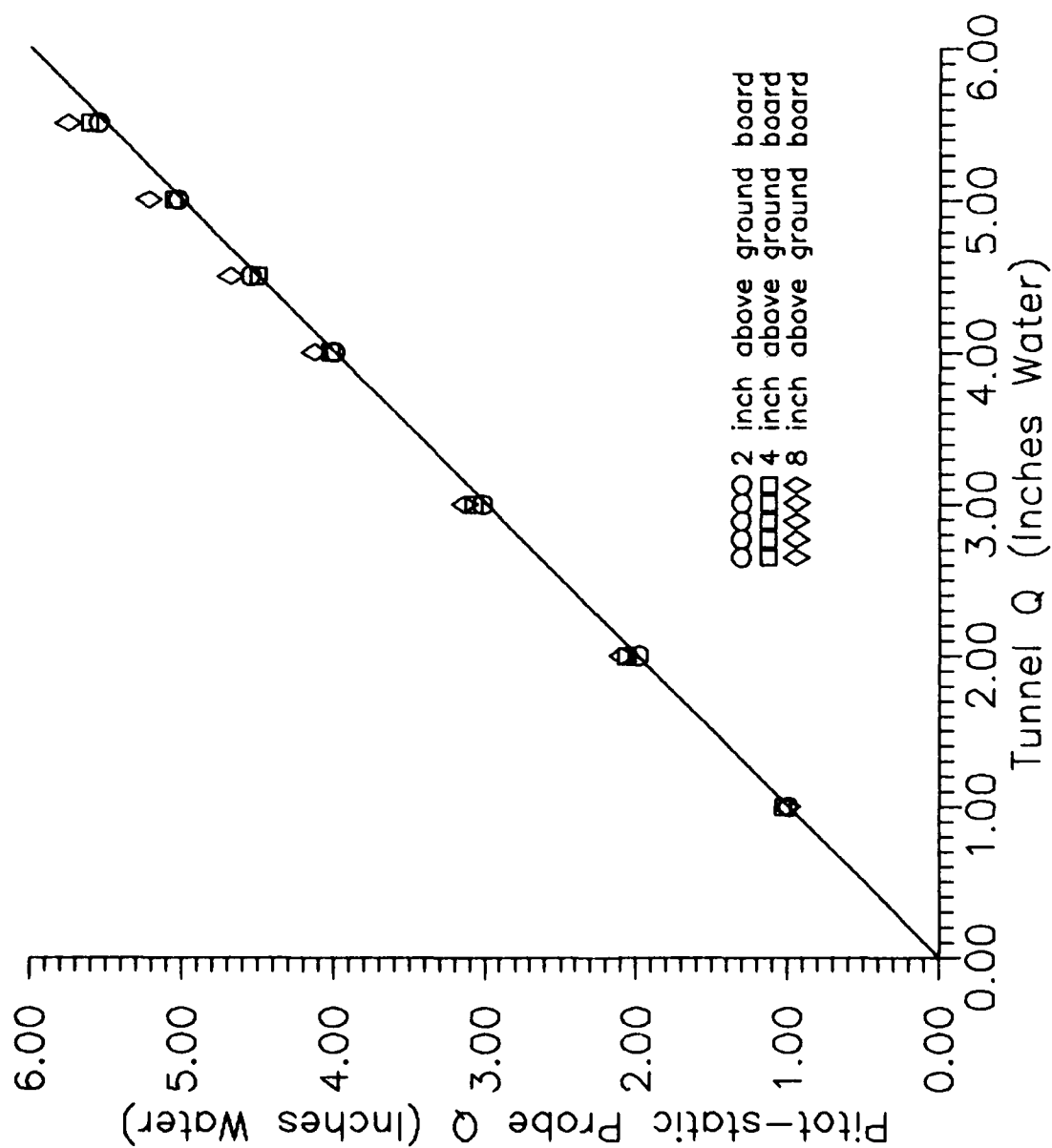
Figure 4.5 Dynamic Pressure Measurement Comparison
(Pitot-static Probe Averages vs.Tunnel)

46
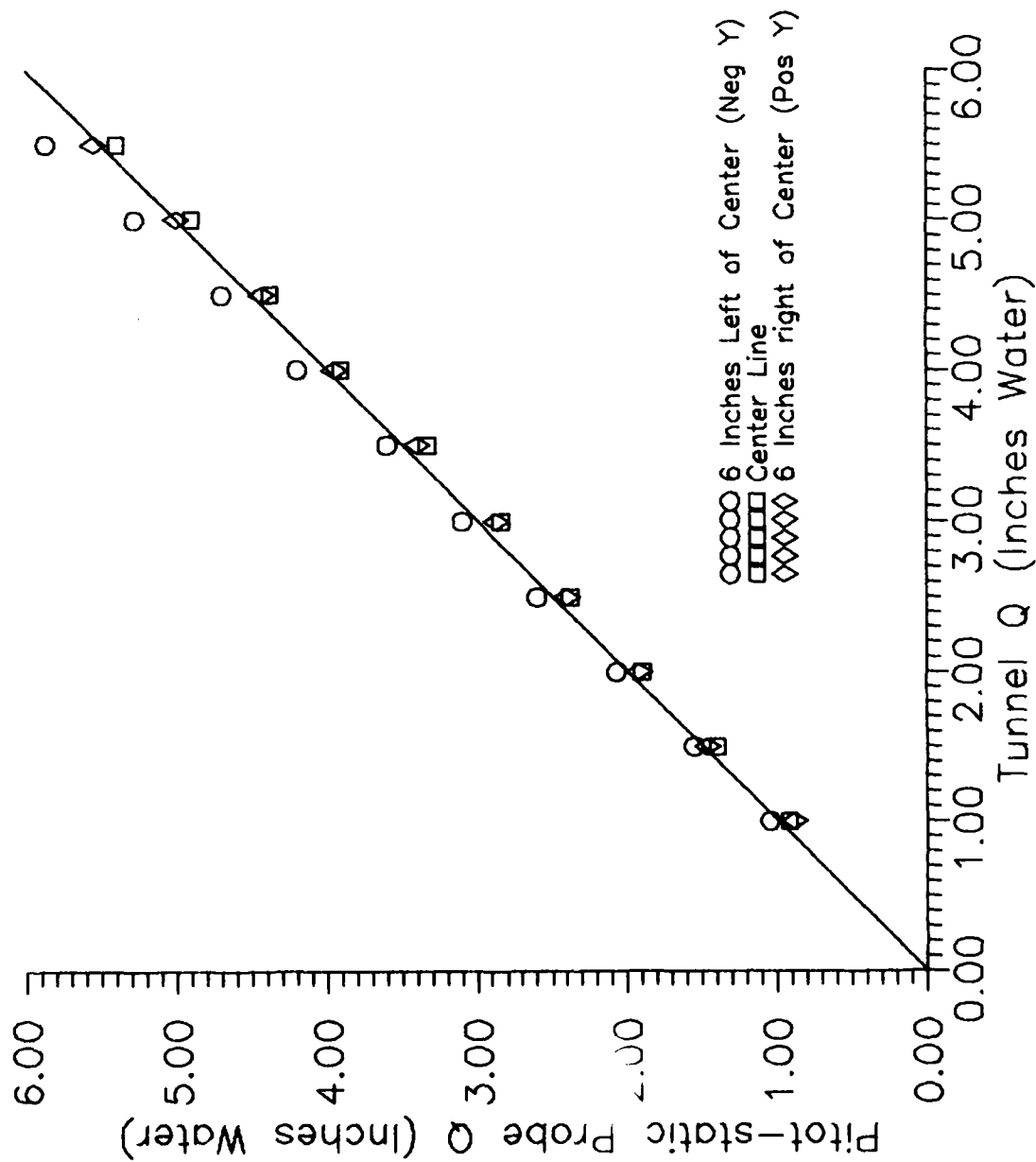
Figure 4.6 Dynamic Pressure Variation Across Test Section
(Pitot-static Probe vs.Tunnel)

47

setup is symmetric, this velocity profile variation is most likely due to the tunnel inlet screens or flow field deficiencies in the return flow external to the tunnel. To compensate for this variation, the average of three pitot-static probe values was used. Thus, the local dynamic pressure for the remainder of testing was based on the average values recorded from the three pitot tubes located 4 inches above the ground board.

Calibrations

The only system requiring calibration during this experiment was the LCU. Procedures and details of the calibrations are provided in Appendix A.

Zero Point Definition

Test results indicated up to a 0.33 lb_f deviation in the LCU zero points before and after data runs. Since the zero point is used to process the force and moment data, a standard for zero point acquisition was established. The zero point acquisition procedure was to:

1) Run the tunnel up to a speed represented by 1.5 inches of water measured on the tunnel micromanometer

2) Hold tunnel speed for 30 seconds

3) Reduce tunnel speed to zero

4) Record the LCU voltages with the MDAS.

This procedure established the base line zeros for the remainder of the

particular data run and was repeated for each configuration change or new day's run.

Test Configuration and Data Acquisition

Six configurations were tested, starting with three no-rotation (NORO) configurations (wind directly on model face) followed by three configurations at a positive 45 degree rotation (45RO) about the Z-axis. All data was acquired with respect to the LCU coordinates In the case of the 45 degree rotation, data was converted back to the tunnel coordinates frame as shown in Figure 4.7. For final analysis, this data was transformed into wind axis coordinates by a 180 degree rotation (about the Y-axis) as shown in Figure 4.8. The data run summaries found in Appendix C are for the wind axis coordinates.

For each configuration, data points were taken at discrete steady-state speeds between 50 ft/s and 180 ft/s. Testing started with the NORO closed configuration and was followed by the 4 inch and 8 inch cavity configurations. For the initial NORO runs, an accelerometer was attached to the top, back face of the model to monitor any possible acceleration limits. This accelerometer provided real time vibration data of the model in the Y-axis (perpendicular to the wind direction) and was displayed on an oscilloscope setup next to the data system. After preliminary testing showed no signs of hazardous vibration, the accelerometer was removed. Upon completion of the NORO runs, testing was repeated for the 45RO configurations in the same manner.
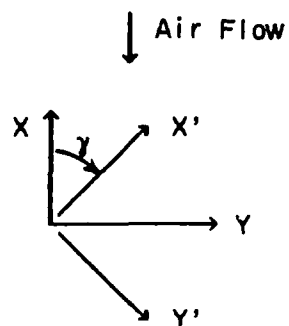
Air Flow

X, Y, Z Tunnel Coordinates

X', Y', Z' LCU Coordinates

γ = Angular Rotation about Z'-axis of the LCU Coordinates Relative to Tunnel Coordinates

$$\begin{bmatrix} X \\ Y \\ Z \end{bmatrix} = \begin{bmatrix} \cos \gamma & -\sin \gamma & 0 \\ \sin \gamma & \cos \gamma & 0 \\ 0 & 0 & 1 \end{bmatrix} \begin{bmatrix} X' \\ Y' \\ Z' \end{bmatrix}$$

Moments are transferred in the same manner.

Figure 4.7   Coordinate Transformation for the LCU to Tunnel
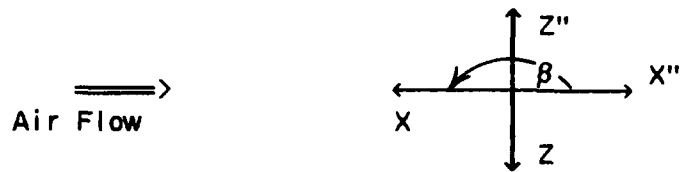
X, Y, Z Tunnel Coordinates

X", Y", Z" Wind Coordinates

β = Angular Rotation about Y-axis of the Tunnel Coordinates Relative to the Wind Coordinates

$$\begin{bmatrix} X" \\ Y" \\ Z" \end{bmatrix} = \begin{bmatrix} \cos\beta & 0 & \sin\beta \\ 0 & 1 & 0 \\ -\sin\beta & 0 & \cos\beta \end{bmatrix} \begin{bmatrix} X \\ Y \\ Z \end{bmatrix}$$

Moments are transferred in the same manner.

Figure 4.8 Coordinate Transformation for Tunnel to Wind Coordinates

Data points were taken at steady-state speeds defined by 1/2 inch intervals as measured on the tunnel micromanometer. With the computer set up to monitor load cell outputs continuously, tunnel speed was increased at these 1/2 inch intervals until load limits were sensed. This upper speed limit was defined when the limit checking codes indicated the occurrence of a 35 lb_f loading for any of the load cells. When the load cell limits were reached during testing, they appeared as periodic loadings as opposed to steady loadings.

Data was recorded both manually and automatically for each data point. The manual recordings were done by hand on a data sheet which contained the daily barometric data, room temperature, tunnel speed setting, inlet air temperature, and data point number. After recording these values on the data sheet, the data acquisition loop was activated and of the force and moment data was automatically recorded by the MDAS system.

Data Reduction

Data reduction was achieved using routines developed in Quick Basic (Version 4.5) along with Goldstar's GRAPHER plotting program (Version 1.75) and DSP Development Corporation's DADiSP Worksheet data analysis program (Version 1.05B). Post-processing was conducted in three phases on a Zenith 248 PC.

The first phase involved a post-processing routine written in Quick BASIC to convert the raw LCU signals into force and moment data, based on the LCU calibration coefficients. Both mean data and transient val-

ues were processed through this code. Phase two involved processing the transient values through the DADiSP Worksheet. From this program, standard deviation data and frequency spectrum data was obtained. In the analysis of the frequency spectrum data, the mean value of the transient signal was subtracted from the transient signal before processing through the DADiSP SPECTRUM command. With this SPECTRUM command, the magnitude of the first half of the Fast Fourier Transform (FFT) of the signal is normalized by the length of the signal. The result is a plot showing frequency spikes of the primary components of the signal. The last phase of post processing involved calculation of the force and moment coefficients along with local velocities based on the q_{local} values. The equations used in this processing are defined in Chapter II and were programmed on the Zenith using Quick BASIC routines.

Flow Visualization

Flow visualization pictures of the flow over the ground board and along the cavity floor were taken as a last part of this thesis study. These flows were observed using oil droplets placed on both the ground board and cavity floor surfaces. The flow visualization oil used was a mixture of:

7cc of 10CS Dow Corning 200 Fluid
3cc of 100CS Dow Corning 200 Fluid
3.5cc Titanium Dioxide
2 drops of OLEIC Acid

The first step in the flow visualization procedure was to apply this white oil mixture as small "dots" to the ground board and cavity floor surfaces using a cotton tip swab. After the oil droplets were

53

applied, the tunnel was brought up to the selected speed and held steady for 30 seconds. Following this 30 second period, the tunnel flow was shut down and pictures were taken of the oil patterns. These pictures were taken through an open hatch on top of the tunnel using a 35mm SLR Camera with a 35-70 macro lens. Once the pictures were taken, the oil streaks were wiped up, the configuration was changed, and new oil droplets were applied, repeating the above procedures.

A comparison between speed settings of 1.5 inches and 4.5 inches of water on the tunnel micromanometer was done to determine which speed would produce the better visualizations. These tunnel settings corresponded to velocities of 87 ft/s and 147 ft/s respectively. Figures 4.9 and 4.10 are top view pictures of the 8 inch cavity, 45RO configuration at these two speeds. Air flow is from top to bottom in these pictures. Comparing the oil streak lengths, it is apparent the higher velocity provides a better picture of the surface flows. Thus, the higher speed setting was selected for flow visualization pictures of the remaining five configurations. All of these pictures were taken through the open top hatch on the tunnel, with the flow direction moving from the top to bottom in each picture.

Figure 4.11 is a picture of the flow pattern along the ground board and cavity floor surfaces of the 8 inch open, NORO configuration. At the top of the picture, flow lines along the ground board surface leading up to the cavity appear straight and parallel to the flow. A minor spreading of these lines from the center line (left and right) is apparent as flow approaches the model. This indicates the extent of upstream
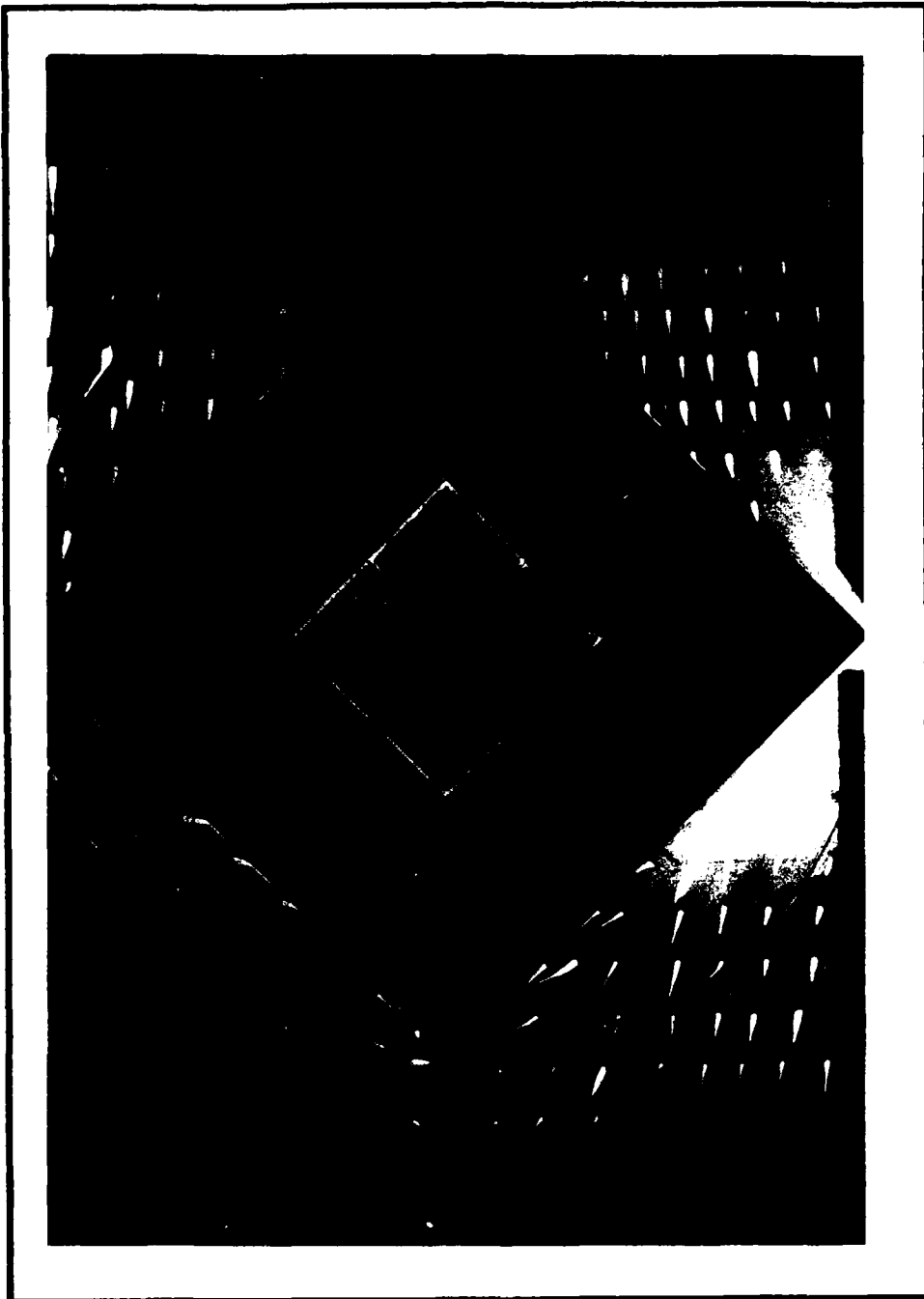
Figure 4.9 Flow Visualization, 8" Cavity, 45°, 85 ft/s
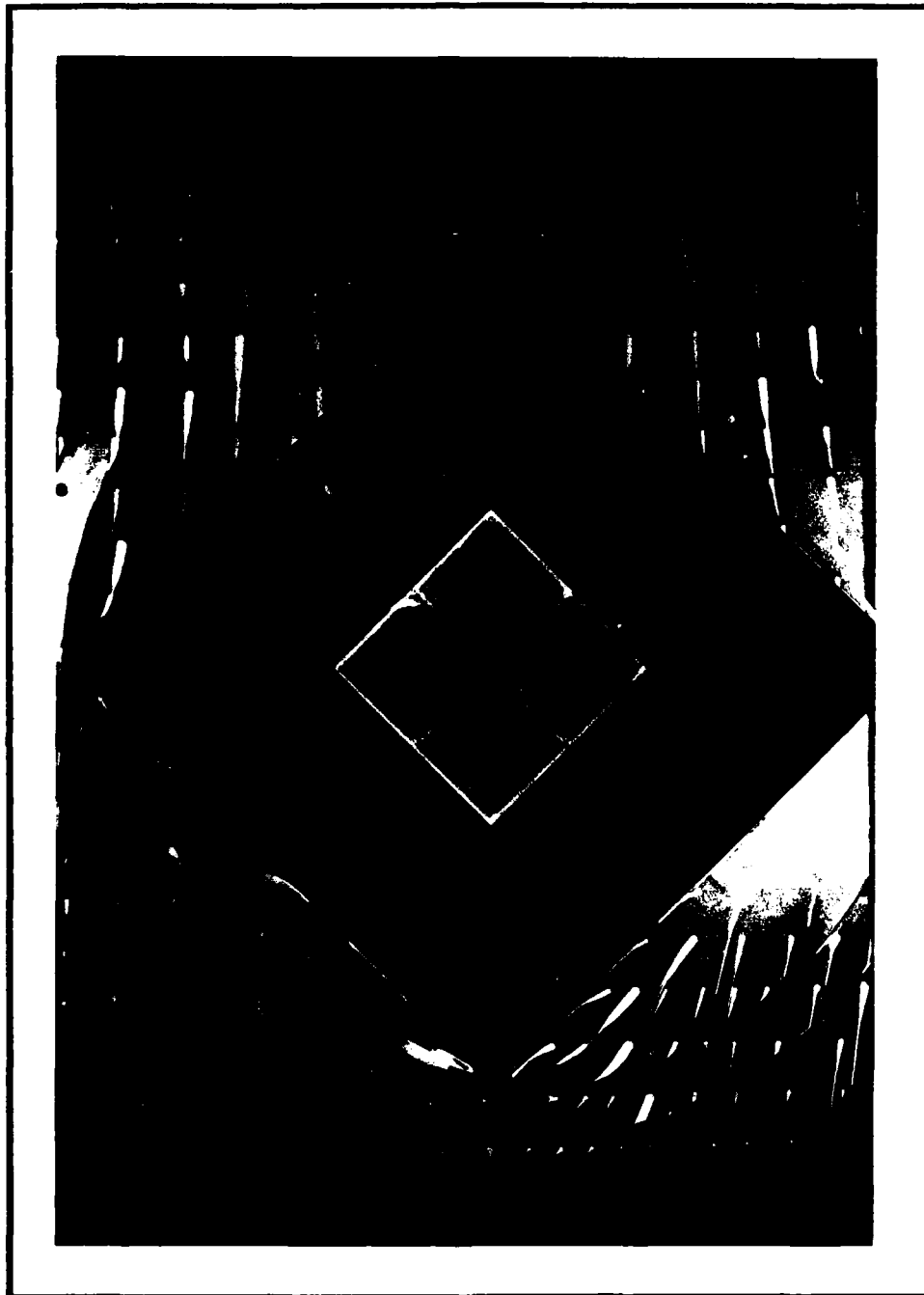
Figure 4.10 Flow Visualization, 8" Cavity, 45°, 147 ft/s

56
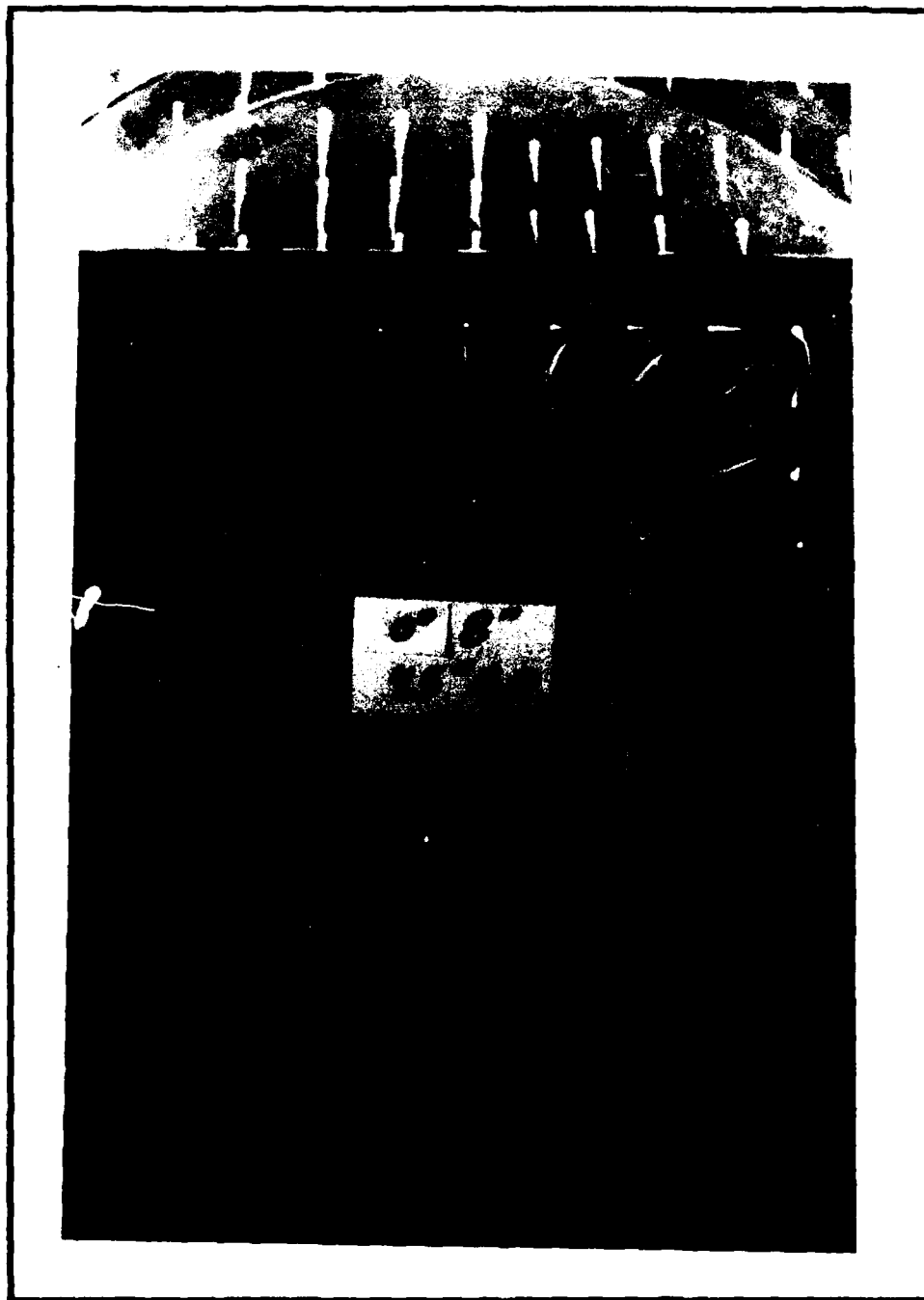
Figure 4.11   Flow Visualization, 8" Cavity, 0°, 147 ft/s

influence the model blockage has on flow stream line adjustment. The oil streaks on the ground board surface aft of the cavity, show swirl and reverse flow patterns behind the model, in the wake. The swirls appear to be a result of vortex shedding off the model and show symmetry about the flow center line. Inside the cavity, oil streaks on the floor indicate flow movement away from the base in front of and on the sides of the model. Oil streaks behind the model show a swirling of the flow towards the back face of the model.

The flows in this cavity can be understood a little easier by looking at the flow patterns around a rectangular building as presented in Figure 4.12 (15:14.2). In this figure, a roll up region is seen in front of the the building near the base. This upwind vortex continues to wrap itself around the base of the model, much like a horseshoe vortex shedding from a finite wind. This creates a strong surface wind area along side of the building. In a similar manner, the flow patterns in Figure 4.11 are most likely formed at the base of the model along the cavity floor. The flow pattern behind the model is probably a combination of three different flow patterns. These combined patterns include the vertical vortices shedding from the aft corners of the model, the base horseshoe vortices, and the up draft flows trying to exit the back portion of the cavity.

When the model and cavity are rotated 45 degrees to the wind (Figure 4.10), both are more streamline. Disturbance effects on the upstream flow lines along the ground board surface appear less with deviations from the center line occurring closer to the model than in the

58
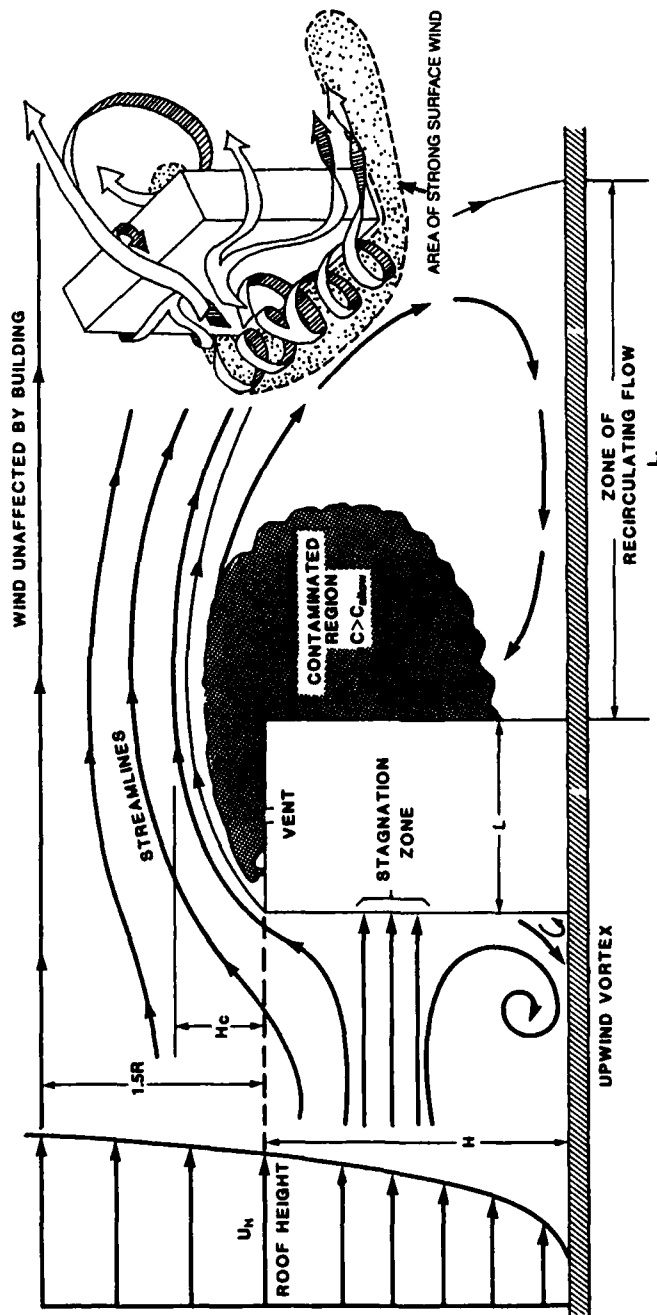
Reference (15:14.2)

Figure 4.12 Flow Patterns Around a Rectangular Building

59

NORO case. Flow aft of the model also seems more uniform, without the heavier swirls and reverse flow patterns observed in Figure 4.11. In regards to the cavity surface patterns, the 45RO case appears to show more pronounced streamlining of the cavity mixing region aft of the model outside edges. It appears the upwind and side vortices are held in a tighter region near the model due to a larger influence by the main flow streamlines passing around the model and through the cavity.

Figure 4.13 is a pictu·e of the 4 inch open NORO configuration. Similar to the 8 inch open NORO case, the upstream effects of the model on the streamline diversions are visible. Down stream of the model, some swirling is apparent, however, there is also an indication of a flow separation bubble forming along the ground board in the wake of the model. This is denoted by the oil droplets which did not streak. As for the flow in the cavity, it appears similar to the results seen in the 8 inch open case.

Figure 4.14 shows the 4 inch open 45RO configuration. Results are similar to those discussed for the 8 inch open 45RO case. The apparent separation bubble seen in the 4 inch open NORO case is not seen here in the narrower wake of the 45RO case.

Figure 4.15 is a picture of the closed cavity NORO configuration. This picture shows prominent reverse flow in addition to the vertical vortex shedding from the aft corner. Comparing this figure to the open cases of the NORO configurations, the cavity appears to disturb the usual ground level flow patterns by lowering the upwind vortex and resulting horseshoe vortex in the cavity. Thus, the reverse flow patterns

60
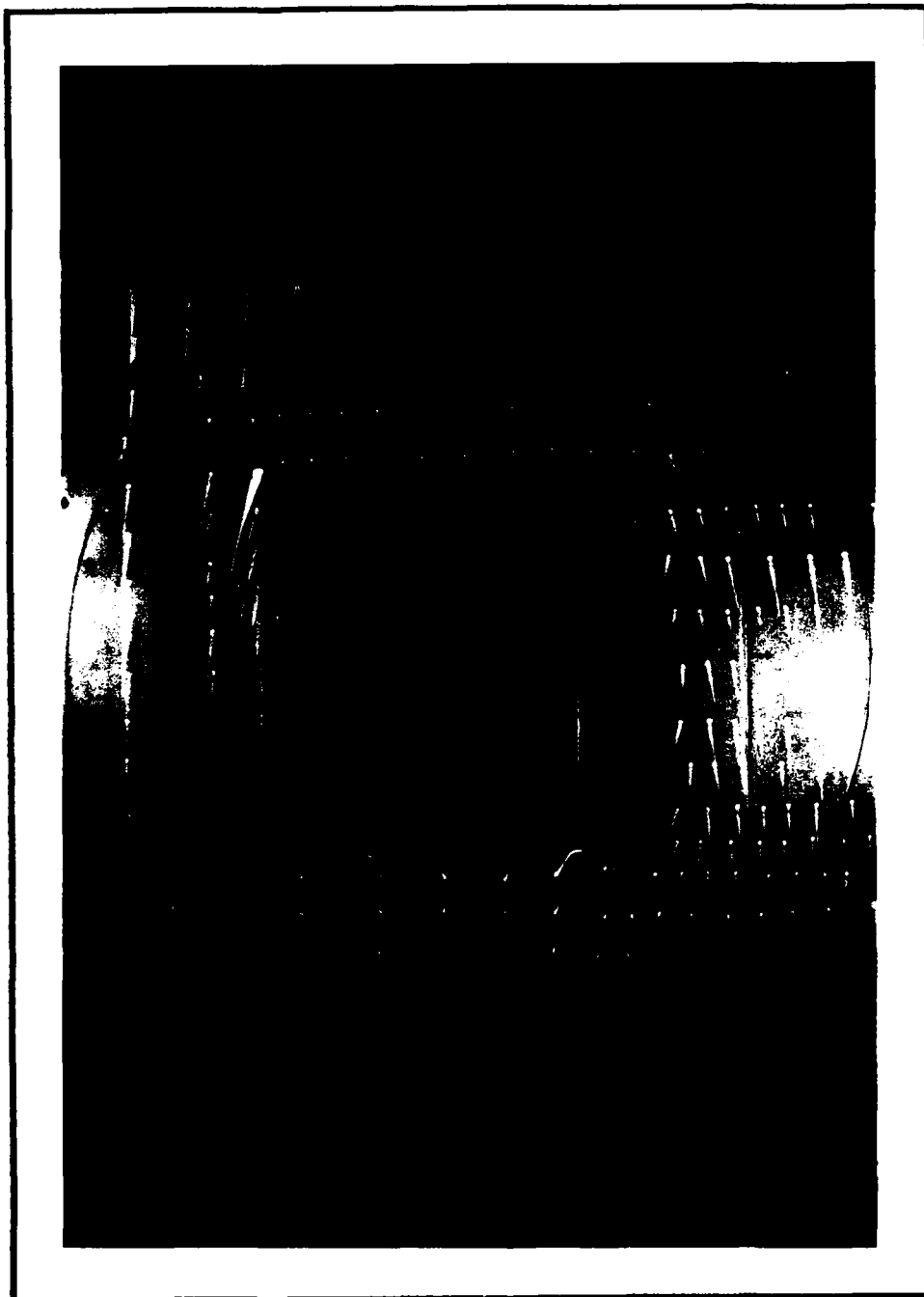
Figure 4.13   Flow Visualization, 4" Cavity, 0°, 147 ft/s
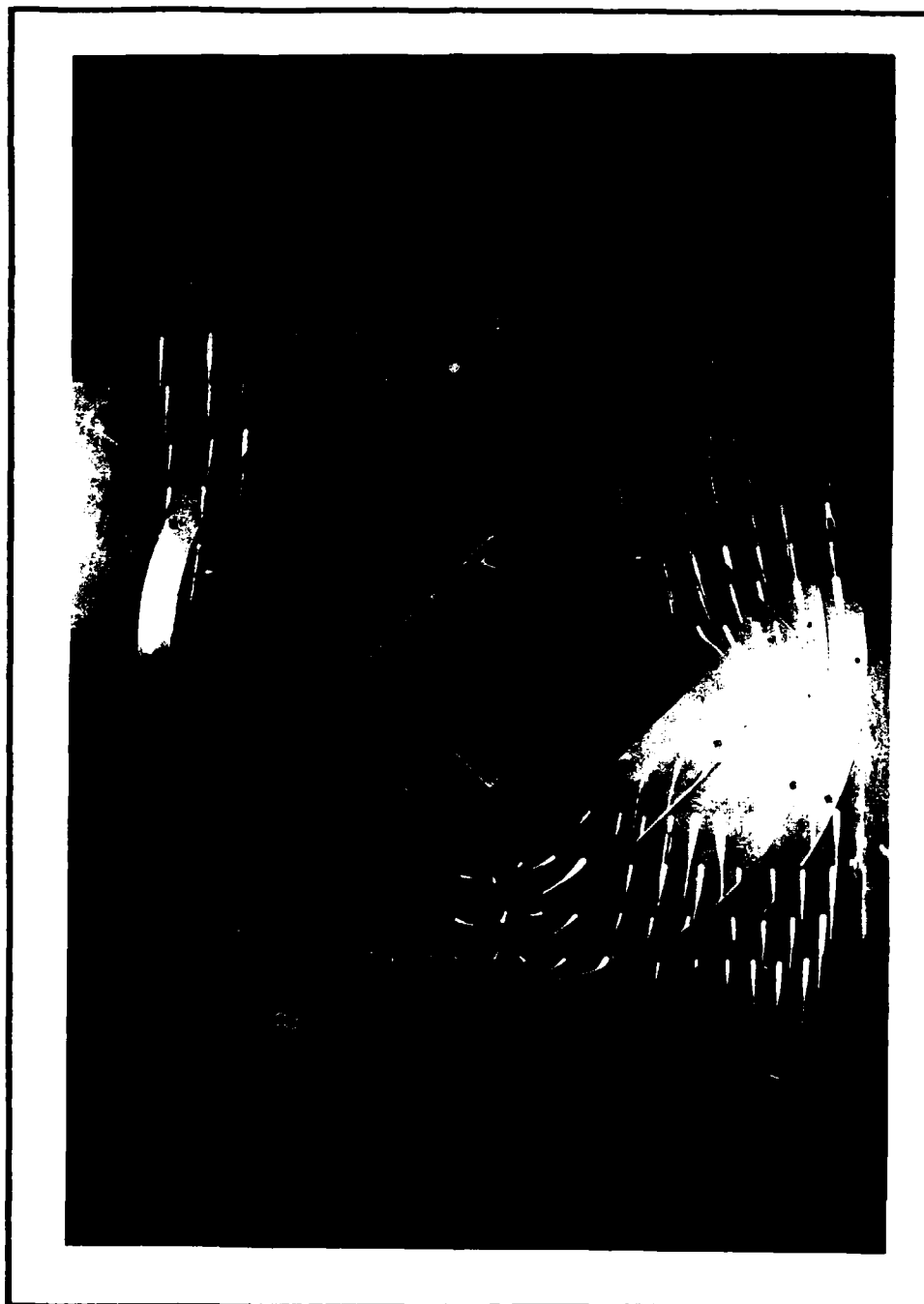
Figure 4.14 Flow Visualization, 4" Cavity, 45°, 147 ft/s
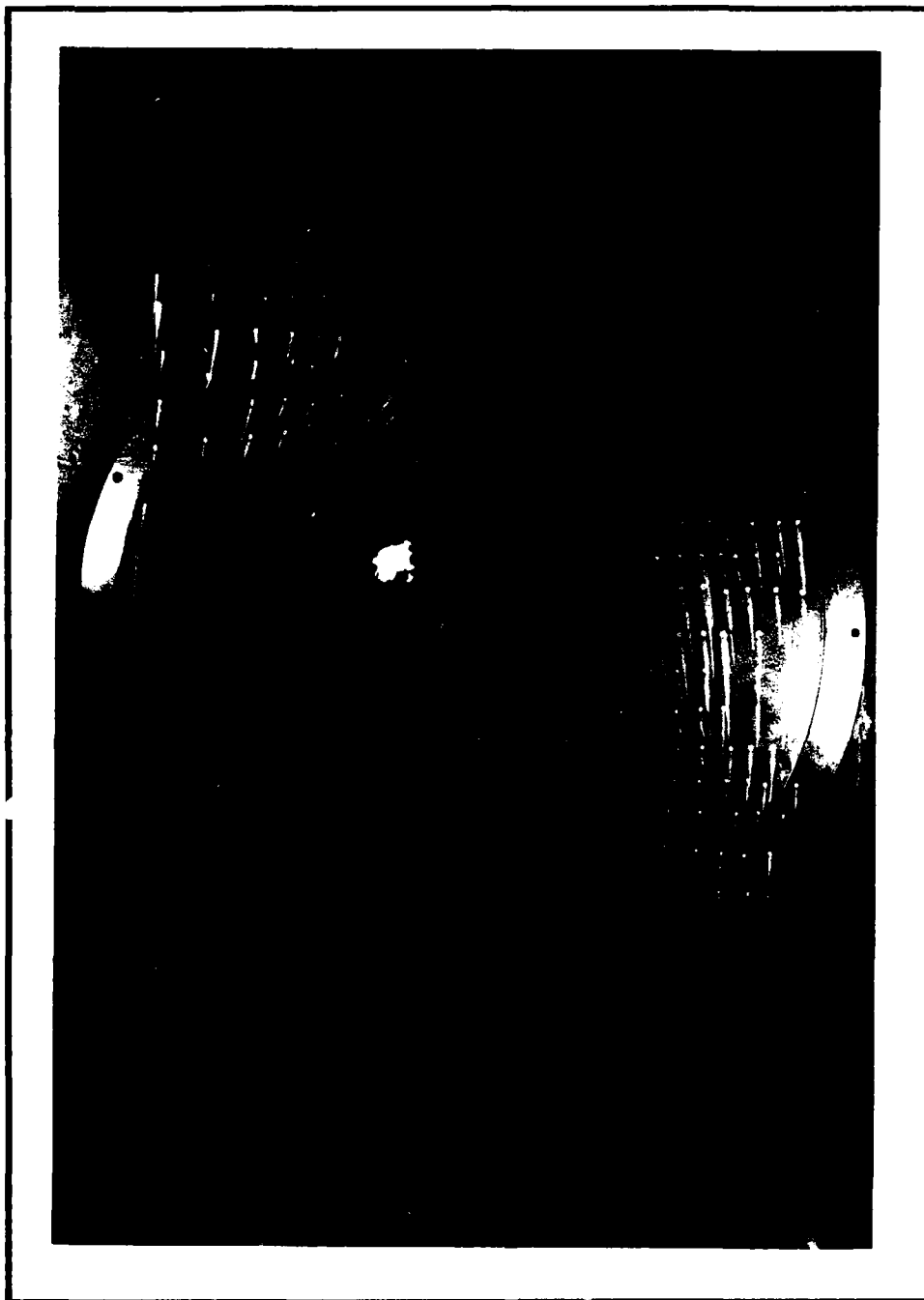
Figure 4.15   Flow Visualization, Closed Cavity, 0°, 147 ft/s

are less prevalent when the cavity is opened. This same effect is noticed in Figure 4.16 which represents the closed cavity 45RO configuration. Compared to the other 45RO configurations, a predominate reverse flow pattern is seen along with the vertical vortex shedding patterns stemming from the two outside corners of the model.

These pictures provide some insight into the vibratory loadings of the model, as discussed in Chapter V.
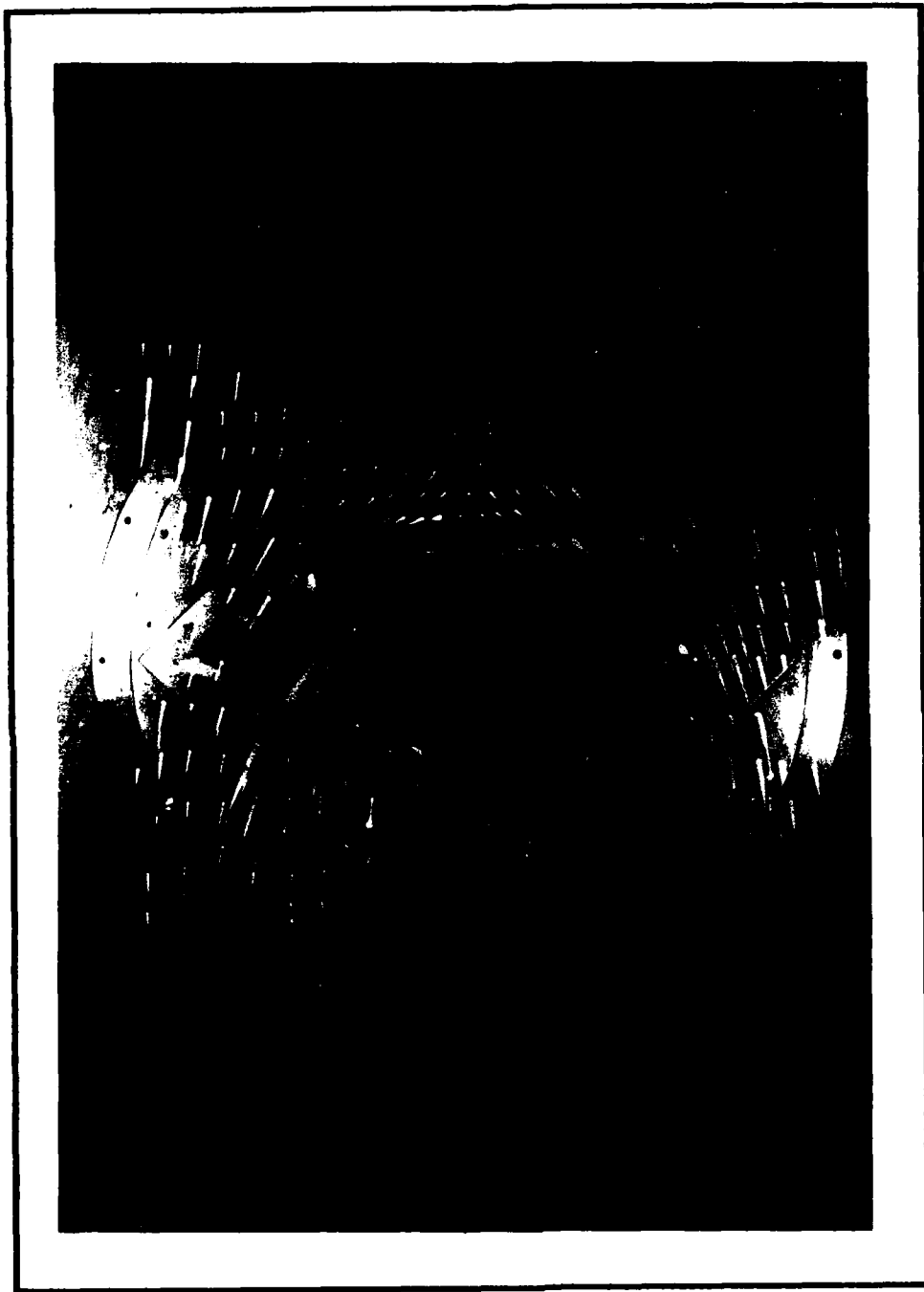
Figure 4.16 Flow Visualization, Closed Cavity, 45°, 147 ft/s

V Results and Discussions

Results are presented as both dimensional and non-dimensional parameters in three areas. In the first area, limitations of the frequency data are discussed, data is compared to results at the USAF Academy, and the effects of cavity size on local dynamic pressure are presented. In the second area, force and moment coefficient data (both mean and standard deviation) are presented in graphic form. These coefficient plots compare cavity opening effects for both the no-rotation (NORO) and 45 degree rotation (45RO) configurations separately. Comparisons are also discussed between rotation configurations. And in the last area, frequency spectrum analysis results for the transient side forces are presented in reference to the model shedding.

As discussed earlier in Chapter IV, the first two natural frequency modes measured on the model assembly were approximately 21 Hz and 87 Hz. Both of these frequencies appeared in the spectrum analysis of the transient data for all configurations tested. The 21 Hz frequency spike was detected in both the X and Y transient force readings along with their counterpart X and Y moment values. The 87 Hz frequency spike was detected in the Z-moment results. These frequency spikes existed at all speeds tested. Figure 5.1 through 5.6 are frequency spectrum plots of the X and Y forces, and the Z-moment as measured on the closed cavity NORO configuration, at 68.5 ft/s and 97.2 ft/s. These figures represent the DADiSP program outputs for the SPECTRUM command applied to these transient signals as described in Chapter IV.
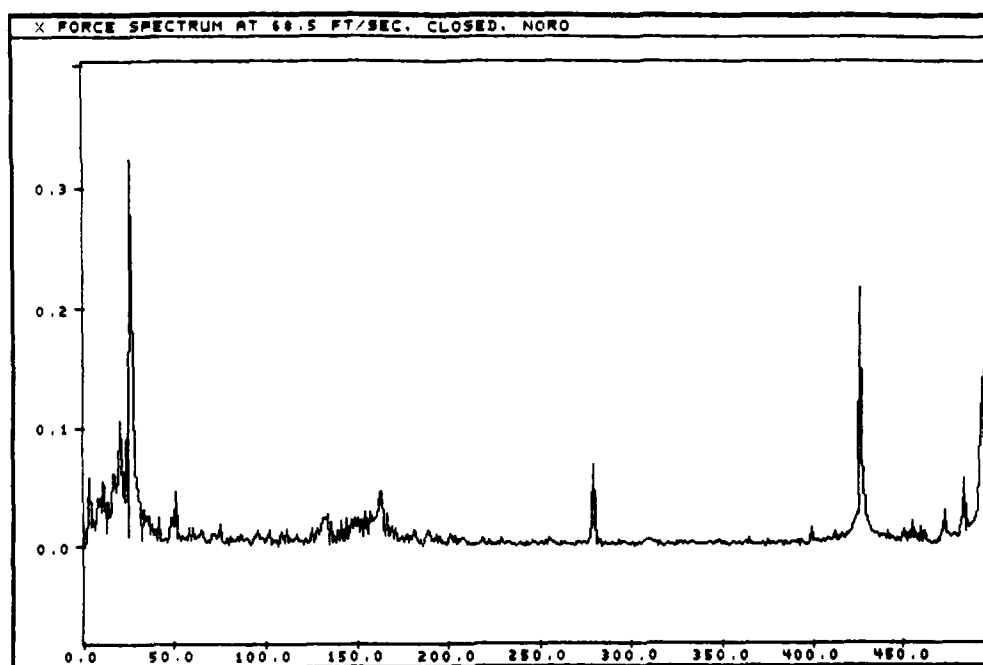
Figure 5.1 X Force Spectrum at 68.5 ft/s, Closed, NORO
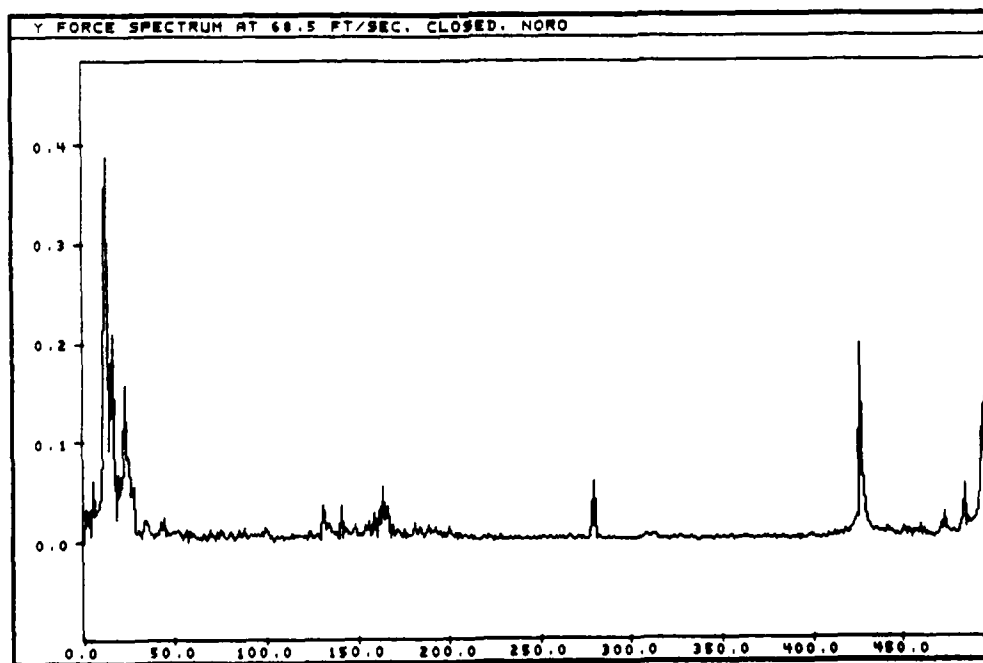
Figure 5.2 Y Force Spectrum at 68.5 ft/s, Closed, NORO

67
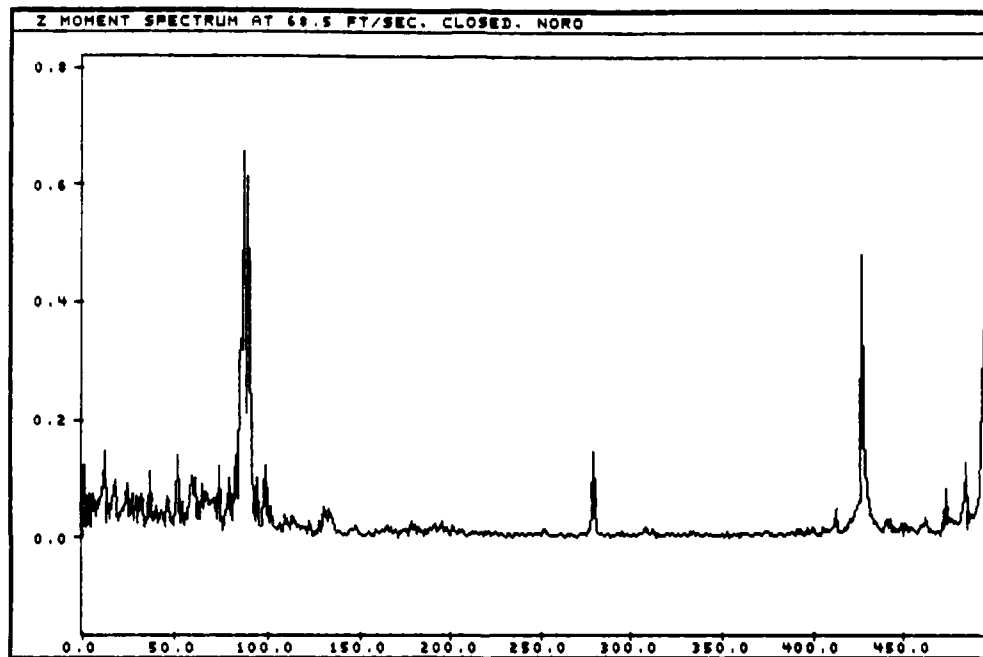
Figure 5.3   Z Moment Spectrum at 68.5 ft/s, Closed, NORO
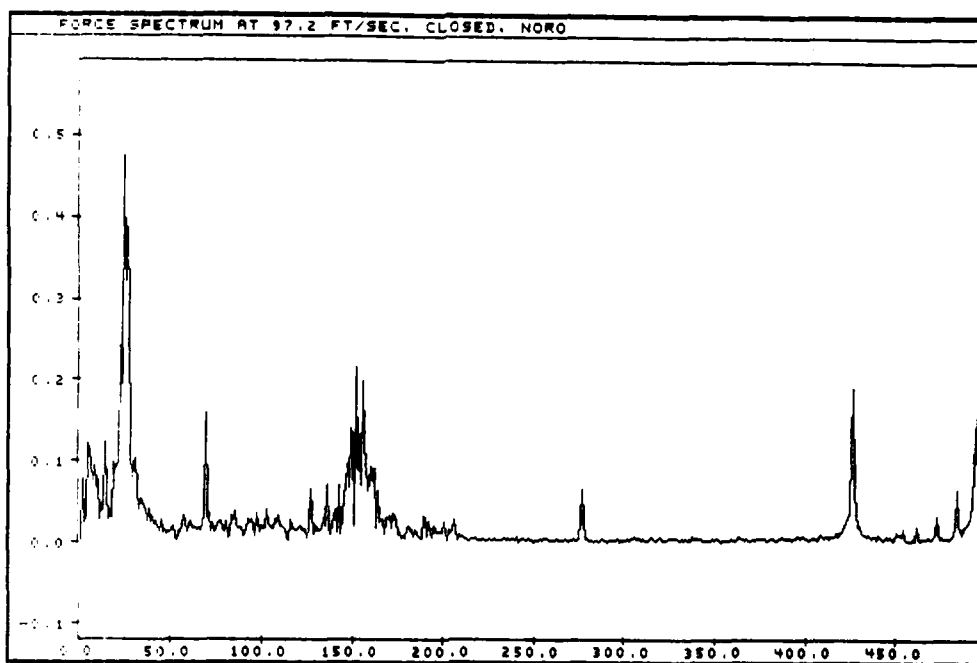
Figure 5.4   X Force Spectrum at 97.2 ft/s, Closed, NORO
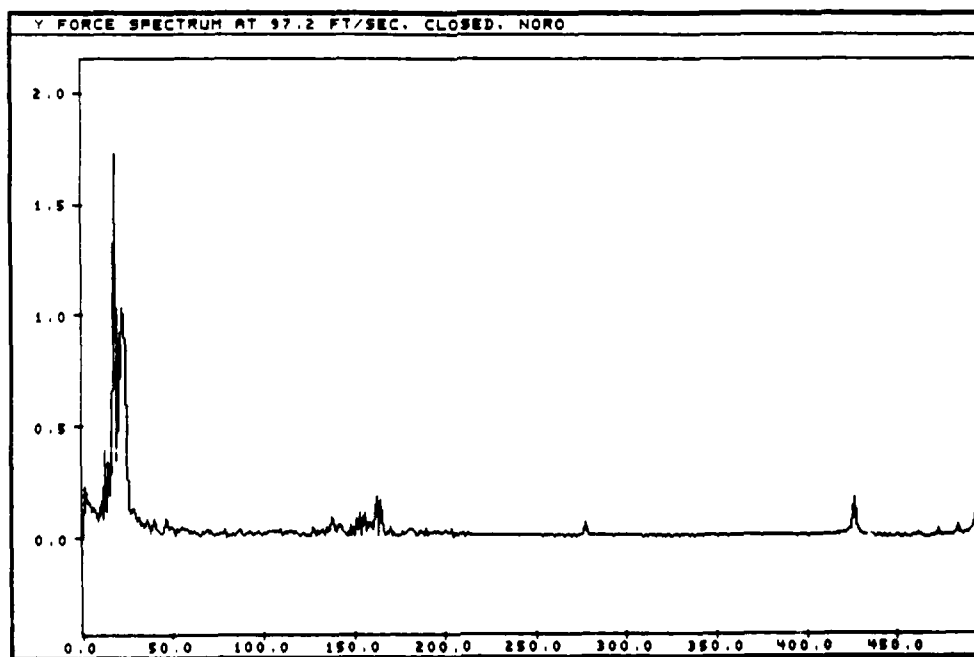
Figure 5.5   Y Force Spectrum at 97.2 ft/s, Closed, NORO

69
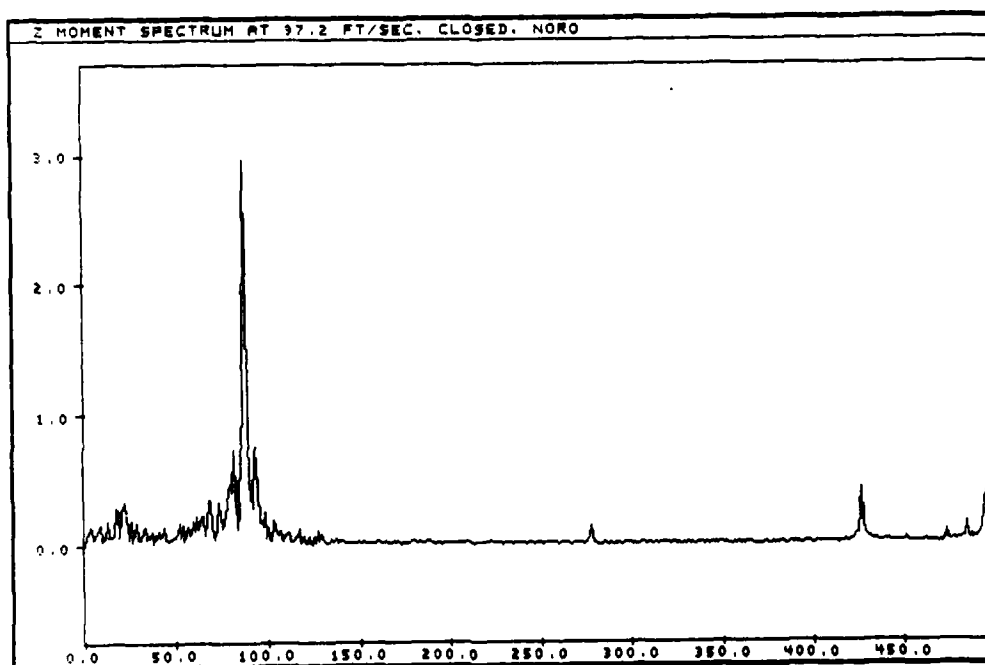
Figure 5.6   Z Moment Spectrum at 97.2 ft/s, Closed, NORO

Looking at the low speed data first, Figures 5.1 is a spectrum of the transient X-force at 68.5 ft/s. This figure shows a predominant 21 Hz spike. The additional frequency spikes seen above 400 Hz are representative of higher modes of the model. These high frequencies should have been filtered out by the MDAS "F2" input card which was set at a cut off of 200 Hz. However, a post test check of the "F2" input cards showed the filters on the fourth card were not functioning properly. Thus, all frequency components were measured on load cell channels 6 and 7. Despite the presence of these high level spikes in the data, the magnitudes at higher speeds are low enough to ignore compared to the predominant model natural frequencies and the low shedding frequencies of interest.

Figure 5.2 shows the frequency spectrum for the Y-force component. Here the 21 Hz signal is seen, but a higher magnitude component is also present at 12 Hz. This 12 Hz signal appears to be a result of vortex shedding from the model, since this frequency spike proved to be a function of air speed.

The Z-moment frequency spectrum is shown in Figure 5.3. Here the second mode natural frequency of 87 Hz is clearly seen, dominating all other frequencies.

As the air flow speed increased, so did the magnitudes of the various frequency components. The predominant vibrations are seen in the Y-force and Z-moment terms. This predominance can be seen in the spectrum magnitude plots shown in Figures 5.4 through 5.6 as compared to the corresponding spectrums in Figures 5.1 through 5.3   For the speed

71

increase of approximately 42 percent, Figure 5.4 shows an X-force spectrum magnitude increase of about 48 percent. In comparison, the Y-force component increase was approximately 330 percent, (shown in Figure 5.5) and the Z-moment increase was around 340 percent (shown in Figure 5.6).

A closer look at Figure 5.5 shows the vortex shedding induced force frequency is now at 18 Hz. As the speed is increased, excitation of the model first mode also increases and the vibrations become more a function of the natural frequency instead of the actual shedding frequency. Thus, for any speed above this point, the actual shedding frequency input to the model may be higher. But the sensed input frequency will be a constant 21 Hz due to the synchronization and "lock-on" discussed in Chapter I.

Since all of the configurations tested (except the NORO closed configuration) showed natural frequency values as the predominant frequencies in the spectrums, the actual representation of wind induced vibrations (instead of model natural frequency mode vibrations) is questionable in the transient data. In the NORO closed configuration, some shedding induced forces were measurable, but only up to the natural frequency of 21 Hz mentioned above. The magnitudes of the standard deviation values in the force and moment directions of the natural frequencies appear to be biased by these frequencies, thus masking the true aerodynamic vibration inputs. Despite the questionable nature of the standard deviation values, they are plotted along with the mean values for completeness since they may prove helpful to another researcher with similar limitations.

Initial testing of the cube model was intended to verify the results obtained at the USAF Academy tunnel (14:1-12). The USAF Academy test configuration was an 8 inch cube mounted on a sting balance extending from the flat bottom of the tunnel, facing head-on in the the air flow. Speeds tested were between 50 ft/s and 180 ft/s, with no turbulence generation. Drag force data from this test are presented in Figure 5.7, in terms of the wind coordinates defined in Chapter IV. A line connecting these points off sets them from the other points. AFIT test data for the NORO closed configuration are plotted against the USAF Academy results. The deviation of the mean NORO values from the USAF Academy data appears to be a direct result of the 1/4 inch gap around the AFIT model assembly (this gap exists to allow the model freedom to move in the closed configuration). If the gap did not exist, the AFIT data would most likely lie on top of the USAF Academy data. The apparent impact of the 1/4 inch gap is an increase in the mean drag at low speed with a transition to normal drag values above 100 ft/sec. As for the standard deviation values, results appear to parallel USAF Academy results until the synchronization with the natural frequency occurs.

Data for the 45RO closed cavity configuration is also plotted in Figure 5.7. The mean values of C_{D_x} appear constant between 1.27 and 1.29, about 0.1 lower than the NORO values. And standard deviation values appear 0.05 lower than the NORO values.

Figure 5.8 is a plot of the side force coefficient standard deviation versus tunnel speed for the USAF Academy data along with the AFIT NORO and 45RO closed configurations data. Results from the USAF Academy

73
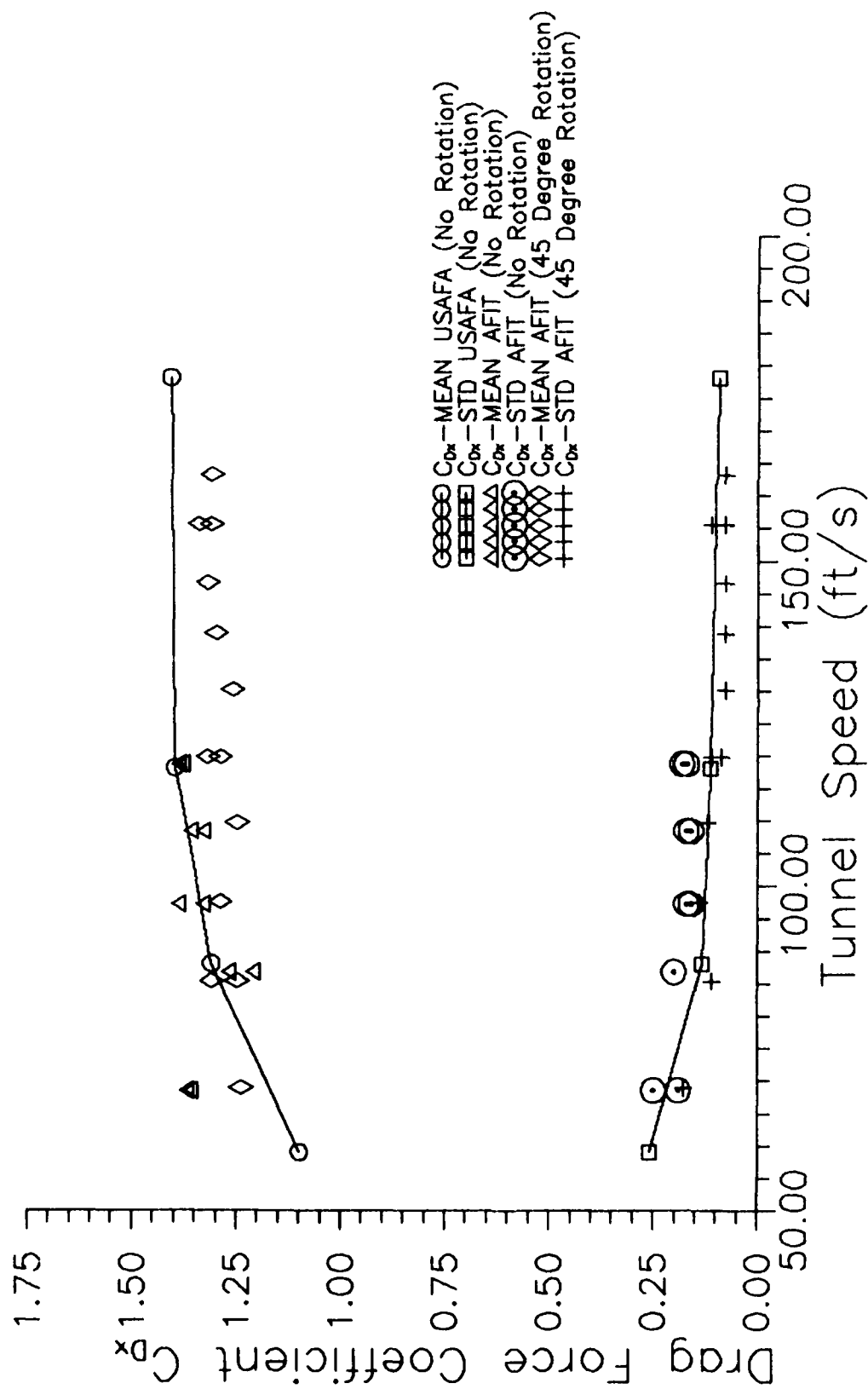
Figure 5.7 Drag Coefficient Comparison with USAF Academy Data
(Closed Configurations)

74
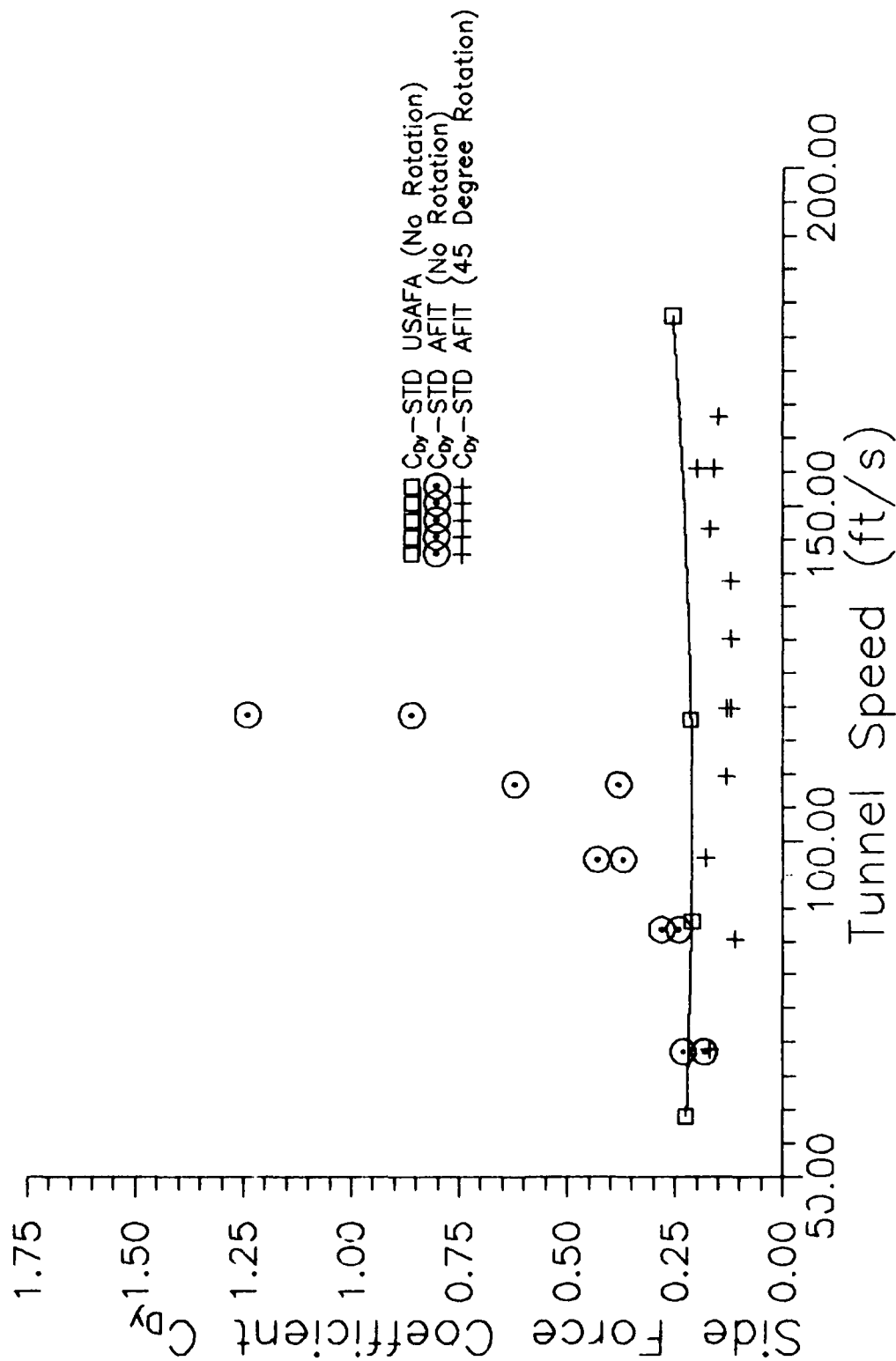
Figure 5.8 Side Force Coefficient Comparison with USAF Academy Data
(Closed Configurations)

show the standard deviation of C_{D_y} to be a constant value around 0.23, while AFIT NORO closed configuration results show a sharp rise with speed from 0.24 at 68.5 ft/s to 1.25 at 118.6 ft/s. This rise is attributed to excitation of the first mode and is supported by Y-force frequency spectrum analysis which shows this steady rise in the first mode magnitude with tunnel speed (see Figures 5.2 and 5.5). The first mode is apparently excited by vortex shedding off the back corners of the model, along with the air flow as is passes along the narrow gaps between the model and cavity side walls. The formation of upstream vortex (as shown in Figure 4.3) and resulting horseshoe vortex around the base of the model would appear to create turbulence in the small gap around the model. This vortex generated turbulence in conjunction with the abrupt contour changes of the cavity and the trailing edge vortex shedding could set up this driving force. Because of this first mode excitation, periodic high warning limits were measured on two of the base load cells during test. Thus, the reason for the limited number of data points for this configuration.

Results of the 45RO closed cavity configuration are also plotted in Figure 5.8. These values appear steady over the speed range, paralleling the USAF Academy data with values approximately 0.08 lower. Since these C_{D_y} values appear steady with speed, it is apparent that the 45RO configuration is more aerodynamically stable. This is as expected since air flow is smoothly divided on either side of the model, and can flow into and out of the cavity with less turbulence, as discussed in Chapter IV with Figures 4.10 and 4.11.

The effects of the cavity openings on the q_{local} value are presented in Figures 5.9 and 5.10, respectively representing the NORO and 45RO configurations. For the NORO configuration, the slope between local and tunnel dynamic pressure shows an increase from 0.995 for the closed cavity slope to 1.032 for the 4 inch open cavity, while the 8 inch opening q slope is 1.044. Similar results are found for the 45RO configuration where the changes from the closed cavity slope of 1.040 are 1.056 for the 4 inch cavity and 1.061 for the 8 inch. These changes are less than half those for the NORO case, tending to indicate the cavity opening has more of an impact on reducing upstream effects for the NORO configuration over the 45RO configuration. The impact of the cavity opening on reducing the upstream effects can be seen in Figures 4.13 and 4.15 in Chapter IV. In the closed cavity NORO configuration pictured in Figure 4.15, oil streaks upstream of the 4 inch cavity plate show flow divergence to the left and right. When this cavity is opened (as shown in Figure 4.13) these same oil streaks show a more parallel flow approaching the cavity and model, leading to the conclusion of reduced upstream effects. These overall shifts in q slope amount to a 5 ft/s variation in measured velocity, which is less than the potential error from the actual manometer readings at ± 0.07 inches of water (± 6 ft/s). Thus, the actual measured q values for each configuration is acceptable for use.

Figures 5.11 through 5.16 are plots for the NORO configuration force and moment coefficients versus local tunnel speed. Both the mean and standard deviation values are plotted for the three cavity inserts.

77
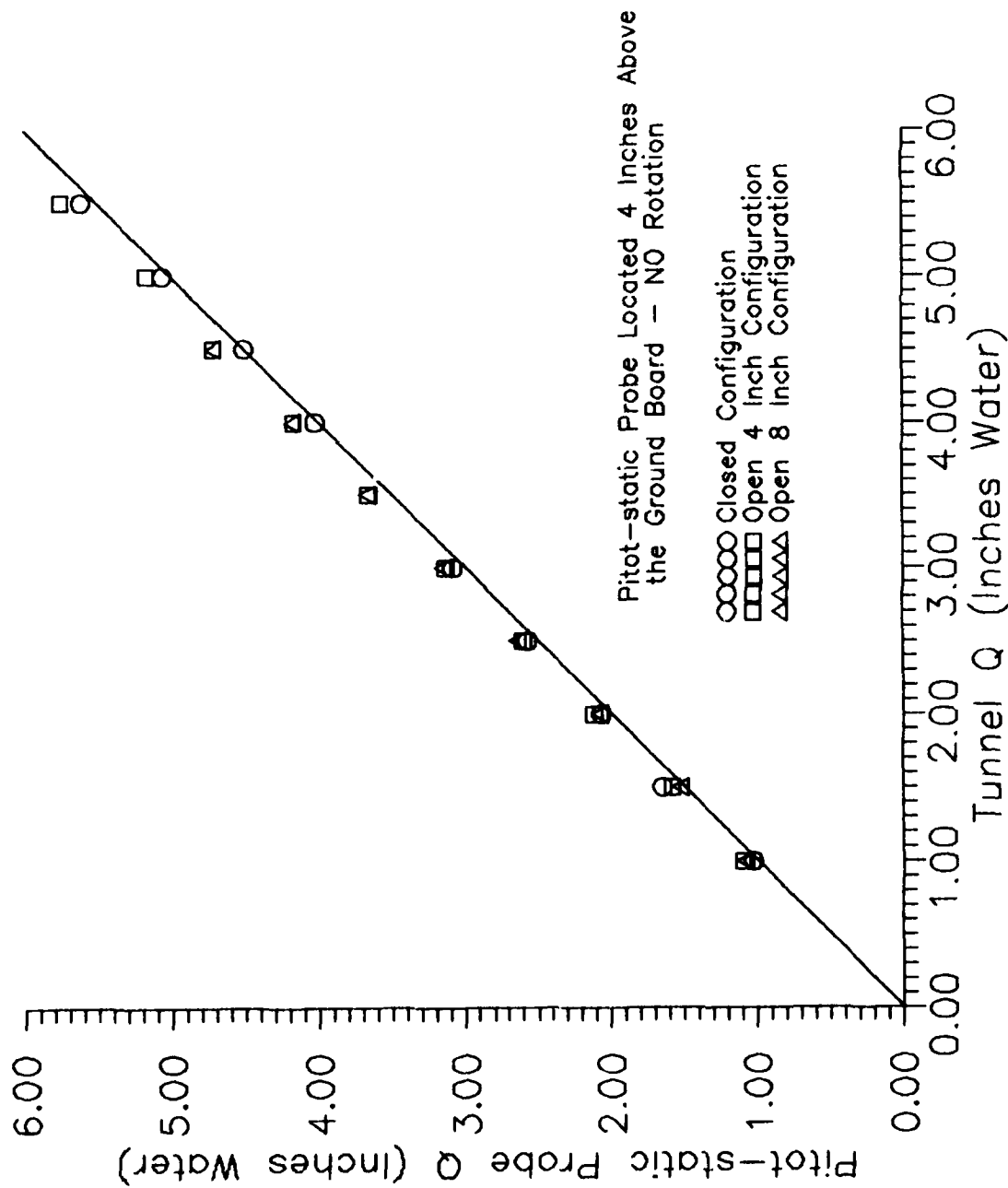
Figure 5.9   Dynamic Pressure Variation With Cavity Selection
(Average Pitot-static Probe Values vs.Tunnel)

78
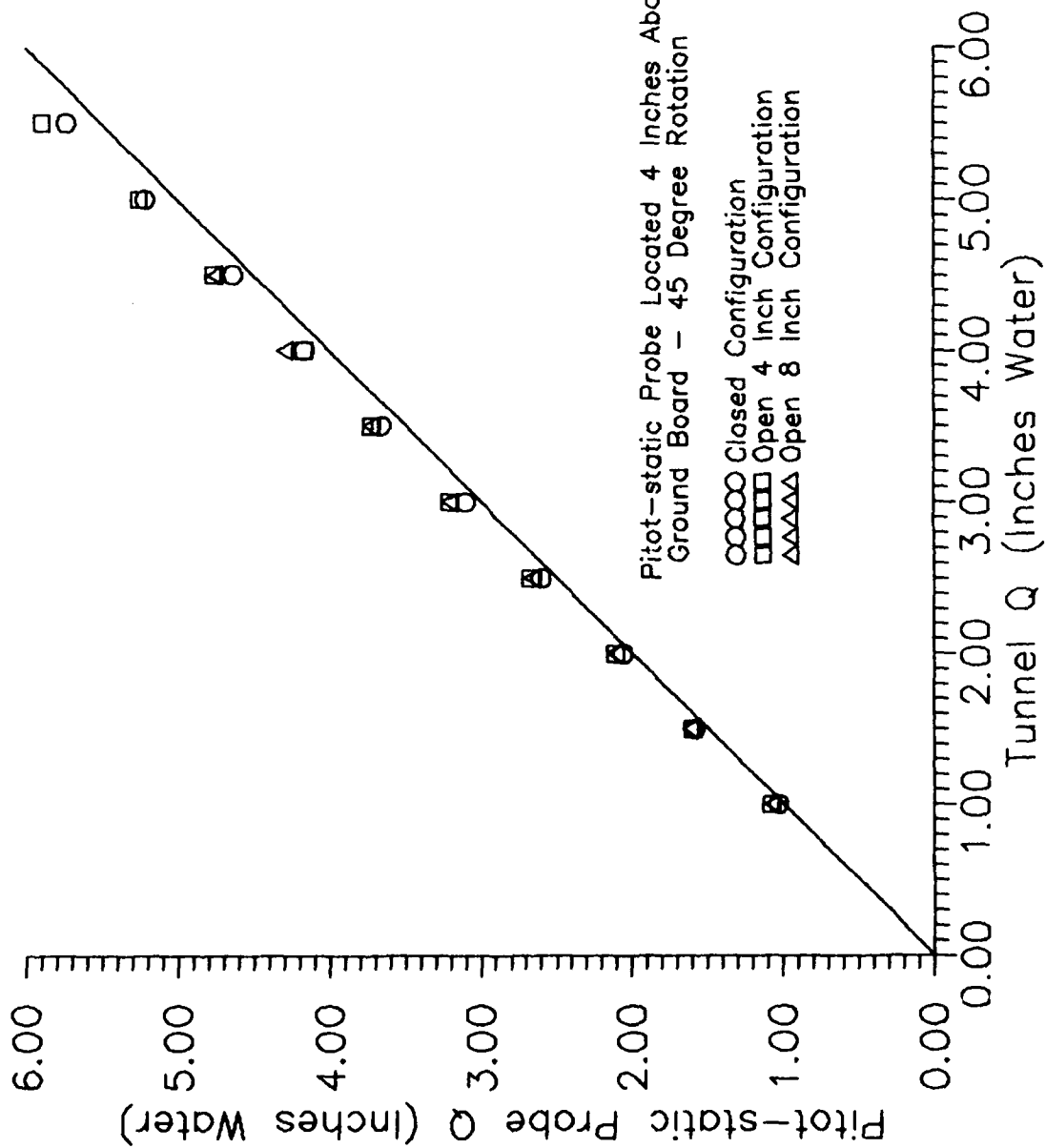
Figure 5.10 Dynamic Pressure Variation With Cavity Selection
(Average Pitot-static Probe Values vs.Tunnel)
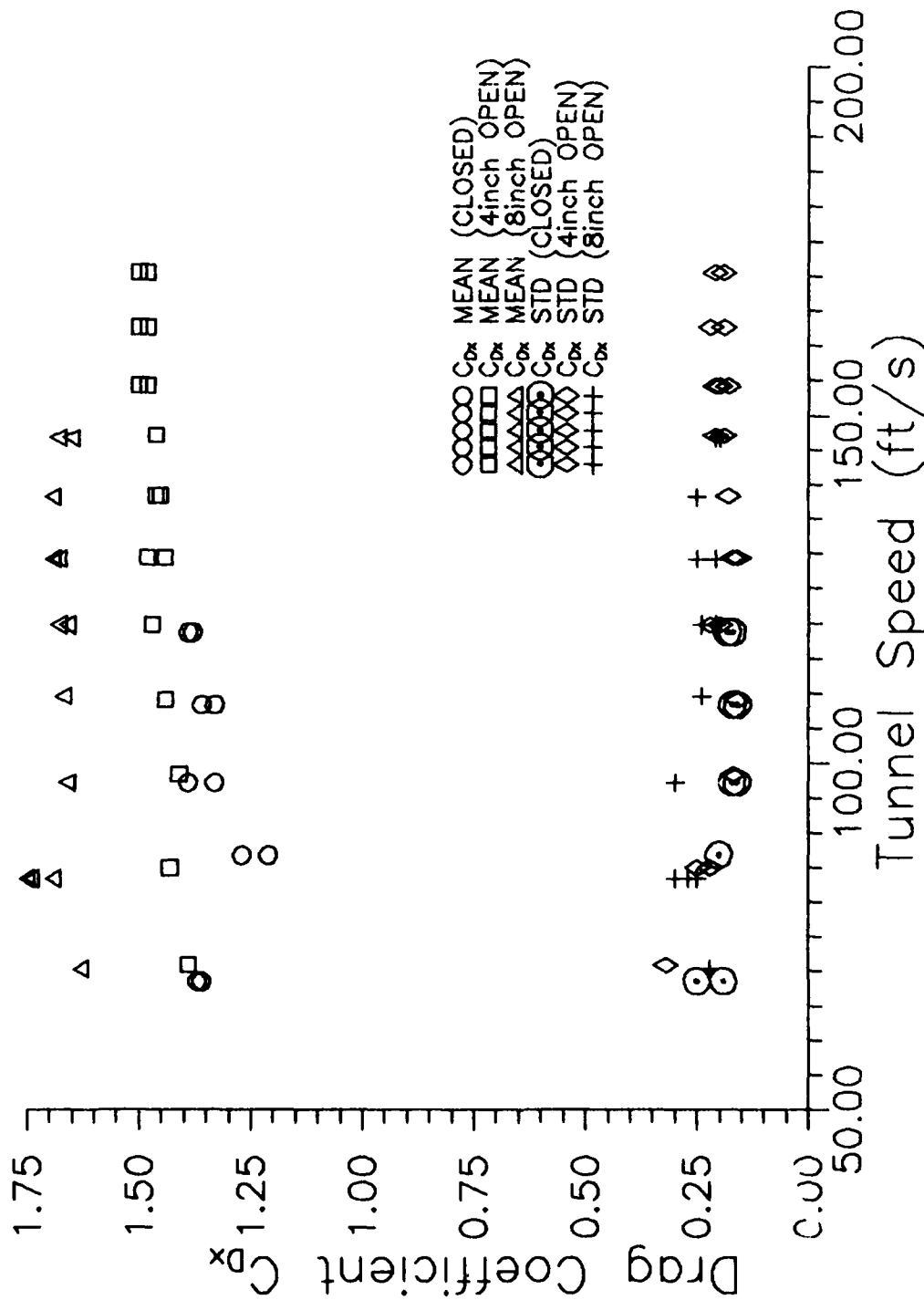
Figure 5.11 Drag Coefficient Variation with Cavity Configurations
(No Rotation of Model)
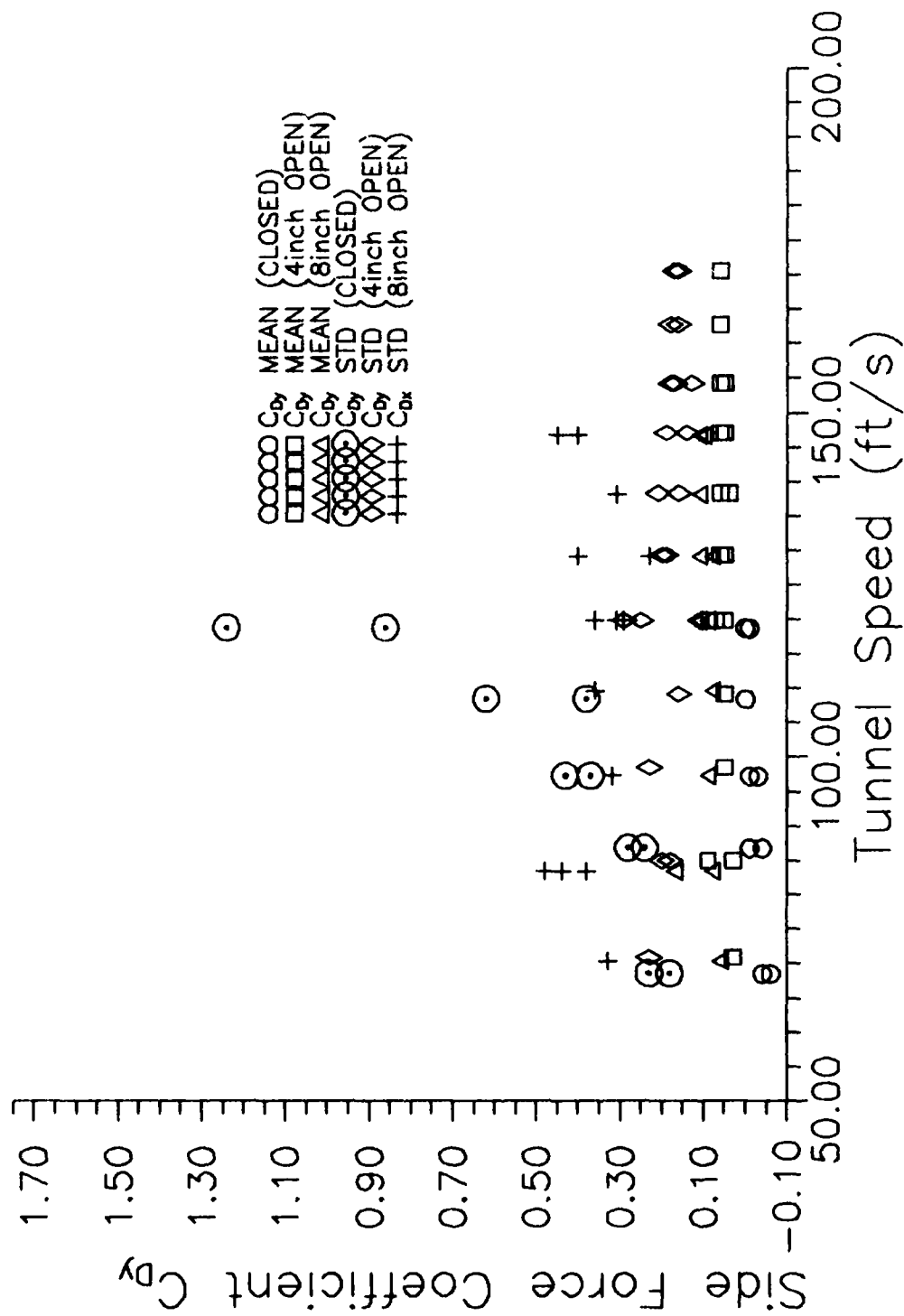
Figure 5.12   Side Force Coefficient Variation with Cavity Configurations
(No Rotation of Model)
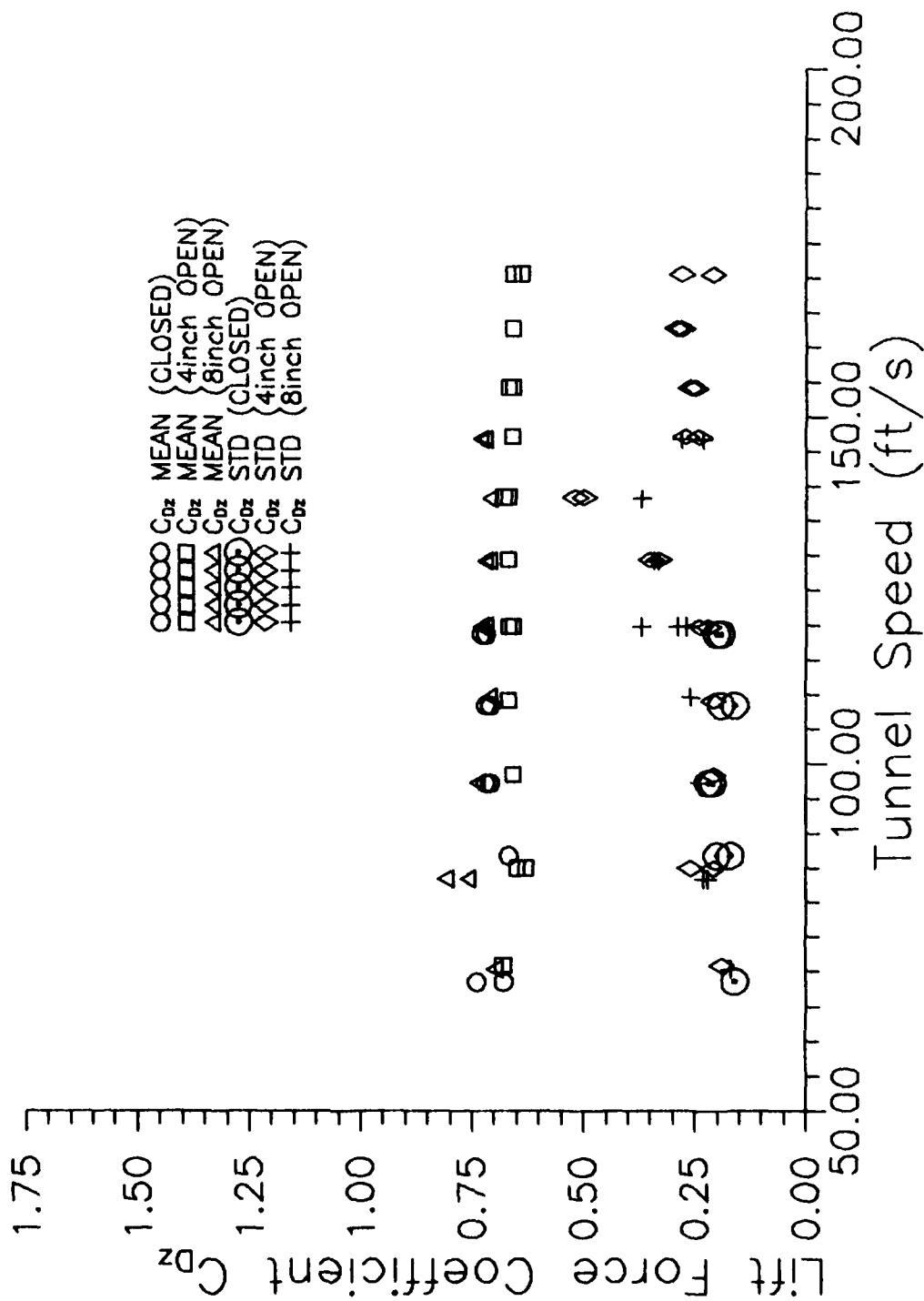
Figure 5.13 Lift Force Coefficient Variation with Cavity Configurations
(No Rotation of Model)
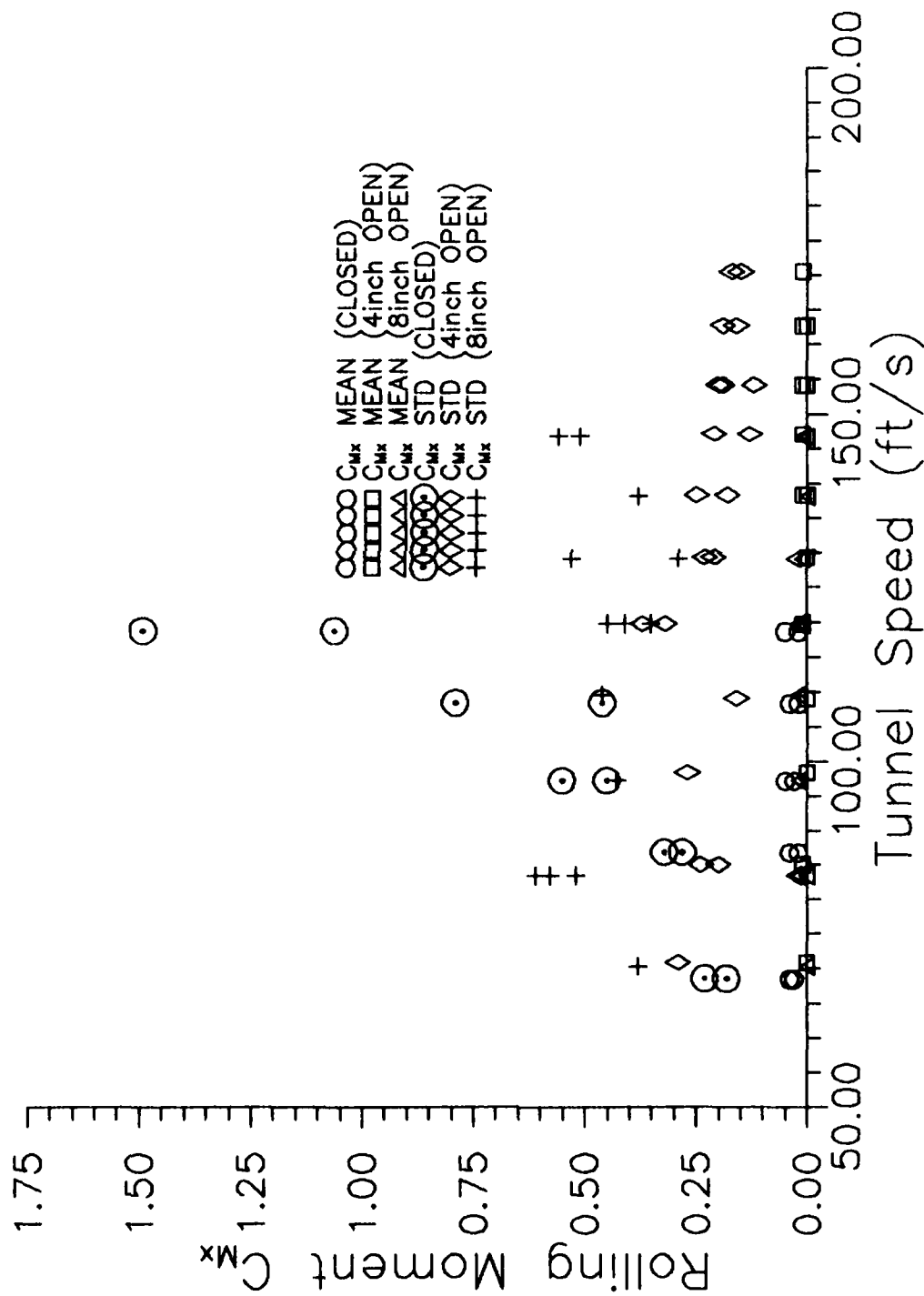
Figure 5.14   Rolling Moment Coefficient Variations with Cavity Configurations
(No Rotation of Model)

83
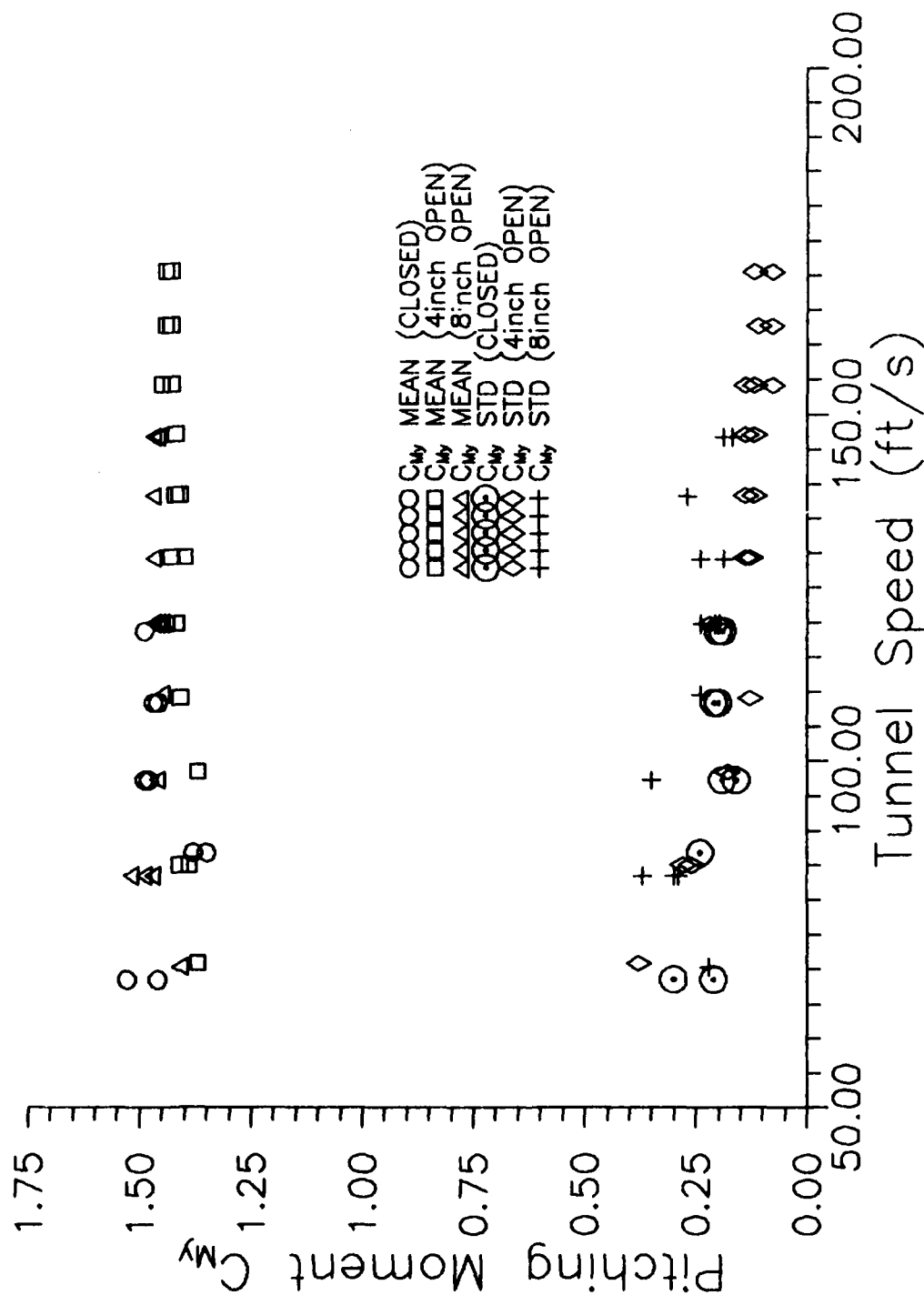
Figure 5.15   Pitching Moment Coefficient Variations with Cavity Configurations
(No Rotation of Model)
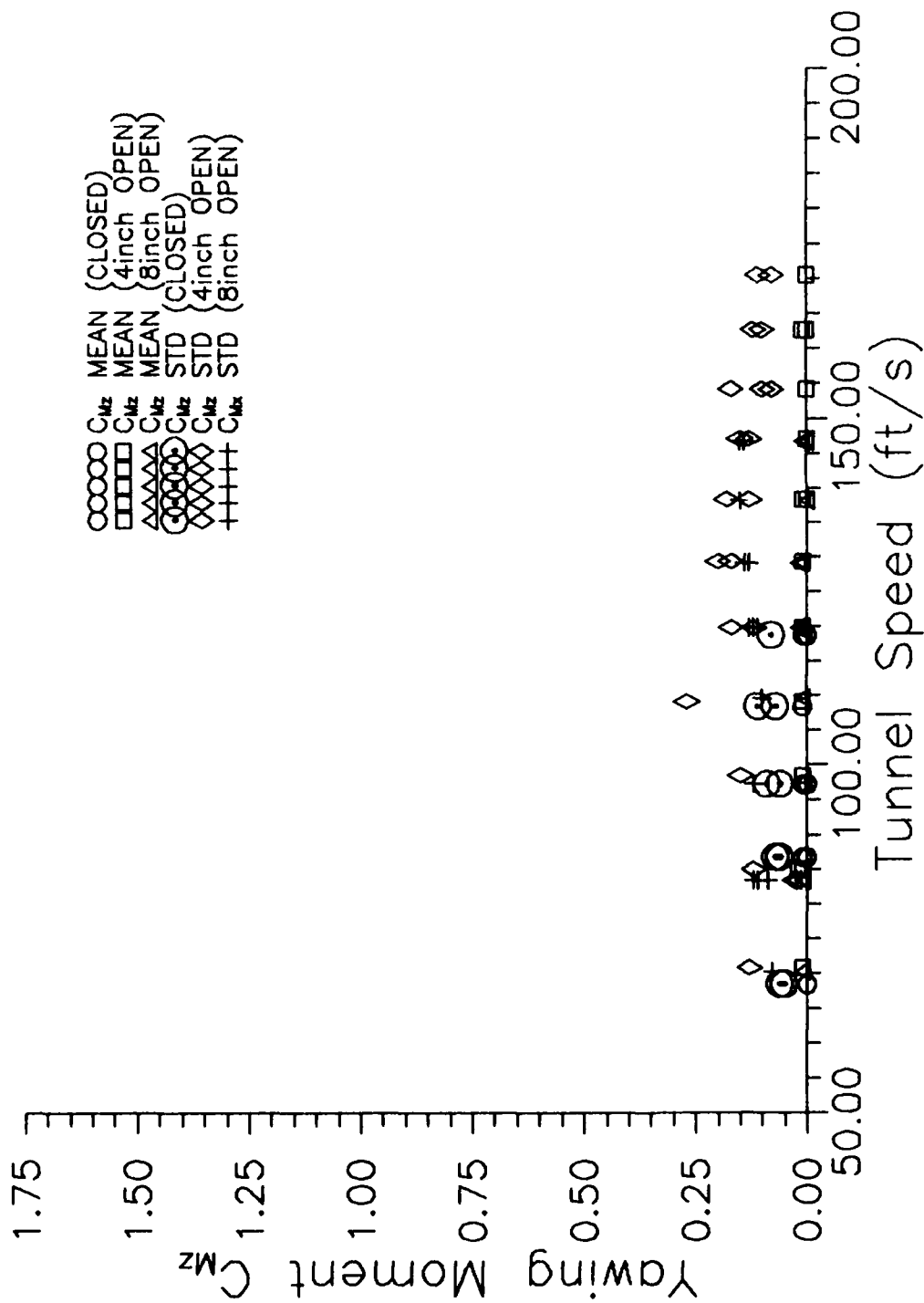
Figure 5.16 Yawing Moment Coefficient Variations with Cavity Configurations
(No Rotation of Model)

As mentioned earlier, the standard deviation values may be questionable due to the natural frequency vibrations.

The drag coefficients are plotted in Figure 5.11. In this figure, the closed cavity values are the same ones seen and discussed in Figure 5.7. With the 4 inch and 8 inch open cavity data included, one can see the effects the cavity has at increasing the C_{D_x} values. The apparent trend of mean C_{D_x} values is a gradual increase with speed for each configuration, and a positive shift in values as the cavity is opened. Based on an assumed mean value of 1.35 for closed cavity, the 4 inch opening causes an 0.05 increase in C_{D_x} values, while the 8 inch opening leads to a 0.31 increase. This increase in the mean C_{D_x} values can be attributed to the increased surface area exposed to free stream air as the cavity is opened. The actual exposed area is not known, thus the C_{D_x} values are based on the fixed reference area above the ground board plan.

The data in Figure 5.7 also supports the idea that the cavity act as a buffer region between the cavity walls and the model. As this cavity is opened, the turbulent regions around the base of the model (as discussed in Chapter IV) may dissipate due to the increased free stream flow which is able to enter the cavity. This would be similar to the effect discussed for the 45RO configuration in Figure 5.8 where the model rotation was rationalized to have caused a reduction in turbulence by enabling air flows to enter into and out of the cavity more easily.

86

Figure 5.12 shows the mean side force coefficients to be close to zero, as is expected in a uniform flow field. The deviations of these mean values from zero are partially due to sensitivity of the LCU near zero along with actual flow field deviation, as mentioned in Chapter IV. The standard deviation values for the closed cavity configuration are the same as shown in Figure 5.8. These values appear to represent the vortex shedding up to a speed of approximately 120 ft/s as mentioned at the beginning of this chapter with Figures 5.2 and 5.5. Above this speed, the natural frequencies of the model dominates the spectrum, and further dissemination of the true wind induced values is not possible. As for the open cavity cases, the natural frequencies dominate the values over the speed range with variations due to the model vibratory modes instead of the wind induced vibration. The main conclusion from this data show no significant impact of the cavity opening on the side loads.

Figure 5.13 illustrates the effects of the cavity openings on the model lifting force coefficients. For all three cavity openings, the mean lift coefficient remains fairly constant over the speed range between 0.65 and 0.70. This lift force is probably due to a higher pressure region inside the cavity in reference to the pressure field setup by the flow moving across the ground board surface. An additional contribution may be due to air flow under the model, in the region of the LCU. Around the base of the model, there exists a 1/8 inch gap to allow freedom of movement. This gap could allow air swirling round the base

of the cavity to flow underneath the model, contributing to the lift force.

Examination of the standard deviation values show spike occurring at a velocity of approximately 138 ft/s. A check of the Z force frequencies revealed two major frequency components. The first was a steady 116 Hz component seen at all speeds. This component appears to be a model assembly mode not detected in the pre-test analysis. The second frequency component proved to be a function of air speed. At 120 ft/s, this Z-force frequency component was 83 Hz. As tunnel speed was increased, both magnitude and frequency increased, peaking at a speed of 138 ft/s. The peak frequency was 95 Hz with a magnitude increase approximately 5 times the 120 ft/s setting. Above this speed, the frequency spike dissipates and the primary 116 Hz signal dominates again. These events can be seen in Figures 5.17 through 5.20 which are the frequency spectrums for the Z-force of the speeds discussed. As with the previous spectrum plots, the mean value has been subtracted off the signal before spectrum processing. This apparent excitation and dissipation is most likely due to a resonance underneath the model in the LCU cavity.

Figure 5.14 is a plot of the rolling moment coefficient versus local tunnel speed for the three NORO cavities. As would be expected, the moment data plotted in the figure matched the trends shown by the Y-force data plotted in Figure 5.12. In Figure 5.14, the standard deviation values for C_{M_x} in the closed cavity case show the same rapid increase with velocity as was seen for the closed cavity C_{D_y} standard
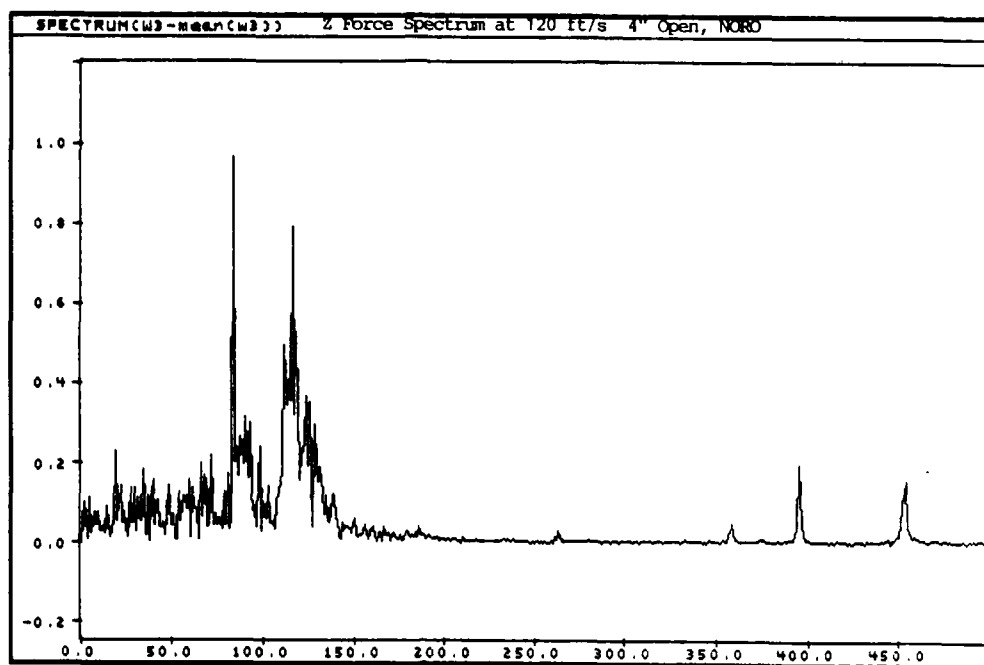
Figure 5.17   Z Force Spectrum at 120 ft/s, 4" Open, NORO
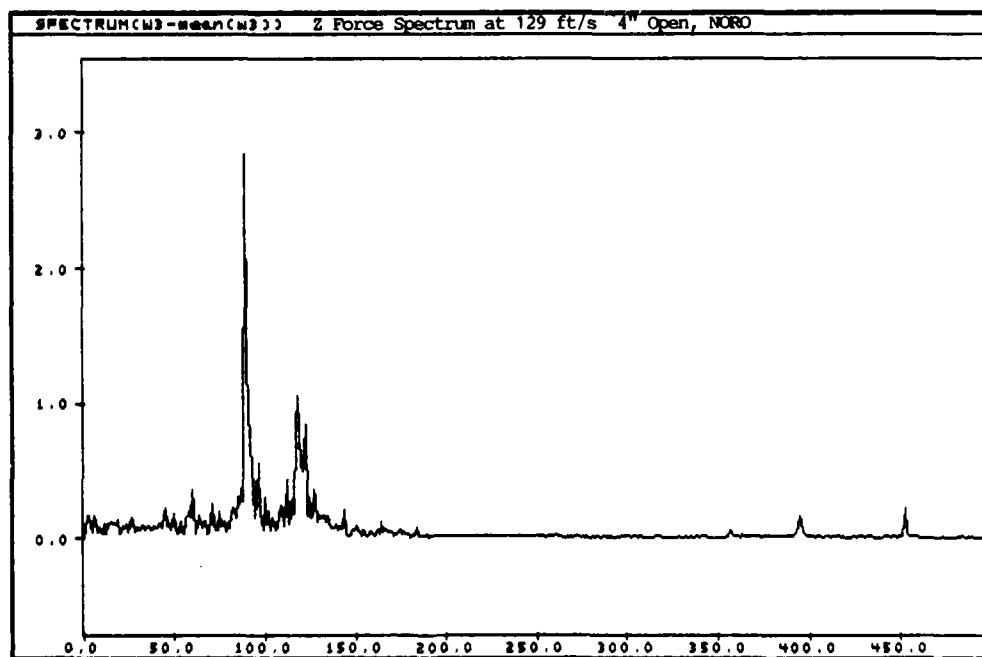
Figure 5.18   Z Force Spectrum at 129 ft/s, 4" Open, NORO

89
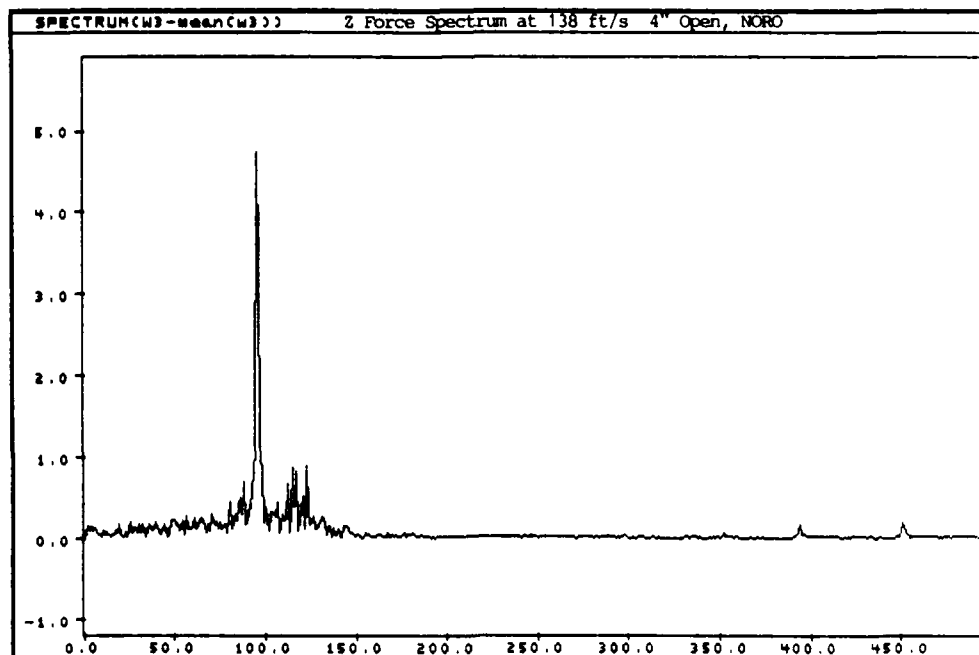
Figure 5.19 Z Force Spectrum at 138 ft/s , 4" Open, NORO
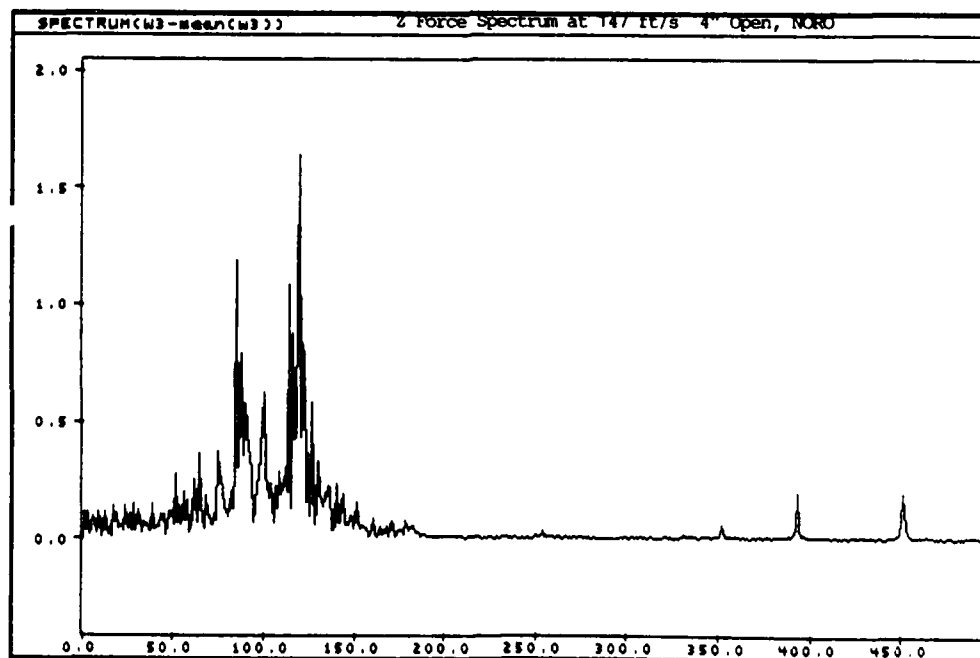
Figure 5. 20 Z Force Spectrum at 147 ft/s, 4" Open, NORO

90

deviation values in Figure 5.12. Mean C_{M_x} values lie between zero and 0.05 for all three cavity openings, indicating no significant changes in the mean C_{M_x} value with cavity opening. This result is the same conclusion reached from the mean C_{D_y} data shown in Figure 5.12.

The pitching moment coefficients for the three NORO cavities are shown in Figure 5.15. As with the previous plots of C_{M_x} and C_{D_y}, both mean and standard deviation values of C_{M_y} match the respective data trends in their C_{D_x} counterparts shown in Figure 5.11. Mean values for C_{M_y} appear the same for all three cavity configurations, holding at approximately 1.44 over the speed range tested. Thus, these results lead to the conclusion that the cavity opening has no significant impact on the mean C_{M_y} values.

The last figure for the NORO configurations is the yawing moment coefficient shown in Figure 5.16. As is expected with the model symmetry about the Z-axis, all mean C_{M_z} values are zero. The standard deviation values tend to show a constant value of 0.1, independent of the cavity opening. Variations in these standard deviation values are dominated by the model second mode frequency at 87 Hz. This can be seen in the Z-moment frequency spectrums shown earlier in Figures 5.3 and 5.6. Since this 87 Hz frequency dominates the Z-moment spectrum over the entire speed range tested, these standard deviation values are more representative of the model vibrations rather than the true aerodynamic in-

puts. The overall conclusion from the yaw moment coefficients is that the mean values are constant with variation in cavity opening.

Figures 5.21 through 5.26 are plots for the 45RO configuration of the force and moment coefficients (referenced to wind coordinates) versus local tunnel speed. As with the NORO figures both mean and standard deviation values are plotted for the three cavity inserts, with the standard deviation values still being questionable due to natural frequency vibrations.

Figure 5.21 is the drag coefficient plot. In this plot, the mean C_{D_x} values show an increase with both speed and cavity opening, with cavity opening causing the largest change. For the 4 inch opening, the increase over the closed cavity values is 0.21, while for the 8 inch opening, the increase is 0.44. The mean C_{D_x} values for the 45RO closed configuration are about 0.1 lower than the NORO results in Figure 5.11. As the cavity is opened, the 45RO mean C_{D_x} values increase over the NORO values by about 0.03 in both the 4 inch and 8 inch cavity configurations. This rise in drag is attributed to increased model surface area exposed to the free stream air as the cavity is opened. In summary, the results presented in Figure 5.21 show that even though the rotation tends to reduce the mean C_{D_x} values, the cavity opening causes an increase in these values.

The standard deviation C_{D_x} values of Figure 5.21 are dominated by the 21 Hz first mode frequency at all speeds tested. The fluctuations seen are due to variations in the amplitude of this 21 Hz first mode

92
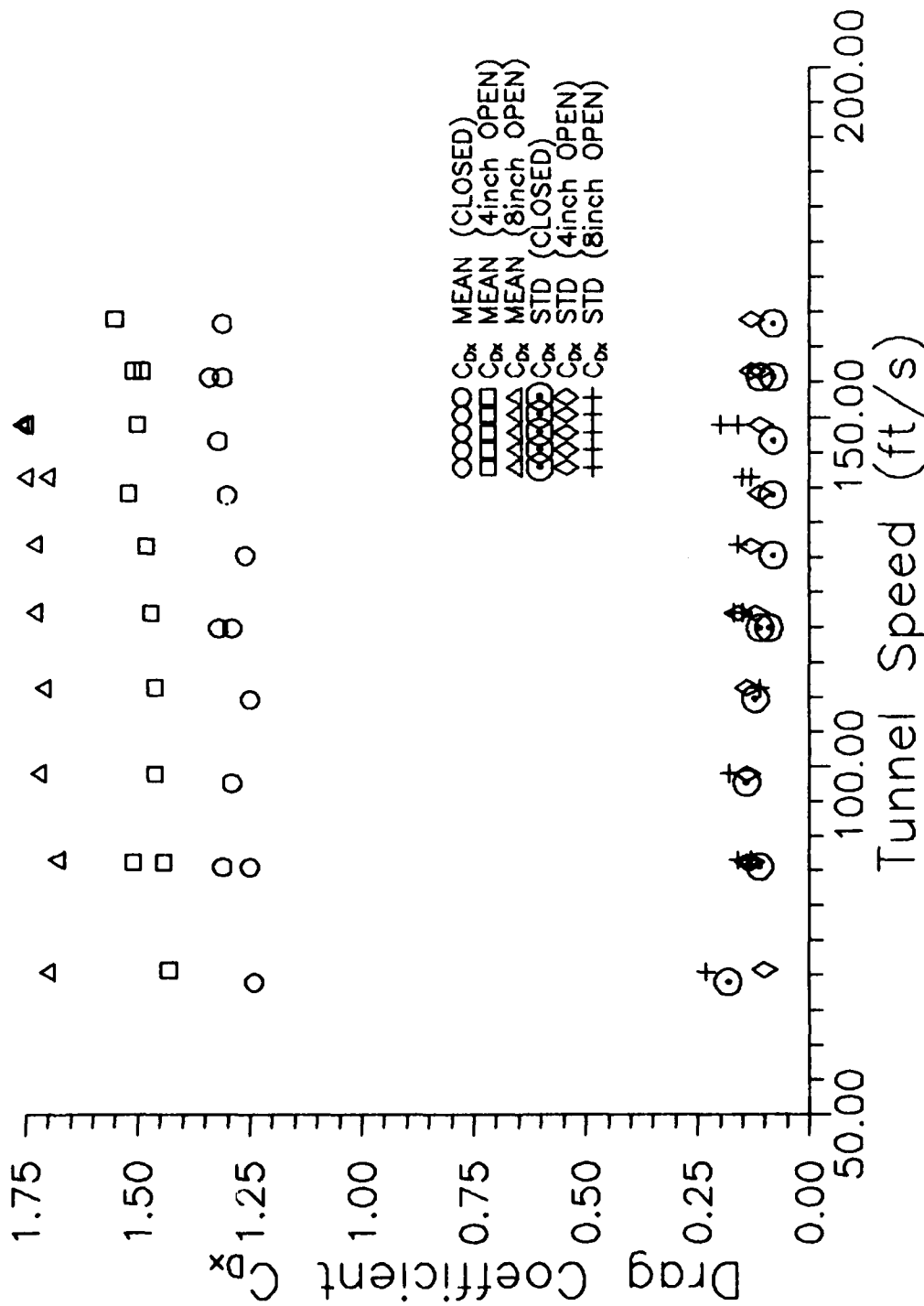
Figure 5.21 Drag Coefficient Variation with Cavity Configurations
(45 Degree Rotation of Model)
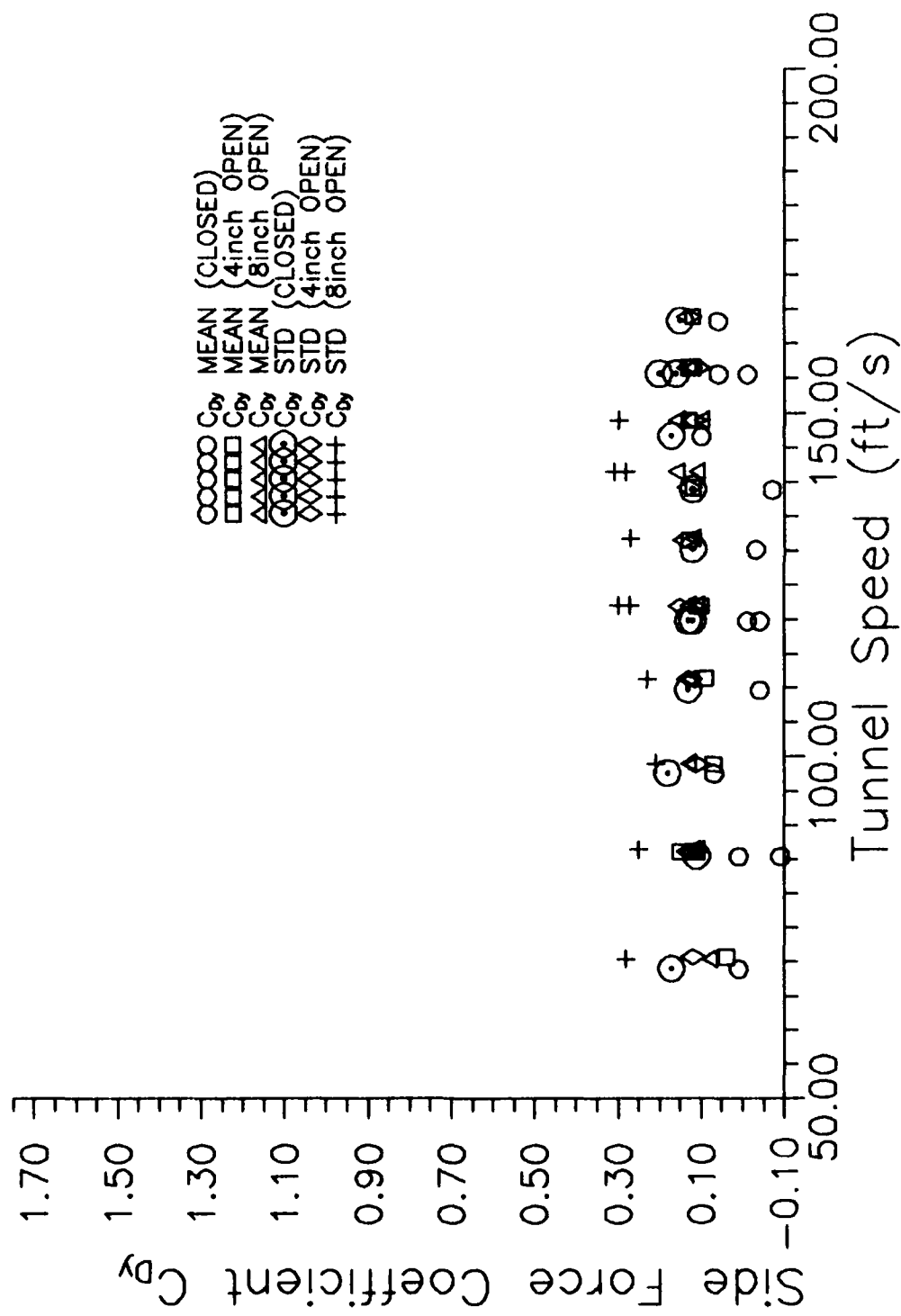
Figure 5.22 Side Force Coefficient Variation with Cavity Configurations
(45 Degree Rotation of Model)

94

Figure 5.23 Lift Force Coefficient Variation with Cavity Configurations
(45 Degree Rotation of Model)

95
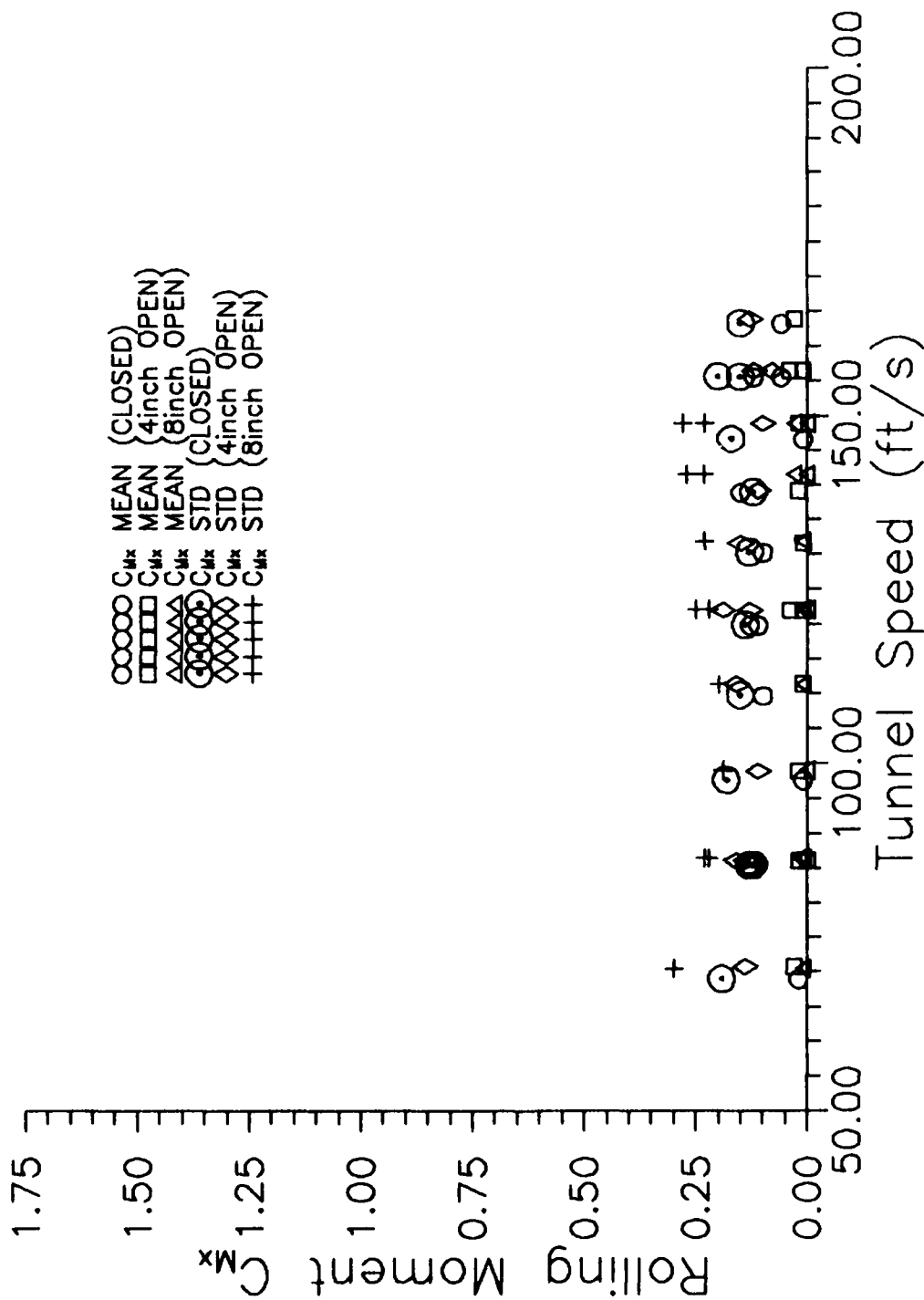
Figure 5.24 Rolling Moment Coefficient Variations with Cavity Configurations (45 Degree Rotation of Model)
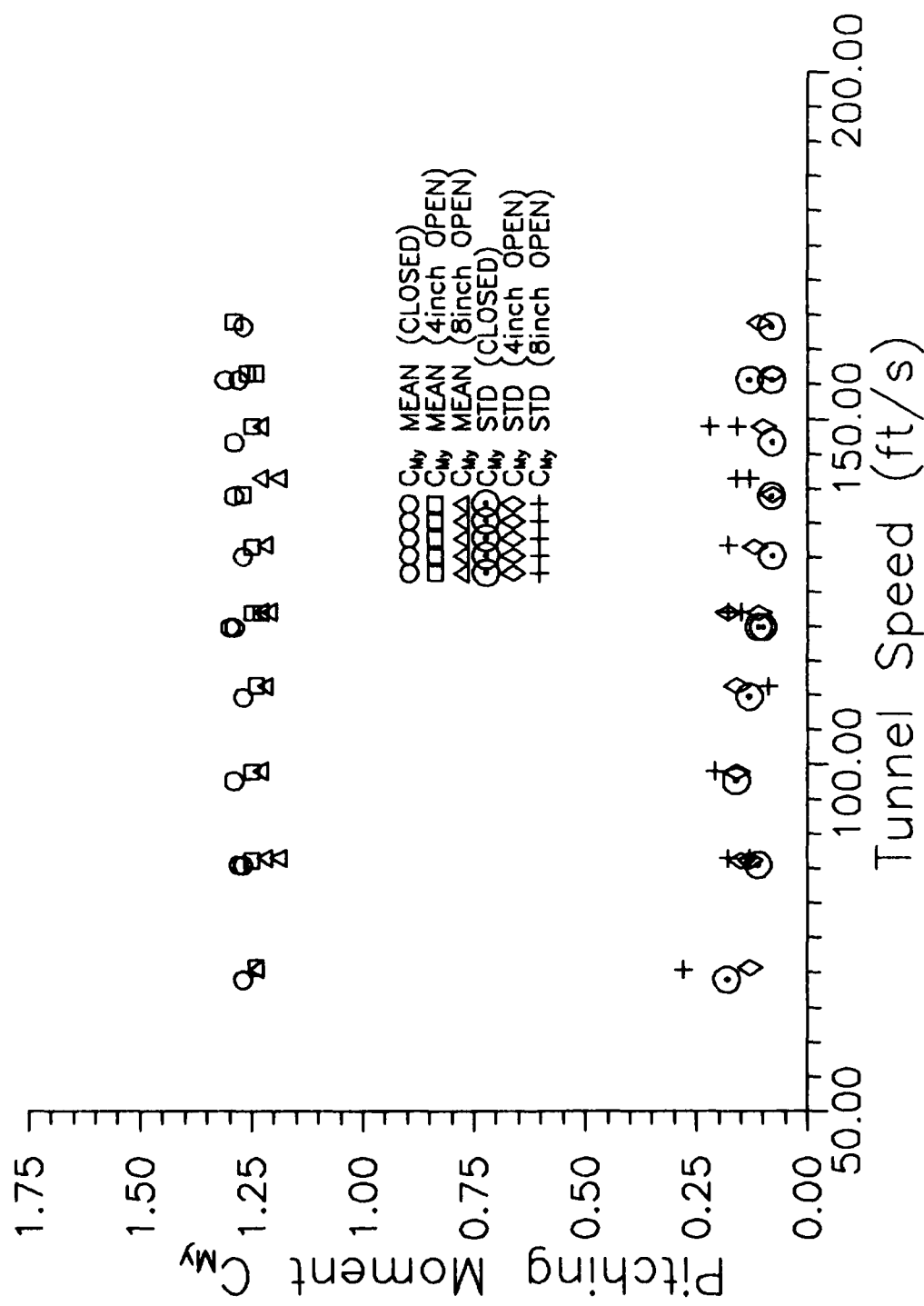
Figure 5.25   Pitching Moment Coefficient Variations with Cavity Configurations
(45 Degree Rotation of Model)
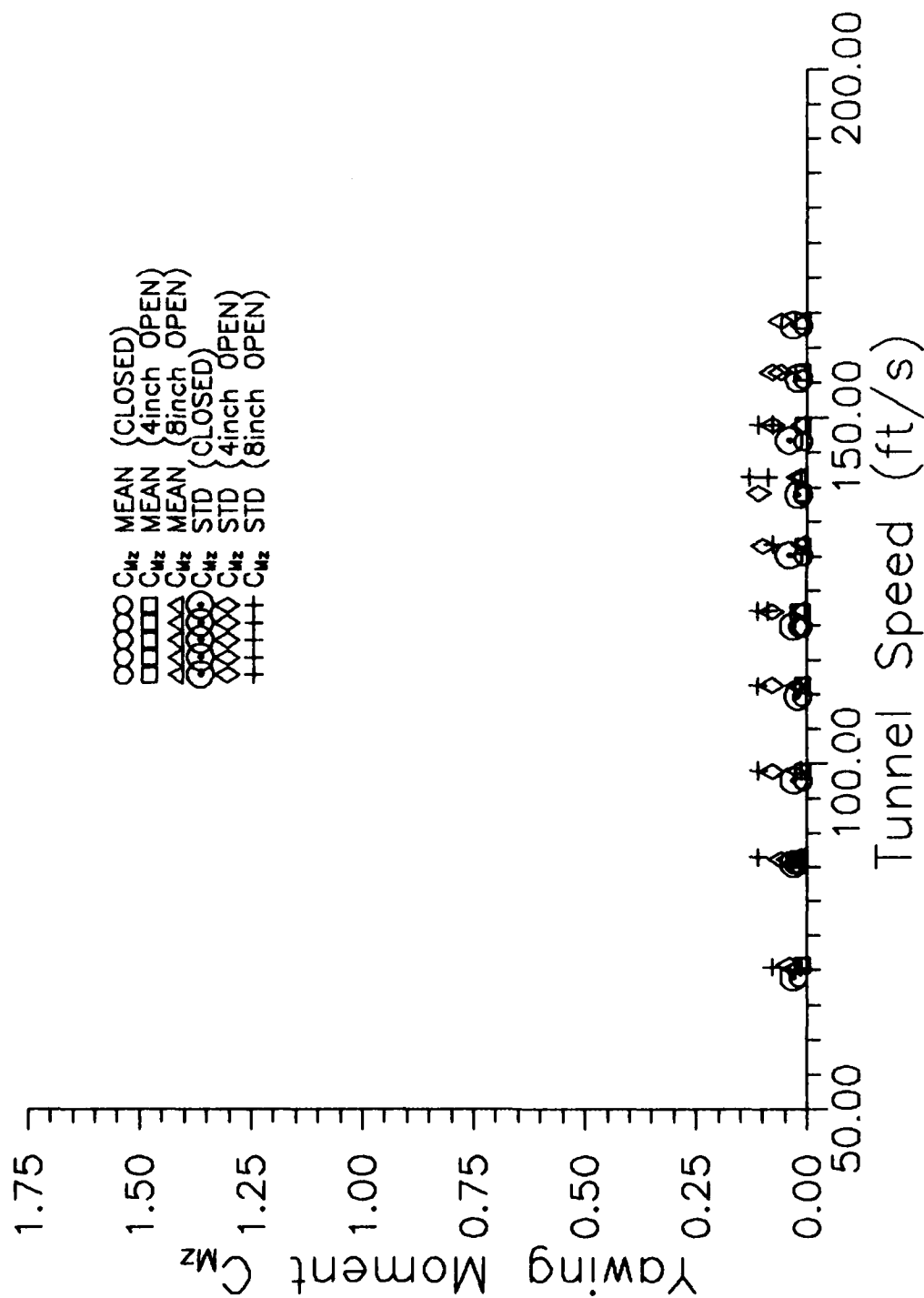
Figure 5.26 Yawing Moment Coefficient Variations with Cavity Configurations
(45 Degree Rotation of Model)

98

vibration. These same results are seen in the standard deviation C_{D_y} values of Figure 5.22. The 21 Hz signal was present in all data points, masking out any of the actual air induced vibrations which may have occurred.

The mean C_{D_y} values shown in Figure 5.22 appear to be close to zero, as would be expected in a symmetrical environment. The deviations from zero are most likely due to LCU sensitivity near zero and actual flow field deviations mentioned for the NORO case of C_{D_y}. Thus, the conclusion here is that the cavity opening has no significant impact on the mean C_{D_y} values.

Figure 5.23 represents the lift force coefficient for the 45RO configuration. The mean C_{D_z} shows a steady increase over the speed range and a definite reduction with the cavity opening. This reduction from the closed cavity configuration to the 4 inch cavity opening is approximately 0.26 while the drop for the 8 inch cavity is 0.45. This reduction in the mean lift force with the cavity opening could be attributed to the aerodynamic shape of the 45RO configuration. With the cavity and model at 45 degrees, the abrupt flow edges of the front and back cavity walls seen in the NORO configuration are now oriented more parallel with the free stream flow. Thus, flow over the ground board enters and exits the cavity more uniformly as the opening increases, leading to a potentially lower pressure differential and reduced lift on the model.

Flow penetration under the model is again the probable cause for the rise and fall of the standard deviation values between 122 ft/s and

149 ft/s. Figures 5.27 through 5.30 are frequency spectrums of the Z-force for the 45RO 4 inch open cavity configuration between 122 ft/s and 149 ft/s. As with the NORO case, two frequencies components are predominant, one holding a constant value while the other component increases in frequency with speed. The growth in magnitude of the shifting frequency value corresponds to the rise seen in standard deviation values in Figure 5.23. Thus, it is assumed some sort of resonance is occurring under the model in the LCU cavity.

The mean C_{D_z} values for the 45RO (Figure 5.23) and the NORO (Figure 5.13) configurations are compared. The impact of the rotation appears to be a higher C_{D_z} by 0.12 over the NORO values, followed by a reduction with the cavity opening. For the 4 inch open case, this reduction in C_{D_z} is approximately 0.15 from the NORO values, and 0.35 for the 8 inch open case. This C_{D_z} variation with the cavity opening is only seen in the 45RO configuration, as the NORO configuration shows no change with the cavity opening.

Figure 5.24 is a plot of the rolling moment coefficient versus local tunnel speed for the 45RO cavities. As was shown for the NORO case, the moment data plotted in Figure 5.24 matches the trends shown in the corresponding Y-force data plotted in Figure 5.22. Mean C_{M_x} values are approximately zero except for some variations in the closed cavity case were values extended up to 0.15. These higher values are most likely due to disturbances created in the small gap around the model, for as the cavity is opened, the mean values return to the zero. Some of this

100
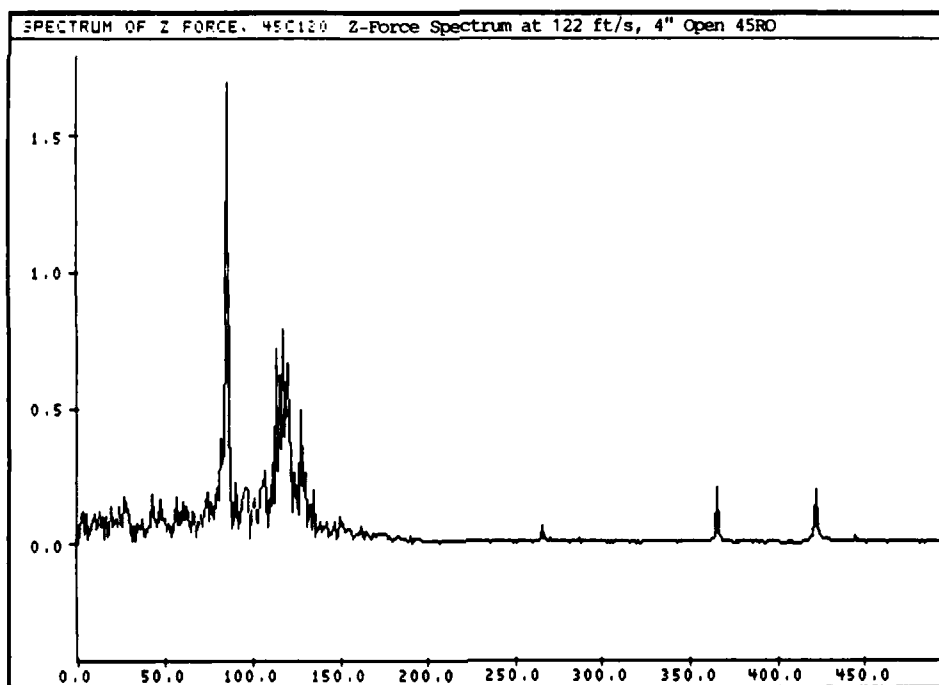
Figure 5.27 Z Force Spectrum at 122 ft/s, 4" Open, 45RO
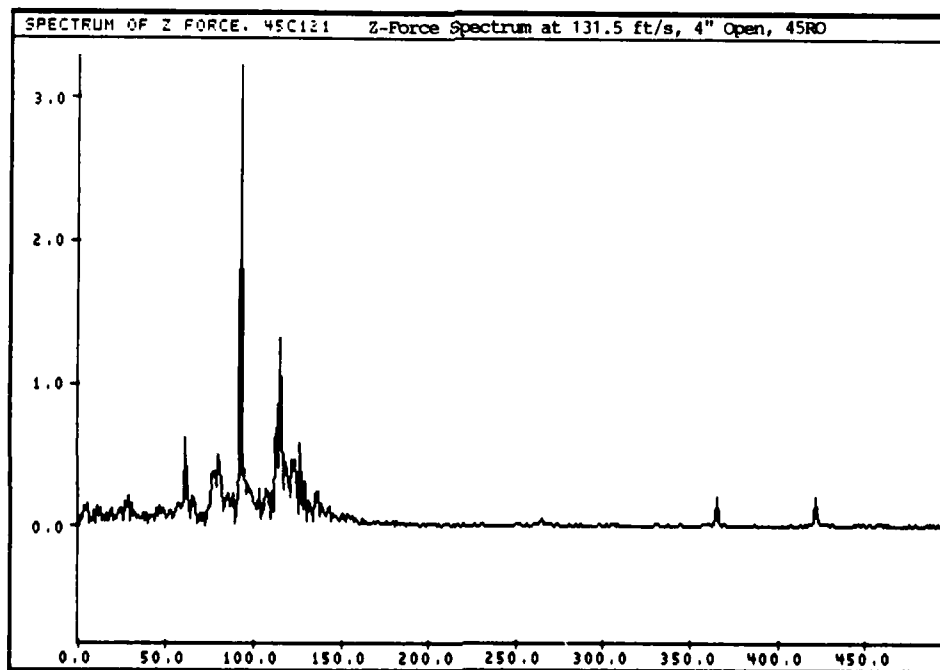
Figure 5.28 Z Force Spectrum at 131.5 ft/s, 4" Open, 45RO
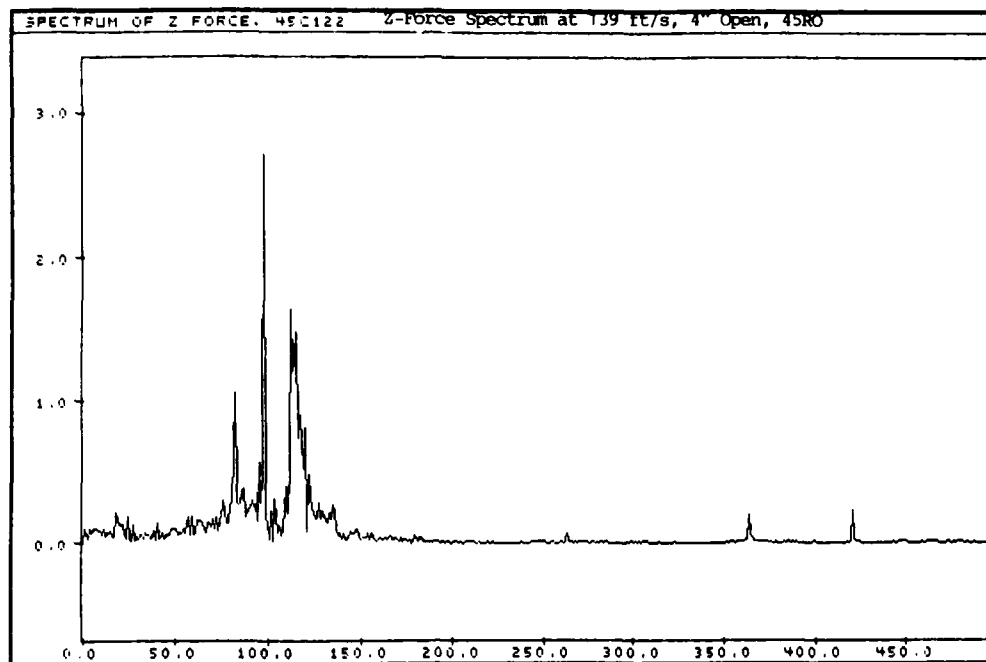
Figure 5.29 Z Force Spectrum at 139 ft/s, 4" Open, 45RO
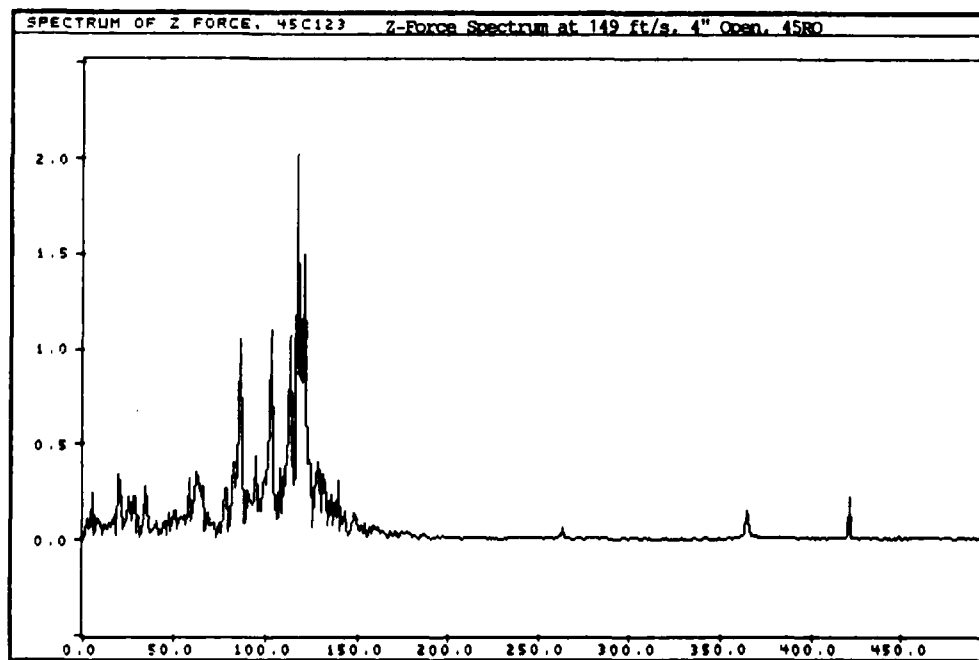
Figure 5.30 Z Force Spectrum at 149 ft/s, 4" Open, 45RO

deviation from zero is also due to LCU accuracies near zero, mentioned earlier. The standard deviation values are representative to the model vibrating at 21 Hz and not of aerodynamic loadings. It appears from this data that cavity opening has no significant impact on the C_{M_x}.

The pitching moment coefficients for the 45RO cavities are shown in Figure 5.25. As with the previous plots of C_{M_x} and C_{D_y}, both mean and standard deviation values of C_{M_y} match the respective data trends in their C_{D_x} counterparts shown in Figure 5.21. Mean values of C_{M_y} appear to hold a constant value of 1.25 over the speed range tested, for all three cavity configurations. Thus, these results lead to the conclusion that the cavity opening does not have a significant effect on the mean C_{M_y} values. However, model rotation does cause a reduction in the mean C_{M_y} val... ʹ⸴ compared to the NORO case. In terms of the actual moments, this is an increase.

The last figure for the 45RO configuration is the yawing moment coefficient shown in Figure 5.26. As was the case in the NORO configurations, all mean C_{M_z} values are zero. The standard deviation values tend to show a constant value of 0.08, independent of the cavity opening. Variations in these standard deviation values are again dominated over the speed range by the model second mode frequency of 87 Hz, as discussed in the NORO case. Thus, the conclusions from this data is the cavity opening and the model rotation has no significant impact on the C_{M_z} values.

The last area of discussion is the side load vibratory inputs to the model. As mentioned in the beginning of this chapter, surveys of the data frequency spectrums showed a predominant 21 Hz natural frequency mode in all processed data in the X and Y axes The only exception to this was the closed cavity NORO configuration where a predominant side force frequency component increased in frequency with speed. This frequency component was seen at 12 Hz for a local tunnel speed of 68.5 ft/s, and progressed up to 20-21 Hz at 118.6 ft/s. Spectrum plots of this shifting frequency component can be seen in Figures 5.31 through 5.33. These three figures represent the intermediate and high speeds tested for the closed cavity NORO configuration, Plots of low and middle speed were previously presented in Figures 5.2 and 5.5.

Table 5.1 summarizes the average shedding frequencies discerned from the spectrum plots. Despite their closeness to the natural frequency of the model's first mode at about 21 Hz, there appears to be a trend of shedding frequencies up to an apparent "lock-on" at approximately 21 Hz. These results show a constant Strouhal number for the side load induced vortex shedding of S = 0.11 from 68.5 ft/s to 118.6 ft/sec. This constant Strouhal number matches reported values for other square bluff bodies (7:15; 10:29-30); thus, supporting the conclusion that the vibratory forces are truly due to aerodynamic loading and not model natural frequency vibrations. At speeds above 98 ft/s, an apparent excitation and "lock-on" to the 21 Hz natural frequency takes place. This is seen in the 21 Hz frequency spike amplitude gain along with the positive frequency shift of the shedding frequency component as tunnel
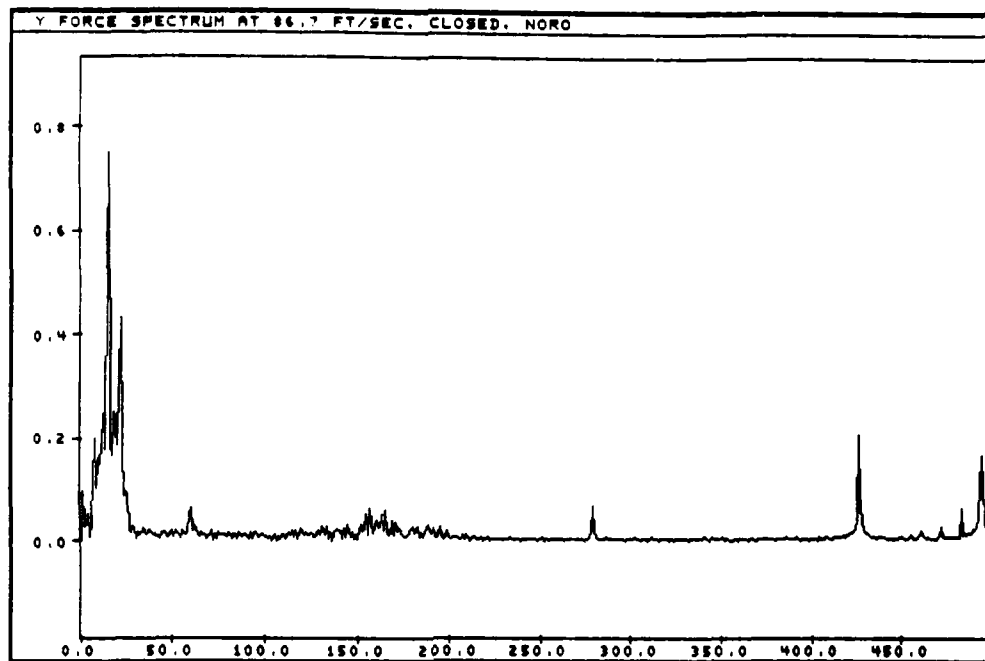
Figure 5.31   Y Force Spectrum at 86.7 ft/s, Closed, NORO
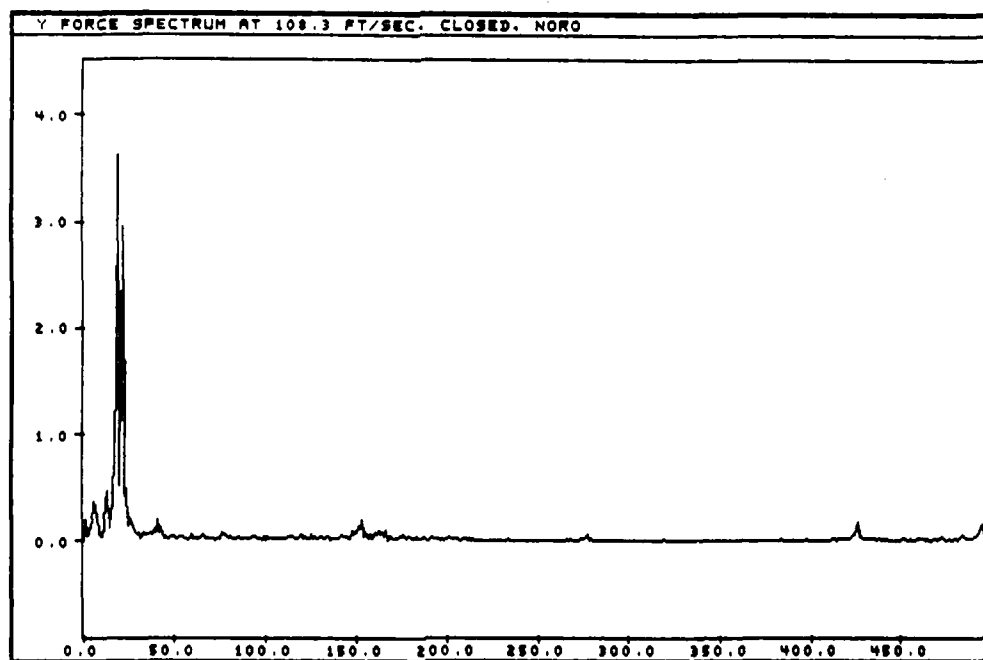
Figure 5.32   Y Force Spectrum at 108.3 ft/s, Closed, NORO

105
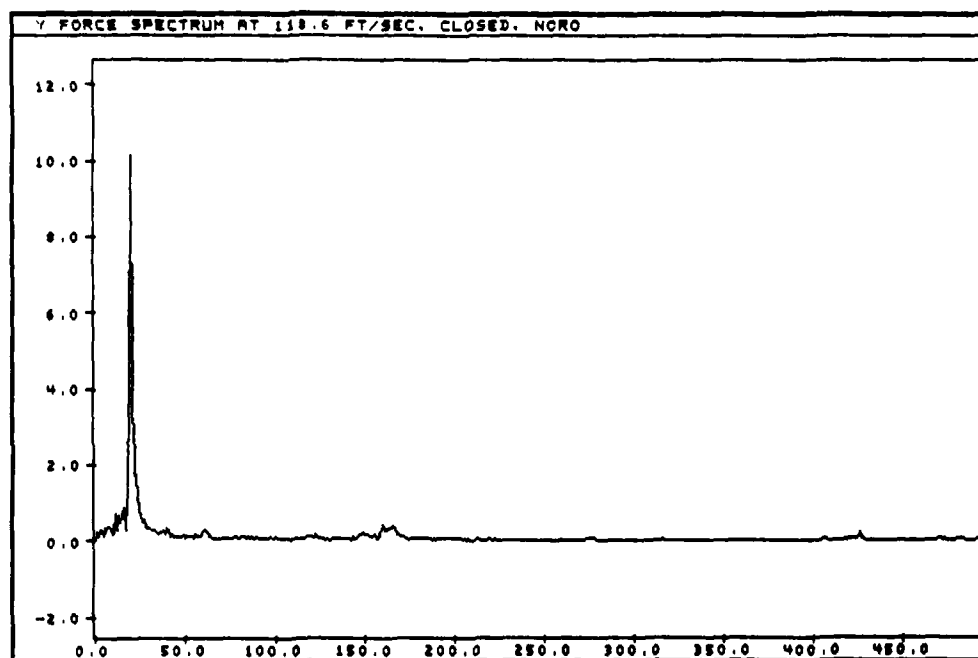
Figure 5.33   Y Force Spectrum at 118.6 ft/s, Closed, NORO

Table 5.1   Average Shedding Frequencies and Strouhal Numbers for No-Rotation, Closed Configuration

Local Tunnel Velocity V (ft/s)	Average Shedding Frequency f_{F_y} (Hz)	Strouhal Number
68.9	11.5	0.112
86.7	15.0	0.115
97.2	17.0	0.117
108.3	19.0	0.117
118.6	20.0	0.112

$$\text{Strouhal \#} = \frac{f_{F_y} W}{V}$$

$$W = 8 \text{ inch} = 0.667 \text{ ft}$$

speed increases. The excitation and "lock-on" can be seen starting with Figure 5.5 followed by Figures 5.32 and 5.33. The apparent shedding frequency component shifts in frequency and magnitude from 18 Hz at 1.72 (Figure 5.5) to 19 Hz at 3.62 (Figure 5.32). In Figure 5.33 the frequency is up to 20 Hz at a magnitude of 10.13. This rapid rise in frequency amplitude indicates the excitation of the first mode frequency, leading to the domination of the frequency spectrum by this first mode. Thus, further discernment of actual wind induced vibrations is masked by this natural frequency vibration.

VI Conclusions and Recommendations

As stated at the beginning of this study, the objective and scope was to characterize the vibration input to a bluff body extending from a cavity. Ideally, the model used for this type of analysis should have a high natural frequency. According to Savkar and So, the model natural frequency should be at least four times that of the dominant force frequency to allow the measurement system to work with reasonable accuracy (9:403). From the pre-test modal analysis, this was found not to be the case. Frequency spectrum analysis of the transient force and moment data files showed the presence of the first and second model natural frequencies. The first mode frequency at around 21 Hz was predominant in the X and Y force and moment data while the 87 Hz second mode dominated the Z-moment data. The only exception to this was in the closed cavity NORO configuration where it appears side load forces are induced by vortex shedding from the vertical back corners of the model. In this case, the side load vibrations from the vortex shedding produced a constant Strouhal number of 0.11 over the speed range of 68 ft/s to 120 ft/s. In all of other cases tested, the natural frequencies of the model dominated the frequency spectrum masking any of the actual air loading vibration, as discussed in Chapter IV. Despite these limitations on the vibratory inputs, several conclusions can be made about the cavity and model rotation effects.

1. Mean drag forces increase with both cavity opening and model rotation.

109

2. Side forces show no significant changes due to cavity opening or model rotation.

3. Lift forces were constant with cavity opening in the NORO case, but showed a decrease with cavity opening in the 45RO case. (These findings may be particular to the model due to air interactions under the model.)

4. Rolling moments were constant about zero for all configurations.

5. Pitching moments remained constant with cavity opening and increased with model rotation.

6. Yawing moments were constant about zero for all configurations.

In order to obtain a clearer picture of the cavity effects on the induced forces to the bluff body, additional testing is in order. Recommendations for future testing include:

1. Redesigning the LCU to improve hysteresis effects. This would entail reducing the number of load cell elements and attempting to measure only a few of the six force and moment parameters at one time. A redesign should also look into the stiffness of the unit to help improve the model/LCU natural frequencies.

2. Reducing the model weight to help increase its natural frequency. A styrofoam core with a hard epoxy was a consideration for a second phase of this program, and may help improve frequency response.

3. Sealing the base of the model to prevent possible interaction with the Z-axis lift force.

4. Measuring pressure and turbulence in the cavity.

5. Varying the pattern of the cavity opening to observe the variation in possible dampening effects. A circular opening or 3-D cavity shapes could be investigated.

6. Surveying the flow field with a hot wire probe, both upstream and in the wake of the model.

7. Varying the model rotation relative to the wind at smaller increments between 0 and 45 degrees.

8. Investigating the effects of turbulence generation in front of the model.

REFERENCES

1. Vickery, B. J. "Fluctuating Lift and Drag on a Long Cylinder of Square Cross Section in a Smooth and in a Turbulent Stream", Journal of Fluid Mechanics, 25: 481-494 (1966).

2. Sakamoto, Hiroshi, and Masaru Moriya, and Mikio Arie. "A Study on the Flow Around Bluff Bodies Immersed in Turbulent Boundary Layers (Part 1, On the Form Drag of a Normal Plate)", Bulletin of the Japan Society of Mechanical Engineers, 18: No. 124, 1126-1133 (October 1975).

3. Sakamoto, Hiroshi, and Masaru Moriya, and Mikio Arie. "A Study on the Flow Around Bluff Bodies Immersed in Turbulent Boundary Layers (Part 2, The Pressure Forces Acting on Inclined Plates)", Bulletin of the Japan Society of Mechanical Engineers, 20: No. 139, 71-78 (January 1977).

4. Sakamoto, H., and M. Arie. "Flow Around a Normal Plate of Finite Width Immersed in a Turbulent Boundary Layer", Journal of Fluids Engineering, 105: 98-104 (March 1983).

5. Castro, I. P., and A. G. Robins. "The Flow Around a Surface-Mounted Cube in Uniform and Turbulent Streams", J. Fluid Mech, 79: 307-335 (1977).

6. Sakamoto, Hiroshi, and Mikio Arie. "Flow Around a Cubic Body Immersed in a Turbulent Boundary Layer", Journal of Wind Engineering and Industrial Aerodynamics, 9: 275-293 (1982).

7. Merritt, Paul. Scaling of Aerodynamic Data from Academy Tests Revision A. AF Weapons Laboratory, NM, 16 February 1989.

8. Harris, Cyril M. Shock and Vibration Handbook. 3rd. ed. New York: McGraw-Hill Book Company, 1988.

9. So, R. M. C., and S. D. Savkar. "Buffeting Forces on Rigid Circular Cylinders in Cross Fluids", Journal of Fluid Mechanics, 105: 397-425 (1981).

10. Miller, R. W. Flow Measurement Engineering Handbook. New York: McGraw-Hill Book Company, 1983.

11. Hoerner, Sighard F. Fluid-Dynamic Drag. 2nd. ed. Great Britan: Sighard F. Hoerner, 1958.

12. Zucrow, Maurice J., and Joe D. Hoffman. Gas Dynamics. Vol. 1. New York: John Wiley and Sons, Inc. 1976.

13. Yardich, Nicholas. Public Affairs Write-up on AFIT Five Foot Wind Tunnel for Base Newspaper. Department of Aeronautics and Astronautics, School of Engineering Air Force Institute of Technology (AU), Wright-Patterson AFB OH, 28 August 1984.

14. ACUREX Corporation. 7000--MDAS Modular Data Acquisition Systems Reference Manual. Manual P/N: 60509-010 Version 4.5. ACUREX Corporation, June 1980.

15. 1989 Ashrae Handbook Fundamentals. I-P ed., 14.1-14.17. Society of Heating, Refrigeration and Air Conditioning Engineers Inc., Atlanta, 1989.

16. Interface, Inc. Calibration Certificate Installation Information. Interface, Inc., Scottsdale AZ, 1984.

APPENDIX A

THE LOAD CELL UNIT

(LCU)

A.1 Load Cell Unit Theory

Due to the redundant nature of the LCU, voltage outputs from the eight load cells require combination into six load response voltages, each corresponding to one of the six loading components. These combined voltages are designated EC_1, EC_2, EC_3, EC_4, EC_5, and EC_6, corresponding respectively to loading F_x, F_y, F_z, M_x, M_y, and M_z. The make-up of these combined voltages is defined in Table A.1, which includes output sign responses to positive loadings. Table A.2 provides the load cell responses to ideal loadings.

These six load response voltages are defined to represent the six loading components. However, due to the interactive nature of the LCU, each load response voltage is actually a function of its primary loading along with the remaining five secondary loadings.

$$\Delta EC = \Delta EC_{Primary\ Loading} + \Delta EC_{Secondary\ Loadings} \qquad (A.1)$$

The magnitude of the primary and secondary loadings on each EC term can be represented by a coefficient matrix. This coefficient matrix represents the EC combinations of the eight load cell voltage outputs versus the six load components. The individual calibration slopes for each load cell versus a loading are combined according to the EC definition in Table A.1. For example, the change in EC_1 due to F_x is represented by:

$$\frac{\partial EC_1}{\partial F_x} = \left(\frac{\partial EC_1}{\partial E_0}\right)\left(\frac{\partial E_0}{\partial F_x}\right) + \left(\frac{\partial EC_1}{\partial E_2}\right)\left(\frac{\partial E_2}{\partial F_x}\right) \qquad (A.2)$$

Here, the first terms of each product on the right hand side represents

115

Table A.1 Load Cell Output Voltage Definitions

VOLTAGE COMBINATION	LOAD CELL RESPONSES

$EC_1 = E_2 - E_0 \longrightarrow F_x$ Positive X Force

$\quad$ (EC_1 is positive for F_x) $E_0 = -$

$\qquad\qquad\qquad\qquad\qquad$ $E_2 = +$

$EC2 = (E_1 - E_3) \longrightarrow F_y$ Positive Y Force

$\quad$ (EC_2 is positive for F_y) $E_1 = +$

$\qquad\qquad\qquad\qquad\qquad$ $E_3 = -$

$EC_3 = -(E_4 + E_5 + E_6 + E_7) \longrightarrow F_z$ Positive Z Force

$\quad$ (EC_3 is positive for F_z) $E_4 = - \quad E_6 = -$

$\qquad\qquad\qquad\qquad\qquad$ $E_5 = - \quad E_7 = -$

$EC_4 = E_4 + E_5 - (E_6 + E_7) \longrightarrow M$ Positive X Moment

$\quad M_x$ Break-down: $E_4 = + \quad E_6 = -$

$$M_{x_{45}} = 2.250'' * (E_4 + E_5) = \tfrac{1}{2} M_x \left.\right\}$$ $E_5 = + \quad E_7 = -$

$$M_{x_{67}} = 2.250'' * (E_6 + E_7) = \tfrac{1}{2} M_x \left.\right\} M_{x_{total}}$$

$EC_5 = E_4 + E_7 - (E_5 + E_6) \longrightarrow M_y$ Positive Y Moment

$\quad M_y$ Break-down: $E_4 = + \quad E_6 = -$

$\qquad\qquad\qquad\qquad\qquad$ $E_5 = - \quad E_7 = +$

$$M_{y_{47}} = 2.488'' * (E_4 + E_7) = \tfrac{1}{2} M_y \left.\right\}$$

$$M_{x_{56}} = 2.488'' * (E_5 + E_6) = \tfrac{1}{2} M_y \left.\right\} M_{y_{total}}$$

$$EC_6 = -(E_0 + E_1 + E_2 + E_3) \longrightarrow M_z \qquad \text{Positive Z Moment}$$

M_z Break Down:

$$E_0 = - \qquad E_2 = -$$

$$\left.\begin{array}{l} M_{z_0} = 1.625" * E_o = \frac{1}{4}M_z \\[6pt] M_{z_1} = 1.625" * E_1 = \frac{1}{4}M_z \\[6pt] M_{z_2} = 1.625" * E_2 = \frac{1}{4}M_z \\[6pt] M_{z_3} = 1.625" * E_3 = \frac{1}{4}M_z \end{array}\right\} M_{z_{total}}$$

$$E_1 = - \qquad E_3 = -$$

117

Table A.2 Load Cell Responses to Ideal Loadings

Loading \ Load Cell	0	1	2	3	4	5	6	7
Fx	C/T	S	C/T	S	S	S	S	S
Fy	S	C/T	S	C/T	S	S	S	S
Fz	S	S	S	S	C/T	C/T	C/T	C/T
Mx	S	S	S	S	C/T	C/T	C/T	C/T
My	S	S	S	S	C/T	C/T	C/T	C/T
Mz	C/T	C/T	C/T	C/T	S	S	S	S

Key : S = Shear

C/T = Compression Tension

Notes:

1. Load Cells have approximately 200:1 Side Load Rejection

2. Force and Moment Center located at center of X-Y Plane

the sign of the product while the second term is the actual load cell output change due to the loading, F_x.

Multiplication of the coefficient matrix by the loading components results in a set of equations representing the combined voltages (EC). Table A.3 shows this set of equations in matrix form. A Gauss elimination routine was used to solve these equations for the force and moment loadings. To account for possible coefficient slope change across the zero point, a second set of coefficients for negative loadings were determined from calibrations. Thus, a total of 72 coefficients are available to make up a coefficient matrix of 36 values.

The computer code for processing the LCU outputs assumes all positive coefficients for the first calculation of the loadings. Based on these results, the coefficient matrix is re-loaded with the proper coefficients, and the final loading values are determined. Since the slope changes between positive and negative loadings are small, this two pass iteration is sufficient to select the correct coefficients.

A zero point is taken at the start of each run to compensate for the effects caused by bias shifts in the LCU output voltages. These zero point voltages are subtracted from the run time data in order to "zero-out" the data for post-processing through the conversion routine.

Table A.3 - Matrix Equations for LCU Force and Moment Resolution

$$
\begin{bmatrix}
\dfrac{\partial EC_1}{\partial F_x} & \dfrac{\partial EC_2}{\partial F_x} & \dfrac{\partial EC_3}{\partial F_x} & \dfrac{\partial EC_4}{\partial F_x} & \dfrac{\partial EC_5}{\partial F_x} & \dfrac{\partial EC_6}{\partial F_x} \\[2ex]
\dfrac{\partial EC_1}{\partial F_y} & \dfrac{\partial EC_2}{\partial F_y} & \dfrac{\partial EC_3}{\partial F_y} & \dfrac{\partial EC_4}{\partial F_y} & \dfrac{\partial EC_5}{\partial F_y} & \dfrac{\partial EC_6}{\partial F_y} \\[2ex]
\dfrac{\partial EC_1}{\partial F_z} & \dfrac{\partial EC_2}{\partial F_z} & \dfrac{\partial EC_3}{\partial F_z} & \dfrac{\partial EC_4}{\partial F_z} & \dfrac{\partial EC_5}{\partial F_z} & \dfrac{\partial EC_6}{\partial F_z} \\[2ex]
\dfrac{\partial EC_1}{\partial M_x} & \dfrac{\partial EC_2}{\partial M_x} & \dfrac{\partial EC_3}{\partial M_x} & \dfrac{\partial EC_4}{\partial M_x} & \dfrac{\partial EC_5}{\partial M_x} & \dfrac{\partial EC_6}{\partial M_x} \\[2ex]
\dfrac{\partial EC_1}{\partial M_y} & \dfrac{\partial EC_2}{\partial M_y} & \dfrac{\partial EC_3}{\partial M_y} & \dfrac{\partial EC_4}{\partial M_y} & \dfrac{\partial EC_5}{\partial M_y} & \dfrac{\partial EC_6}{\partial M_y} \\[2ex]
\dfrac{\partial EC_1}{\partial M_z} & \dfrac{\partial EC_2}{\partial M_z} & \dfrac{\partial EC_3}{\partial M_z} & \dfrac{\partial EC_4}{\partial M_z} & \dfrac{\partial EC_5}{\partial M_z} & \dfrac{\partial EC_6}{\partial M_z}
\end{bmatrix}
\begin{Bmatrix} F_x \\ F_y \\ F_z \\ M_x \\ M_y \\ M_z \end{Bmatrix}
=
\begin{Bmatrix} EC_1 \\ EC_2 \\ EC_3 \\ EC_4 \\ EC_5 \\ EC_6 \end{Bmatrix}
$$

Coefficient Matrix   Loadings   Combined Voltages

120

A2. LCU Range Selection

Load ranges for the LCU were based on the largest force expected on the model, primarily the drag force. A drag force of 30.4 lb_f was calculated using

$$F_x = \frac{1}{2}\rho V^2 A C_{D_x} \tag{A.3}$$

where

$$C_{D_x} = 1.5$$

$$\rho = 0.00228 \frac{lb_f s^2}{ft^2}$$

$$V = 200 \ ft/s$$

$$A = 0.444 \ ft^2$$

The above values represent the upper limit of expected operating parameters. The C_{D_x} value of 1.5 was higher than the maximum value observed during USAFA testing of an 8 inch cube (USAFA:10); thus, calculated the drag force margin has a safety limit built in.

With this upper force limit in hand, the next step was to propagate this force through the LCU to the individual load cells and check limits. Assuming a 30 lb_f load was applied in either the X or Y direction, two load cells were available to absorb the loading. Ideally, each load cell would sense this loading equally at 15 lb_f each. In the case of a 30 lb_f load in the Z axis, the load is distributed to four load cells at 7.5 lb_f each. These results show that for pure force application, no limits are reached on the individual load cells.

The next step was to check out the impact of applied moments to the load cells. Again, the worst case was assumed due to the drag force acting on the front face center of the model. The moment arm to the

121

defined LCU centroid (centered on the LCU X-Y plane) is 8.97 inches. Thus, the drag force of 30 lb_f would create a moment of 269 in-lb_f. Dividing this moment by the short moment arms between the base load cells and centroid results in the actual force loadings on the load cells. In the case of a 30 lb_f drag in the X-axis of the LCU, each load cell should see 0.901 times the drag force. For a 30 lb_f in the Y-axis, the loading is 0.996 times. Figures A.1 and A.2 indicate the geometry and equations used to determine the impact of these Y and X moments on the individual load cells. In a similar manner, the induced forces due to a Z-moment were calculated. These results show a 30 lb_f load acting on the edge of the model would produce individual load cell loadings of 18.46 lb_f. Figure A.3 provides the geometry for the Z-moment impact.

These results of the force and moment propagations through the LCU showed that a 25 lb_f load cell was sufficient to handle the applied loadings. The selected 25 lb_f load cells are capable of loads up to 37.5 lb_f without damage (16:1-2) and provides better resolution of forces over a 50 lb_f load cell, the next size up.
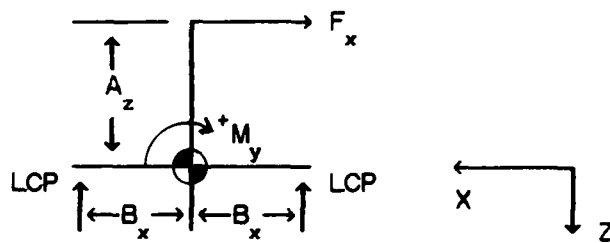
$A_z = 8.97$ inches

$B_x = 2.488$ inches

$M_y = A_z \times F_x$

$M_y = 4 [B_x \times F_{LC}]$

$F_{LC} = \dfrac{M_y}{4B_x} = \dfrac{A_z \times F_x}{4B_x}$

$F_{LC} = \dfrac{(8.97)F_x}{4(2.488)} = 0.901F_x$

LCP = Load Cell Point of Loading

Figure A.1 Y Moment Impact on Load Cells
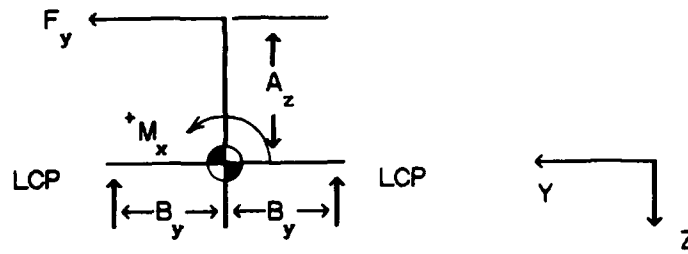
A_z = 8.97 inches

B_y = 2.25 inches

$M_x = A_z \times F_y$

$M_x = 4 [B_y \times F_{LC}]$

$LC = \dfrac{M_x}{4B_y} = \dfrac{A_z \times F_y}{4B_y}$

$F_{LC} = \dfrac{(8.97)F_y}{4(2.25)} = 0.996\ F_y$

LCP = Load Cell Point of Loading

Figure A.2 X Moment Impact on Load Cells
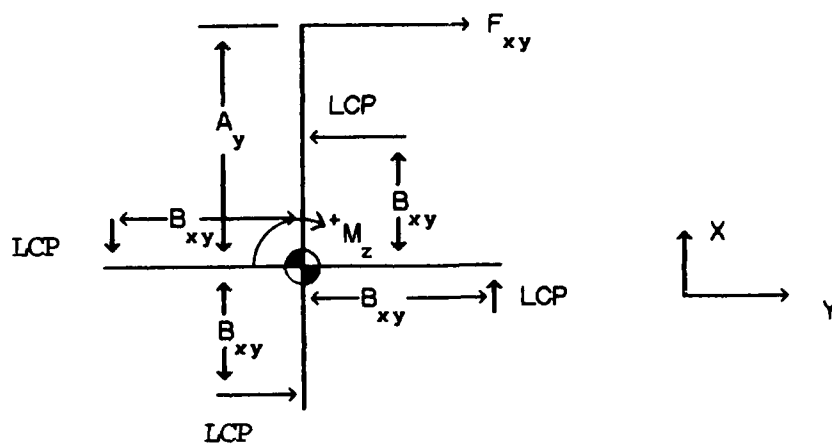
A_{xy} = 4.00 inches

B_{xy} = 1.625 inches

$M_z = A_{xy} \times F_{xy}$

$$F_{LC} = \frac{M_z}{4B_{xy}} = \frac{A_{xy} \times F_{xy}}{4B_{xy}}$$

$$F_{LC} = \frac{(4.00)\ F_{xy}}{4(1.625)} = 0.6158\ F_{xy}$$

LCP = Load Cell Point of Loading

Figure A.3 Z Moment Impact on Load Cells

A.3 LCU Calibration

In order to account for any interactions between the model and the LCU, calibration of the LCU was conducted with the model attached. Loadings for the calibration were based on the limits defined in section A.2. To simulate pure forces and moments on the model, specific load points were defined. For X and Y force applications, a load line was established on the model aligning these forces with their primary load cells in the X-Y plane. These loadings were centered on the particular force being loaded. The Z force was handled by applying weights, centered on top of the model. X, Y, and Z moments were applied to the model with equal and opposite forces to produce pure moments. Figure A.4 shows how X and Y moments were applied to the model while Figure A.5 shows how the Z moment was applied.

All forces and moments, except the Z moment, were applied to the model using a plastic coated steel cable looped around the model. For the Z-moment, small aluminum "L" channels were super glued to the model corners at the load line level. Using these "L" channel extensions, Y-directional forces could be applied to the model as depicted in Figure A.5. These "L" channels were removed after calibrations.

Small "S" hooks were used to connect the steel loop or "L" channel connector to the steel cable pulley and weight system as shown in Figure 3.15. The pulley system was mounted to the cavity floor with magnetic mounts. These magnets held for most loadings, however during the X and Y moment applications, additional weights were added to the magnetic base to hold it in place.

LCU Centroid

$M = (8\ \text{inch}) \times F$
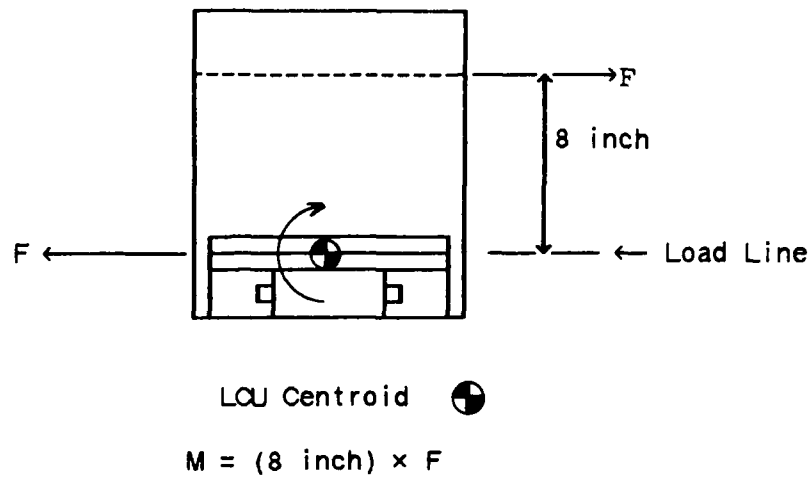
Note: An equal and opposite force is applied at the Load Line to balance forces leading to a moment

Figure A.4   Calibration Moment Applications (M_x and M_y)

$M = [4\ \text{inch} \times F] + [4\ \text{inch} \times F]$
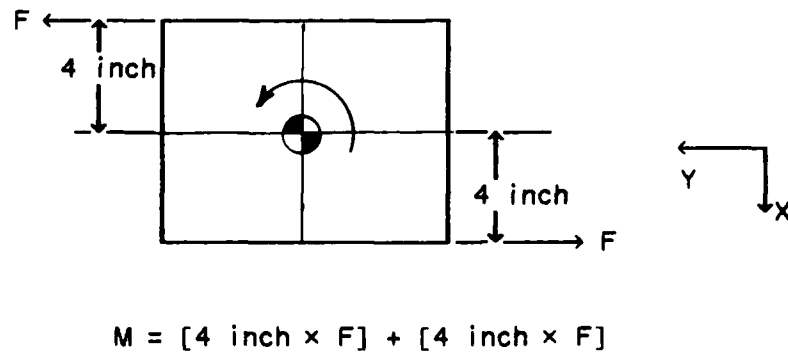
Figure A.5 Calibration Moment Applications (M_z)

127

Calibration loads for the three force directions were divided into 14 loadings up and down, while the applied moments were divided into 12. Before each loading sequence, the model was exercised in the negative X direction (LCU coordinates) to standardize any possible hysteresis effects from the previous calibration. The negative Z force was not calibrated directly due to problems in applying this loading. Thus, the coefficients for negative loadings were assumed the same as the positive loadings.

Results from the calibration loads are plotted in Figures A.6 through A.16. These plots show the combined voltage outputs versus the applied loadings. Hysteresis effects are noticeable in some of these plots. The impact of this hysteresis is discussed in the Check Load Data, Appendix B of this report.

A first order polynomial curve fitting routine in the GRAPHER software package was used to generate the conversion coefficients from this calibration data. A sample of GRAPHER Polynomial Fit Statistics is shown in Figure A.17. These values are for the combined voltage channels EC_1 and EC_2 under a positive X-force loading (LCU coordinates). The complete set of coefficients are provided in Table A.4.
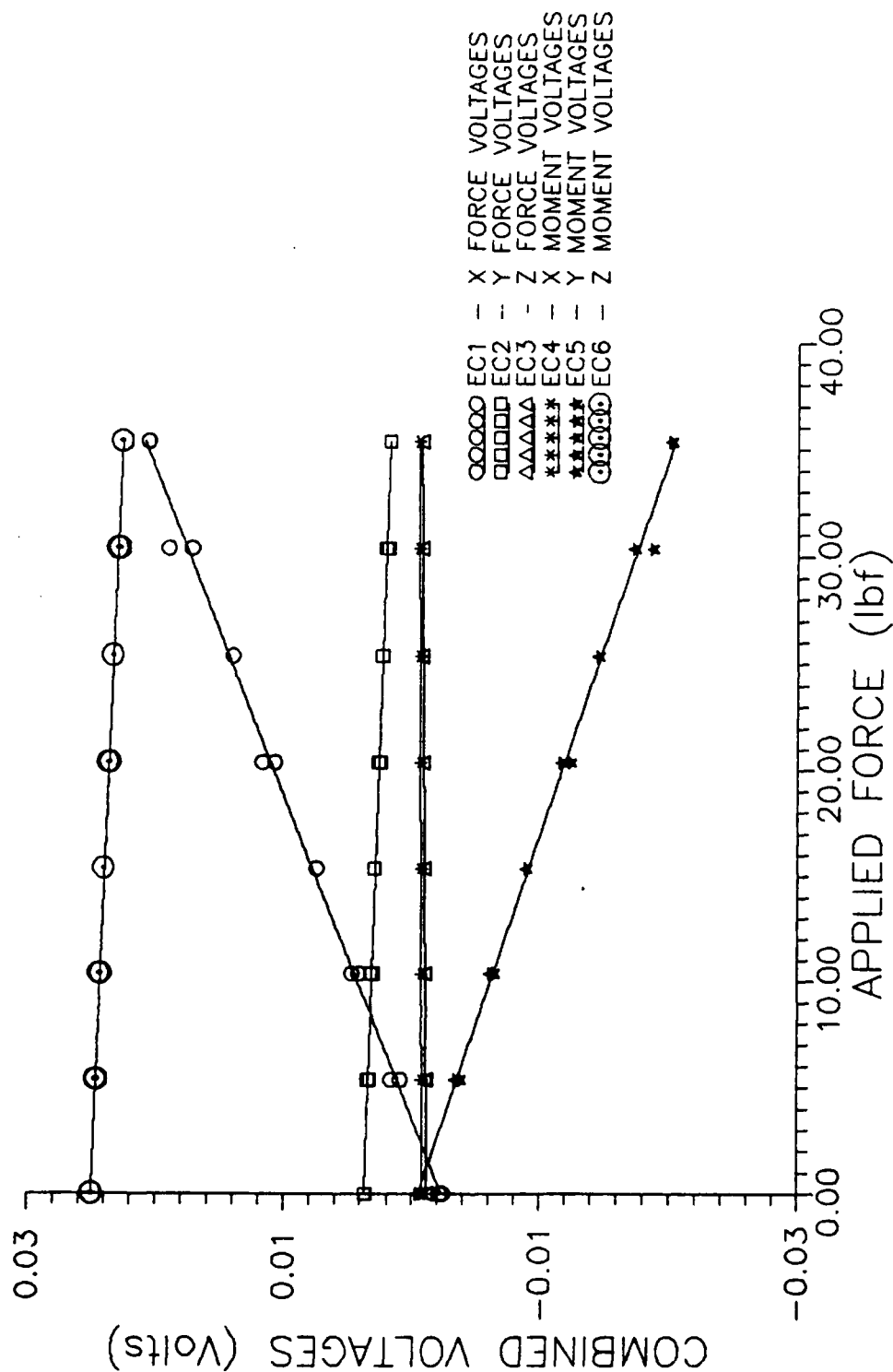
Figure A.6 LCU Calibration Curves for Positive X Force Loading

129

Figure A.7 LCU Calibration Curves for Positive Y Force Loading

Figure A.8 LCU Calibration Curves for Positive Z Force Loading

131

Figure A.9 LCU Calibration Curves for Positive X Moment Loading

Figure A.10 LCU Calibration Curves for Positive Y Moment Loading

Figure A.11 LCU Calibration Curves for Positive Z Force Loading

PRIMARY MOMENT CALIBRATION DATA
NEGATIVE X MOMENT LOADING

OOOOO EC1	—	X	FORCE VOLTAGES
DDDDD EC2	—	Y	FORCE VOLTAGES
△△△△△ EC3	—	Z	FORCE VOLTAGES
***** EC4	—	X	MOMENT VOLTAGES
***** EC5	—	Y	MOMENT VOLTAGES
OOOOO EC6	—	Z	MOMENT VOLTAGES
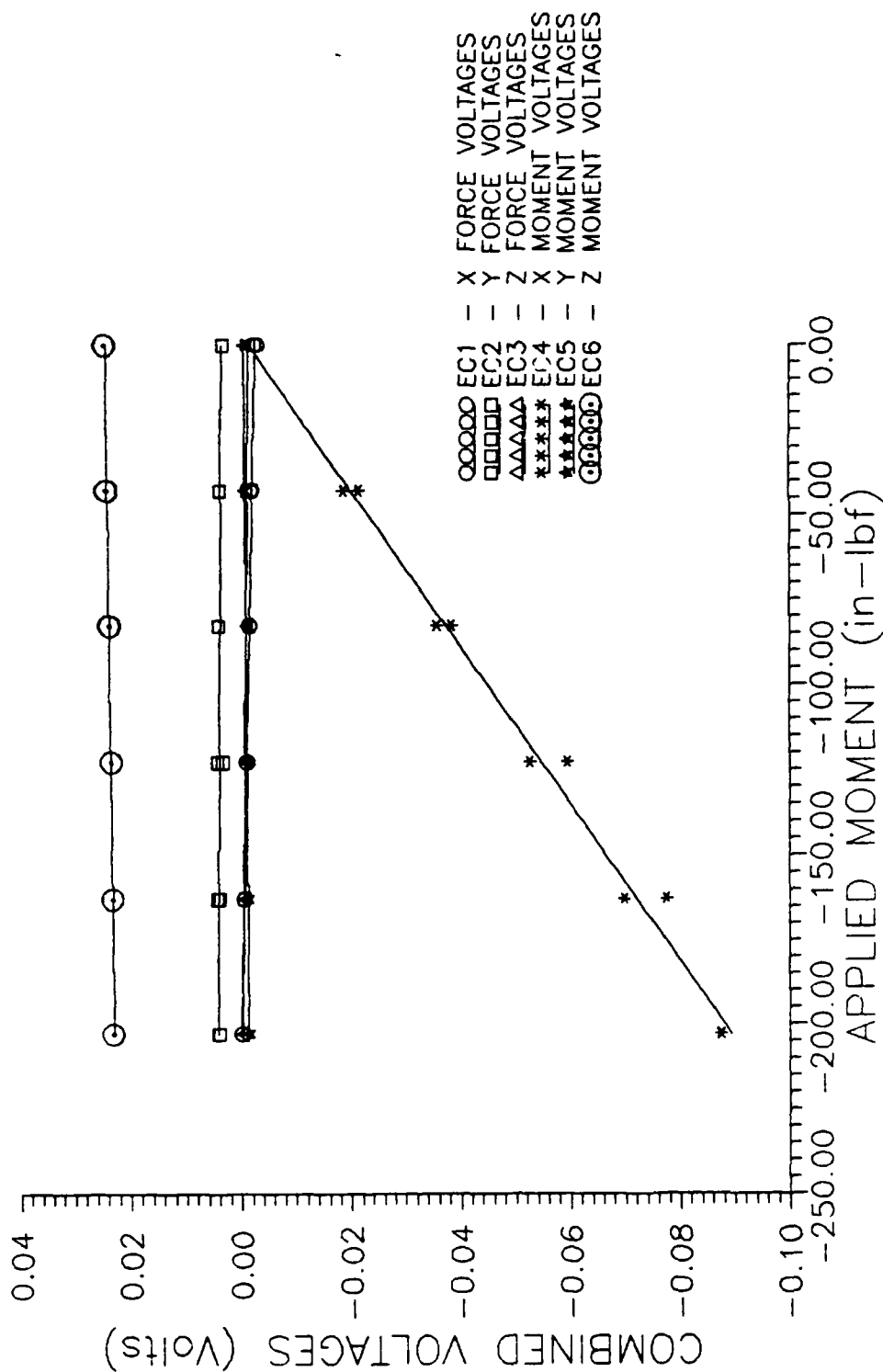
Figure A.12 LCU Calibration Curves for Negative X Force Loading

135

Figure A.13 *LCU Calibration Curves for Negative Y Force Loading*

Figure A.14 LCU Calibration Curves for Negative X Moment Loading

PRIMARY FORCE CALIBRATION DATA
NEGATIVE X FORCE LOADING

EC1 — X FORCE VOLTAGES
EC2 — Y FORCE VOLTAGES
EC3 — Z FORCE VOLTAGES
EC4 — X MOMENT VOLTAGES
EC5 — Y MOMENT VOLTAGES
EC6 — Z MOMENT VOLTAGES

COMBINED VOLTAGES (Volts)

APPLIED FORCE (lbf)
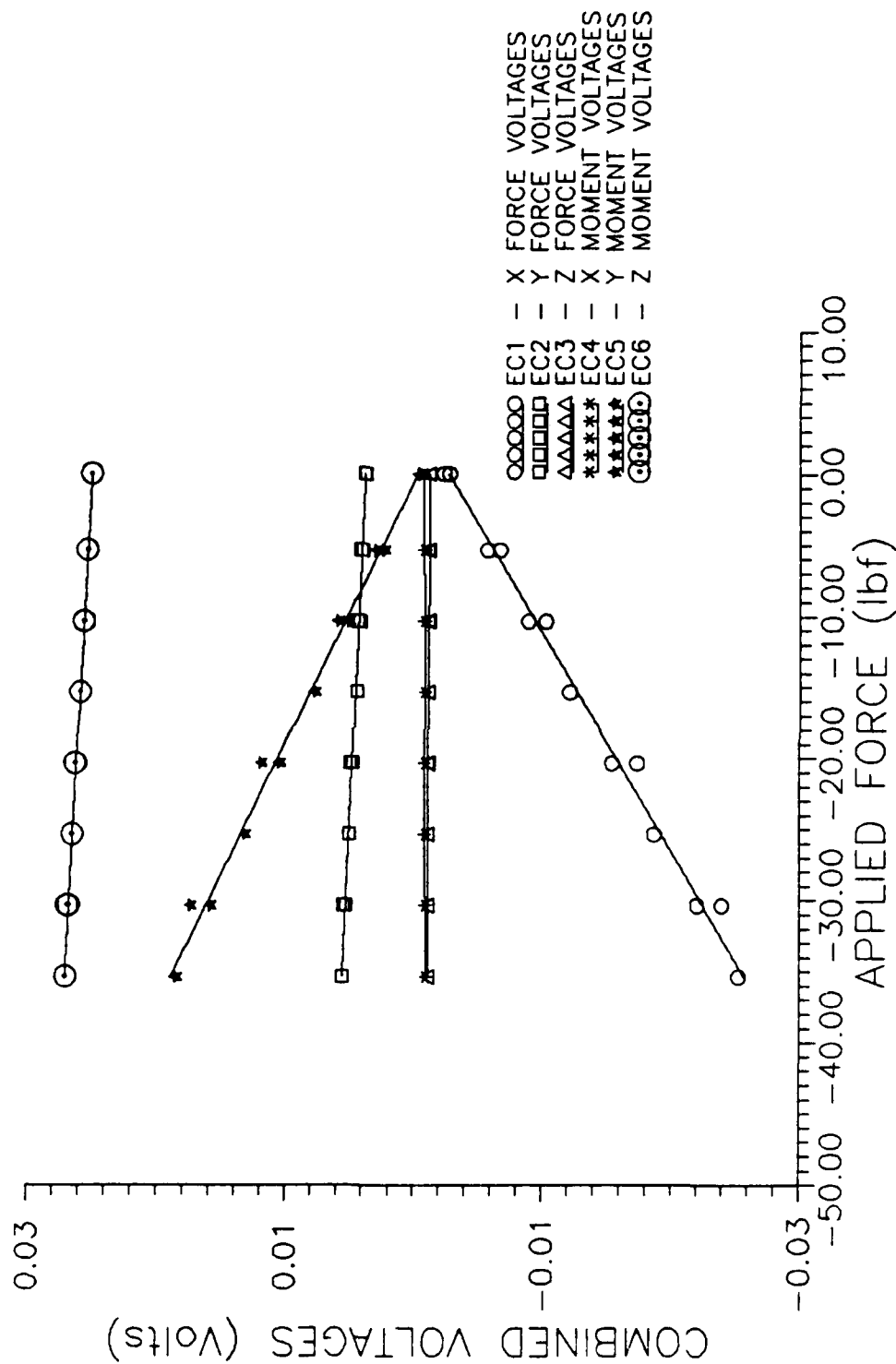
Figure A.15 LCU Calibration Curves for Negative Y Moment Loading

138

PRIMARY FORCE CALIBRATION DATA
NEGATIVE Y FORCE LOADING

EC1 — X FORCE VOLTAGES
EC2 — Y FORCE VOLTAGES
EC3 — Z FORCE VOLTAGES
EC4 — X MOMENT VOLTAGES
EC5 — Y MOMENT VOLTAGES
EC6 — Z MOMENT VOLTAGES
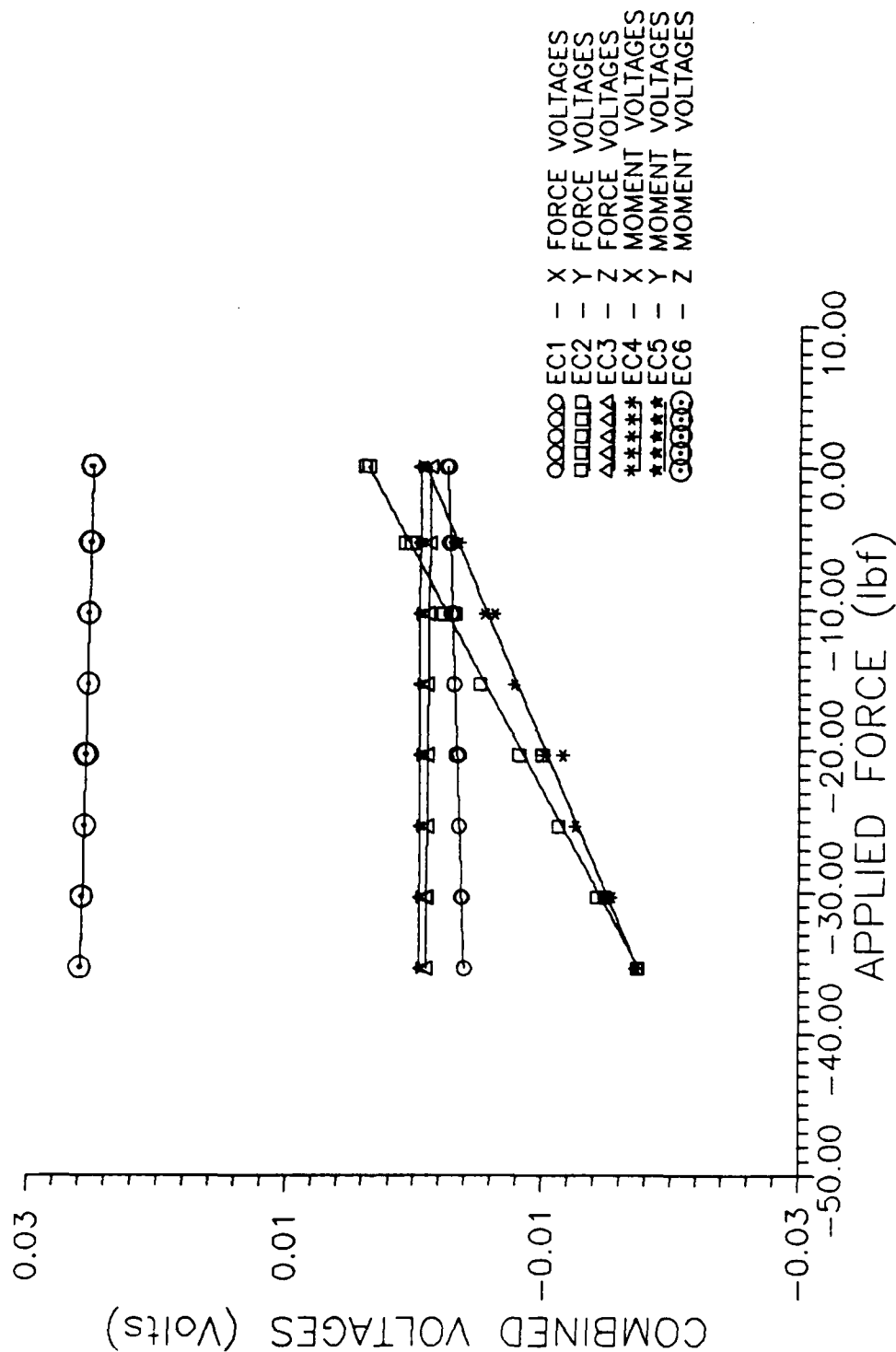
Figure A.16 LCU Calibration Curves for Negative Z Moment Loading

139

```
                    Menu 1.3.6.6 Pol/nomial Fit Statistics
              GRAPHER Copyright (C) 1988 Golden Software, Inc.

Total points = 14          Current data file:  1          Fitting Interval Limits
Points in fit interval = 14       CHAN                          0 to 35.36
                 Sums of Squares      PerCent of Residuals        Polynomial
      Degree      of Residuals        about Mean Explained       Coefficients
        0         0.000884806                 0                   -0.00228799
        1         3.49893E-006               100                   0.00065398  -
```

Change degree of fitting polynomial
       Change Degree   Orthogonal Factors   Fit Statistics

      Esc = Back 1 level   F1 = Summary   F2 = View   F3 = Main Menu
      Use arrow keys to select and —⏎ to execute the selected option

```
                    Menu 1.3.6.6 Polynomial Fit Statistics
              GRAPHER Copyright (C) 1988 Golden Software, Inc.

Total points = 14          Current data file:  2          Fitting Interval Limits
Points in fit interval = 14       CHAN                          0 to 35.36
                 Sums of Squares      PerCent of Residuals        Polynomial
      Degree      of Residuals        about Mean Explained       Coefficients
        0         6.04751E-006                0                    0.00368542
        1         5.08633E-008               99                   -5.39455E-005
```

Change degree of fitting polynomial
       Change Degree   Orthogonal Factors   Fit Statistics

      Esc = Back 1 level   F1 = Summary   F2 = View   F3 = Main Menu
      Use arrow keys to select and —⏎ to execute the selected option

Figure A.17   Sample of GRAPHER Polynomial Fit Statistics
                  (X Force Channel 0 and 1)
```

## Table A.4  LCU Conversion Coefficients

```
ECM      --> MATRIX CONTANTS THE CONVERTION COEFFICIENTS FOR THE
             COMBINED ELECTRICAL VOLTAGES OF THE EIGHT LOAD CELLS
             UNITS [mV/lbf] or [mV/in-lbf]

EC____   --> ECM MATRIX POSITION DEFINITION

             [X___] PRIMARY FORCE OR MOMENT FOR LOAD CELL OUTPUT VOLTAGE
                    1 - X FORCE        4 - X MOMENT
                    2 - Y FORCE        5 - Y MOMENT
                    3 - Z FORCE        6 - Z MOMENT
             [_X__] ACTUAL FORCE APPLIES TO LOAD CELL COMBINATION TO
                    PRODUCE OUTPUT VOLTAGE
                    F - FORCE ; M - MOMENT
             [__X_] AXIS OF THE FORCE OR MOMENT
             [___X] POSITIVE OR NEGATIVE FORCE OR MOMENT APPLICATION
                    P - POSITIVE ; N - NEGATIVE
```

' >>> POSITIVE X FORCE APPLICATION RESULTS   ' >>> NEGATIVE X FORCE APPLICATION RESULTS

```
ECM(1, 1) = 6.5398E-04    (EC1FXP)          ECM(7, 1) = 6.5138E-04    (EC1FXN)
ECM(1, 2) = -5.3946E-05   (EC2FXP)          ECM(7, 2) = -4.9734E-05   (EC2FXN)
ECM(1, 3) = 1.3136E-05    (EC3FXP)          ECM(7, 3) = -1.9874E-06   (EC3FXN)
ECM(1, 4) = 8.2706E-06    (EC4FXP)          ECM(7, 4) = 3.8691E-06    (EC4FXN)
ECM(1, 5) = -5.6261E-04   (EC5FXP)          ECM(7, 5) = -5.4421E-04   (EC5FXN)
ECM(1, 6) = -6.9545E-05   (EC6FXP)          ECM(7, 6) = -5.7858E-05   (EC6FXN)
```

' >>> POSITIVE Y FORCE APPLICATION RESULTS   ' >>> NEGATIVE Y FORCE APPLICATION RESULTS

```
ECM(2, 1) = 3.4865E-05    (EC1FYP)          ECM(8, 1) = 3.7838E-05    (EC1FYN)
ECM(2, 2) = 6.1444E-04    (EC2FYP)          ECM(8, 2) = 5.9822E-04    (EC2FYN)
ECM(2, 3) = -1.6621E-06   (EC3FYP)          ECM(8, 3) = -8.8352E-06   (EC3FYN)
ECM(2, 4) = 4.6015E-04    (EC4FYP)          ECM(8, 4) = 4.6785E-04    (EC4FYN)
ECM(2, 5) = 2.6975E-06    (EC5FYP)          ECM(8, 5) = -1.7052E-06   (EC5FYN)
ECM(2, 6) = 5.501E-05     (EC6FYP)          ECM(8, 6) = -2.5901E-05   (EC6FYN)
```

' >>> POSITIVE Z FORCE APPLICATION RESULTS   ' >>> NEGATIVE Z FORCE APPLICATION RESULTS

```
ECM(3, 1) = 4.7484E-06    (EC1FZP)          ECM(9, 1) = ECM(3, 1)     (EC1FZN)
ECM(3, 2) = 3.6797E-06    (EC2FZP)          ECM(9, 2) = ECM(3, 2)     (EC2FZN)
ECM(3, 3) = .0012498      (EC3FZP)          ECM(9, 3) = ECM(3, 3)     (EC3FZN)
ECM(3, 4) = -3.2596E-05   (EC4FZP)          ECM(9, 4) = ECM(3, 4)     (EC4FZN)
ECM(3, 5) = -1.8033E-06   (EC5FZP)          ECM(9, 5) = ECM(3, 5)     (EC5FZN)
ECM(3, 6) = 2.8669E-05    (EC6FZP)          ECM(9, 6) = ECM(3, 6)     (EC6FZN)
```

Table A.4 LCU Conversion Coefficients (cont.)

' >>> POSITIVE X MOMENT APPLICATION RESULTS

```
ECM(4, 1) = -1.1572E-05    (EC1MXP)
ECM(4, 2) = -5.3071E-06    (EC2MXP)
ECM(4, 3) = -1.8869E-06    (EC3MXP)
ECM(4, 4) = 4.3745E-04     (EC4MXP)
ECM(4, 5) = 2.5418E-06     (EC5MXP)
ECM(4, 6) = -4.7707E-06    (EC6MXP)
```

' >>> NEGATIVE X MOMENT APPLICATION RESULTS

```
ECM(10, 1) = -1.2895E-05   (EC1MXN)
ECM(10, 2) = -3.1565E-06   (EC2MXN)
ECM(10, 3) = -5.4074E-06   (EC3MXN)
ECM(10, 4) = 4.3362E-04    (EC4MXN)
ECM(10, 5) = 4.3346E-06    (EC5MXN)
ECM(10, 6) = 8.011E-06     (EC6MXN)
```

' >>> POSITIVE Y MOMENT APPLICATION RESULTS

```
ECM(5, 1) = 3.441E-07      (EC1MYP)
ECM(5, 2) = -4.4373E-06    (EC2MYP)
ECM(5, 3) = 3.5642E-06     (EC3MYP)
ECM(5, 4) = -1.9648E-06    (EC4MYP)
ECM(5, 5) = 3.6632E-04     (EC5MYP)
ECM(5, 6) = -1.242E-06     (EC6MYP)
```

' >>> NEGATIVE Y MOMENT APPLICATION RESULTS

```
ECM(11, 1) = 2.8776E-06    (EC1MYN)
ECM(11, 2) = -2.6463E-06   (EC2MYN)
ECM(11, 3) = -4.8771E-06   (EC3MYN)
ECM(11, 4) = -1.12E-06     (EC4MYN)
ECM(11, 5) = 3.7318E-04    (EC5MYN)
ECM(11, 6) = -3.1755E-05   (EC6MYN)
```

' >>> POSITIVE Z MOMENT APPLICATION RESULTS

```
ECM(6, 1) = 2.421E-06      (EC1MZP)
ECM(6, 2) = 2.5587E-06     (EC2MZP)
ECM(6, 3) = 3.041E-06      (EC3MZP)
ECM(6, 4) = 3.81E-06       (EC4MZP)
ECM(6, 5) = -1.2628E-06    (EC5MZP)
ECM(6, 6) = 5.3428E-04     (EC6MZP)
```

' >>> NEGATIVE Z MOMENT APPLICATION RESULTS

```
ECM(12, 1) = 3.4549E-06    (EC1MZN)
ECM(12, 2) = 3.5412E-06    (EC2MZN)
ECM(12, 3) = -2.381E-06    (EC3MZN)
ECM(12, 4) = 1.396E-06     (EC4MZN)
ECM(12, 5) = 3.1837E-07    (EC5MZN)
ECM(12, 6) = 5.2633E-04    (EC6MZN)
```

APPENDIX B

ERROR ANALYSIS

B.1 Gain Selection

Gain selection was based on the maximum expected loading on the model along with the maximum voltage range of the A/D converter. In addition to these limits, force resolution and gain induced errors were considered in the analysis. Results for earlier check outs of the MDAS "F2" input card showed up to a ± 2.5 bit error at the A/D converter due to switching noises in the filter circuit of this card. Table B.1 is a summary of the gain selections and the resulting error. Using this information, a combined hardware and software gains of 200 was selected.

Table B.1 Gain Selection and Error

Least Significant Bit (LSB) of MDAS A/D Converter

$$LSB = 4.883 \text{ mV}$$

Bit Error for MDAS "F2" Voltage Input Card

$\pm$ 2.5 bits $\implies$ $\pm$ 12.2 mV in A/D converter

Chose Maximum Gain Setting on the Endevco

Gain 50 $\implies$ 60 mV/lb_f

$\pm$ 12.2 mV $\implies$ $\pm$ 0.20 lb_f

Check of Software Gain Effects with Fixed Hardware Gain of 50

Gain 2 $\implies$ 120 mV/lb_f Saturation at 82 lb_f

$\pm$ 12.2 mV $\implies$ $\pm$ 1.62 oz

1 lb_f $\implies$ 10% error

10 lb_f $\implies$ 1% error

Gain 4 $\implies$ 210 mV/lb_f Saturation at 42 lb_f

$\pm$ 12.2 mV $\implies$ $\pm$ 0.82 oz   (0.05 lb_f)

1 lb_f $\implies$ 5% error

10 lb_f $\implies$ 0.5% error

Gain 8 $\implies$ 210 mV/lb_f Saturation at 21 lb_f

$\pm$ 12.2 mV $\implies$ $\pm$ 0.40 oz   (0.05 lb_f)

1 lb_f $\implies$ 2.5% error

10 lb_f $\implies$ 0.25% error

A total gain of 200 was selected to prevent saturation of the A/D converter under maximum loadings while providing the best resolution.

B.2 Excitation Voltage Error

The magnitude of a potential excitation voltage drift of 0.005 volts was checked. This voltage drift was based on the maximum drifts observed in the Endevco amplifier excitation over a several week period. Table B.2 summarizes the results which show the effects to be insignificant.

Table B.2 Excitation Voltage Impact on Resolution

$$\frac{3 \text{ mV}}{V} \times \cdot \text{Excitation Voltage} \Rightarrow \text{Available Voltage for Signal Resolution}$$

For a 10 V excitation voltage, the signal resolution is

$$\frac{30 \text{ mV}}{25 \text{ lb}_f} = 1.20 \text{ mV/lb}_f$$

If an excitation error of 0.01 volts exist

$$\frac{3 \text{ mV}}{V} \times 0.001 \text{ volts} = 0.03 \text{ mV error}$$

The resulting error in signal resolution is

$$\frac{30 \pm 0.015 \text{ mV}}{25 \text{ lb}_f} = (1.20 \pm 0.0006) \text{ mV/lb}_f$$

In terms of a 1 mV source, this resolution error would lead to force measurement error of

$$\frac{1 \text{ mV}}{1.2006 \text{ mV/lb}_f} = 0.83292 \text{ lb}_f$$

or

$$\frac{1 \text{ mV}}{1.1994 \text{ mV/lb}_f} = 0.83375 \text{ lb}_f$$

This error is approximately 0.05 percent, thus a ± 5 mV excitation fluctuation is insignificant.

147

B.3 Check Loads

Check loads of the LCU were conducted at both the beginning and end of the test program to verify the coefficients and the conversion routine. Loads were applied to the model in the same manner as for the calibration. The pre-test results are shown in Tables B.3 through B.12, and post-test results in Tables B.13 and B.14. Actual loading for forces were 5, 10, 15, and 20 lb_f plus 0.36 lb_f for the weight hanging bracket (Z forces were applied without the bracket). Moments applied to the model were 42.88 and 82.88 in-lb_f. The actual errors for each of the loads applied is included in these figures. A summary of the check loads indicates an average percent error of 1-5% for forces and moments in both pre-test and post-test results. These errors appear to increase up to 16% on some readings. However, these higher errors are attributed to the frictions in the load pulley system and not the LCU as the model is unloaded. This conclusion is based on the fact that when the model is completely disconnected from the load cable, values return to within 0.4 lb_f of their original zero point. Thus, the actual errors of the LCU are more in line with the 1-5% range.

TABLE B.3   POSITIVE X FORCE CHECK LOAD APPLICATION - 17 OCT 89

CHK	FX lbf	FY lbf	FZ lbf	MX in-lbf	MY in-lbf	MZ in-lbf	% ERROR PRIMARY LOAD
404	0.00	0.00	0.00	0.00	0.00	0.00	
405	5.14	0.02	0.06	-0.04	-0.37	0.30	-4.1
406	10.10	0.05	0.09	-0.12	-0.53	0.76	-2.5
407	10.17	0.05	0.08	-0.07	-0.51	0.74	-1.8
408	5.85	-0.01	0.04	-0.02	-0.29	0.40	9.1
409	0.10	-0.03	-0.02	0.05	0.08	-0.02	

TABLE B.4   POSITIVE Y FORCE CHECK LOAD APPLIED - 17 OCT 89

CHK	FX lbf	FY lbf	FZ lbf	MX in-lbf	MY in-lbf	MZ in-lbf	% ERROR PRIMARY LOAD
366	0.00	0.00	0.00	0.00	0.00	0.00	
367	0.04	5.12	0.05	0.83	-0.04	-0.84	-4.5
368	0.07	10.00	0.06	1.50	-0.08	-1.72	-3.5
369	0.15	14.91	0.08	2.15	-0.06	-2.70	-2.9
370	0.13	5.91	0.02	0.98	0.06	-1.11	10.26
371	0.11	5.46	0.02	0.92	0.01	-1.08	1.86
372	0.05	0.11	-0.06	0.01	0.04	-0.06	

TABLE B.5   POSITIVE X MOMENT CHECK LOAD APPLICATION - 17 OCT 89

CHK	FX lbf	FY lbf	FZ lbf	MX in-lbf	MY in-lbf	MZ in-lbf	% ERROR PRIMARY LOAD
373	0.00	0.00	0.00	0.00	0.00	0.00	
374	-0.13	-0.03	0.00	40.91	0.16	-0.27	-4.6
375	-0.19	-0.02	-0.05	79.13	0.66	0.03	-4.5
376	-0.18	-0.10	-0.03	79.25	0.68	0.02	-4.4
377	-0.13	-0.18	-0.02	46.23	0.40	-0.14	7.8
378	0.02	-0.09	-0.02	0.02	0.09	0.02	

TABLE B.6   POSITIVE Y MOMENT CHECK LOAD APPLICATION - 17 OCT 89

CHK	FX lbf	FY lbf	FZ lbf	MX in-lbf	MY in-lbf	MZ in-lbf	% ERROR PRIMARY LOAD
399	0.00	0.00	0.00	0.00	0.00	0.00	
400	-0.07	0.22	0.01	0.87	43.92	-0.41	2.4
401	-0.06	0.43	-0.03	1.72	84.70	-0.59	2.2
402	0.23	0.26	0.00	1.00	49.20	-0.43	14.7
403	0.15	-0.02	0.00	0.06	0.22	0.01	

TABLE B.7   POSITIVE Z MOMENT CHECK LOAD APPLICATION - 17 OCT 89

CHK	FX lbf	FY lbf	FZ lbf	MX in-lbf	MY in-lbf	MZ in-lbf	% ERROR PRIMARY LOAD
356	0.00	0.00	0.00	0.00	0.00	0.00	
357	0.15	0.28	0.01	-0.35	0.13	42.45	-1.0
358	0.28	0.51	-0.02	-0.49	0.19	82.17	-0.8
359	0.23	0.46	-0.02	-0.53	0.25	46.96	9.4
360	0.14	0.31	-0.06	-0.40	0.24	0.79	

TABLE B.8   NEGATIVE X FORCE CHECK LOAD APPLICATION - 17 OCT 89

CHK	FX lbf	FY lbf	FZ lbf	MX in-lbf	MY in-lbf	MZ in-lbf	% ERROR PRIMARY LOAD
391	0.00	0.00	0.00	0.00	0.00	0.00	
392	-5.23	-0.03	0.02	0.03	-0.06	-0.25	-2.4
393	-10.16	-0.02	0.02	0.01	-0.29	-0.63	-1.9
394	-15.22	0.00	0.04	0.02	-0.52	-1.17	-0.9
395	-20.26	0.06	0.05	0.07	-0.76	-2.00	-0.5
396	-11.67	0.10	0.05	-0.06	-0.53	-1.22	12.6
397	-6.25	0.06	0.03	-0.03	-0.41	-0.61	16.6
398	-0.26	0.02	0.00	-0.03	-0.28	0.04	

TABLE B.9   NEGATIVE Y FORCE CHECK LOAD APPLICATION - 17 OCT 89

CHK	FX lbf	FY lbf	FZ lbf	MX in-lbf	MY in-lbf	MZ in-lbf	% ERROR PRIMARY LOAD
379	0.00	0.00	0.00	0.00	0.00	0.00	
380	0.04	-5.23	0.03	-0.19	0.01	-0.25	-2.4
381	0.08	-10.21	0.07	-0.27	0.04	-0.45	-1.4
382	0.09	-15.29	0.06	-0.24	0.03	-0.71	-0.4
383	0.06	-11.58	0.07	-0.23	0.09	-0.56	11.7
384	-0.01	-6.08	0.05	-0.29	0.03	-0.30	13.4
385	-0.05	-0.07	0.01	-0.08	-0.07	0.02	

TABLE B.10 NEGATIVE X MOMENT CHECK LOAD APPLICATION - 17 OCT 89

CHK	FX lbf	FY lbf	FZ lbf	MX in-lbf	MY in-lbf	MZ in-lbf	% ERROR PRIMARY LOAD
361	0.00	0.00	0.00	0.00	0.00	0.00	
362	0.17	0.36	0.08	-42.75	-0.56	1.44	-0.3
363	0.22	0.80	0.09	-81.56	-0.96	2.83	-1.6
364	0.18	0.73	0.04	-46.19	-0.50	1.44	7.7
365	-0.03	0.04	-0.08	-0.16	-0.05	-0.09	

TABLE B.11 NEGATIVE Y MOMENT CHECK LOAD APPLICATION - 17 OCT 89

CHK	FX lbf	FY lbf	FZ lbf	MX in-lbf	MY in-lbf	MZ in-lbf	% ERROR PRIMARY LOAD
386	0.00	0.00	0.00	0.00	0.00	0.00	
387	0.00	0.09	-0.01	0.26	-42.59	-2.11	-0.7
388	-0.07	0.18	-0.09	-0.13	-82.62	-5.12	-0.3
389	-0.24	0.10	-0.03	-0.04	-47.90	-3.06	11.7
390	-0.23	0.00	-0.01	0.01	-0.33	-0.03	

TABLE B.12 NEGATIVE Z MOMENT CHECK LOAD APPLICATIONS - 17 OCT 89

CHK	FX lbf	FY lbf	FZ lbf	MX in-lbf	MY in-lbf	MZ in-lbf	% ERROR PRIMARY LOAD
350	0.00	0.00	0.00	0.00	0.00	0.00	
351	-0.11	0.19	-0.31	-0.34	-0.18	-84.20	3.9
352	-0.13	0.27	-0.35	-0.49	-0.22	-44.57	1.6
353	-0.13	0.30	-0.43	-0.46	-0.19	-85.46	3.1
354	-0.16	0.23	-0.42	-0.61	-0.26	-48.90	14.0
355	-0.13	0.26	-0.51	-0.67	-0.21	-1.07	
356	-0.12	0.24	-0.52	-0.70	-0.21	-0.83	

TABLE B.13 POST TEST CHECK LOAD APPLICATION - 26 OCT 89

CHK	FX lbf	FY lbf	FZ lbf	MX in-lbf	MY in-lbf	MZ in-lbf	% ERROR PRIMARY LOAD
416	0.00	0.00	0.00	0.00	0.00	0.00	
417	0.18	10.50	0.11	1.06	0.21	-1.94	1.4
418	0.10	5.53	0.05	0.64	0.17	-1.04	3.2
419	0.00	0.11	-0.02	-0.00	0.01	-0.04	
420	0.04	-10.84	0.04	0.69	0.00	0.38	4.6
421	-0.00	-5.91	0.03	0.49	-0.03	0.19	10.3
422	-0.06	-0.17	-0.04	0.43	-0.08	-0.14	
423	-10.29	0.09	-0.03	0.09	-0.88	-2.44	-0.7
424	-5.40	0.03	-0.01	0.17	-0.54	-1.32	0.7
425	-0.16	-0.01	-0.04	0.21	-0.38	-0.18	
426	-0.13	0.01	10.03	2.01	-0.13	-0.15	-3.2
427	-0.07	0.01	4.99	0.94	-0.28	-0.14	-6.9
428	-0.05	-0.05	-0.04	0.22	-0.27	-0.17	

TABLE B.14 POST TEST CHECKLOAD APPLICATION - 27 OCT 89

CHK	FX lbf	FY lbf	FZ lbf	MX in-lbf	MY in-lbf	MZ in-lbf	% ERROR PRIMARY LOAD
429	0.00	0.00	0.00	0.00	0.00	0.00	
430	-0.02	-10.78	-0.18	0.66	-0.07	-0.59	4.1
431	-0.07	-5.72	-0.23	0.04	-0.11	-0.59	6.7
432	-0.09	0.02	-0.30	-0.39	-0.15	-0.47	
433	-0.08	0.17	4.68	0.09	-0.33	-0.58	-6.4
434	-0.11	0.19	9.69	0.46	-0.18	-0.59	-3.1
435	-0.06	0.19	4.64	0.04	-0.28	-0.61	-7.2
436	-0.05	0.18	-0.41	-0.57	-0.03	-0.61	

APPENDIX C

DATA SUMMARY SHEETS

Table C.1 Mean Data No Rotation of the Model - Closed Configuration

RUN DATE 19 OCT 89

OOC	FX lbf	FY lbf	FZ lbf	MX in-lbf	MY in-lbf	MZ in-lbf	Q lbf/ft^2
117.00	3.24	-0.10	1.75	0.51	29.04	0.08	5.34
118.00	4.59	-0.14	2.56	1.12	41.11	0.25	8.56
119.00	6.35	-0.15	3.41	1.83	56.31	0.42	10.74
120.00	7.85	0.02	4.29	0.94	69.27	0.49	13.33
121.00	9.81	0.02	5.15	1.35	84.49	0.32	15.98
122.00	9.85	-0.06	5.12	2.86	84.62	0.15	15.98
123.00	8.07	-0.01	4.22	1.81	69.53	0.29	13.33
124.00	6.62	-0.04	3.38	1.23	56.72	0.17	10.74
125.00	4.84	-0.02	2.53	0.49	41.93	0.08	8.56
126.00	3.24	-0.14	1.62	0.74	27.69	0.09	5.34

OOC	VEL ft/sec	CDX	CDY	CDZ	CMX	CMY	CMZ
117.00	68.46	1.37	-0.04	0.74	0.03	1.53	0.00
118.00	86.70	1.21	-0.04	0.67	0.04	1.35	0.01
119.00	97.15	1.33	-0.03	0.72	0.05	1.48	0.01
120.00	108.29	1.33	0.00	0.72	0.02	1.46	0.01
121.00	118.61	1.38	0.00	0.73	0.02	1.49	0.01
122.00	118.61	1.39	-0.01	0.72	0.05	1.49	0.00
123.00	108.29	1.36	-0.00	0.71	0.04	1.47	0.01
124.00	97.15	1.39	-0.01	0.71	0.03	1.49	0.00
125.00	86.70	1.27	-0.01	0.67	0.02	1.38	0.00
126.00	68.46	1.36	-0.06	0.68	0.04		

Table C.2 Mean Data No-Rotation of the Model - Open 4"

RUN DATE 19 OCT 89

OOC	FX lbf	FY lbf	FZ lbf	MX in-lbf	MY in-lbf	MZ in-lbf	Q lbf/ft^2
129.00	3.53	0.08	1.72	0.04	27.74	0.28	5.71
130.00	5.22	0.11	2.38	0.28	40.41	0.37	8.20
131.00	6.87	0.24	3.23	0.08	53.60	0.45	11.00
132.00	8.65	0.30	4.00	-0.02	67.42	0.64	13.49
133.00	10.57	0.33	4.84	0.59	82.06	0.55	16.24
134.00	12.43	0.40	5.62	0.33	96.19	0.40	18.94
135.00	12.14	0.48	5.62	0.29	94 .4	0.50	18.94
136.00	13.93	0.42	6.43	0.65	108. 3	0.58	21.64
137.00	14.05	0.60	6.49	-0.13	109.26	0.32	21.64
138.00	15.89	0.58	7.14	0.75	123.09	0.33	24.44
139.00	15.87	0.60	7.19	0.44	123.13	0.39	24.44
140.00	17.62	0.55	8.04	1.01	136.51	0.36	26.83
141.00	17.59	0.71	7.91	0.02	135.91	0.44	26.83
142.00	19.83	0.75	8.79	0.72	152.86	0.20	29.83
143.00	19.59	0.74	8.68	0.31	151.26	0.56	29.83
144.00	21.76	0.82	9.54	0.65	167.41	0.24	32.74
145.00	21.57	0.86	9.33	0.62	165.94	0.27	32.74
146.00	17.87	0.70	7.88	0.67	138.32	0.42	26.83
147.00	10.58	0.53	4.76	0.51	82.85	0.58	16.24
148.00	5.20	0.33	2.31	0.20	41.13	0.47	8.20

OOC	VEL ft/sec	CDX	CDY	CDZ	CMX	CMY	CMZ
129.00	70.84	1.39	0.03	0.68	0.00	1.37	0.01
130.00	84.94	1.43	0.03	0.65	0.01	1.39	0.01
131.00	98.43	1.41	0.05	0.66	0.00	1.37	0.01
132.00	109.06	1.44	0.05	0.67	0.00	1.41	0.01
133.00	119.72	1.47	0.05	0.67	0.01	1.42	0.01
134.00	129.34	1.48	0.05	0.67	0.00	1.43	0.01
135.00	129.34	1.44	0.06	0.67	0.00	1.40	0.01
136.00	138.31	1.45	0.04	0.67	0.01	1.41	0.01
137.00	138.31	1.46	0.06	0.68	0.00	1.42	0.00
138.00	147.07	1.46	0.05	0.66	0.01	1.42	0.00
139.00	147.07	1.46	0.06	0.66	0.01	1.42	0.00
140.00	154.15	1.48	0.05	0.67	0.01	1.43	0.00
141.00	154.15	1.48	0.06	0.66	0.00	1.43	0.00
142.00	162.65	1.50	0.06	0.66	0.01	1.44	0.00
143.00	162.65	1.48	0.06	0.66	0.00	1.43	0.01
144.00	170.48	1.50	0.06	0.66	0.01	1.44	0.00
145.00	170.48	1.48	0.06	0.64	0.01	1.43	0.00
146.00	154.15	1.50	0.06	0.66	0.01	1.45	0.00
147.00	119.72	1.47	0.07	0.66	0.01	1.44	0.01
148.00	84.94	1.43	0.09	0.63	0.01	1.41	0.02

156

Table C.3 Mean Data No-Rotation of the Model – 8" Open

RUN DATE 20 OCT 89

OOC	FX lbf	FY lbf	FZ lbf	MX in-lbf	MY in-lbf	MZ in-lbf	Q lbf/ft^2
151.00	4.09	0.15	1.75	0.01	28.32	0.24	5.66
152.00	6.17	0.28	2.68	-0.02	43.01	0.40	7.94
153.00	7.96	0.42	3.55	0.68	56.00	0.72	10.80
154.00	10.14	0.49	4.34	0.91	70.61	0.39	13.71
155.00	12.20	0.65	5.24	1.04	84.96	0.88	16.35
156.00	12.08	0.76	5.26	0.31	84.44	0.56	16.35
157.00	14.23	0.68	6.08	1.72	99.14	1.45	19.00
158.00	14.17	0.94	6.02	0.51	98.92	0.66	19.00
159.00	16.28	1.02	6.82	0.12	112.98	-0.24	21.70
160.00	18.28	1.19	7.81	-0.19	128.05	0.68	24.45
161.00	17.87	1.13	7.87	1.03	126.80	0.42	24.45
162.00	12.17	0.88	5.33	0.53	85.41	1.14	16.35
163.00	6.14	0.59	2.87	0.84	42.00	0.90	7.94
164.00	5.94	0.61	2.86	0.62	41.40	1.14	7.94

OOC	VEL ft/sec	CDX	CDY	CDZ	CMX	CMY	CMZ
151.00	70.32	1.63	0.06	0.70	0.00	1.41	0.01
152.00	83.34	1.75	0.08	0.76	0.00	1.52	0.01
153.00	97.22	1.66	0.09	0.74	0.02	1.46	0.02
154.00	109.58	1.67	0.08	0.71	0.02	1.45	0.01
155.00	119.76	1.68	0.09	0.72	0.02	1.46	0.02
156.00	119.76	1.66	0.11	0.72	0.01	1.45	0.01
157.00	129.15	1.69	0.08	0.72	0.03	1.47	0.02
158.00	129.15	1.68	0.11	0.71	0.01	1.47	0.01
159.00	138.09	1.69	0.11	0.71	0.00	1.47	0.00
160.00	146.65	1.68	0.11	0.72	0.00	1.47	0.01
161.00	146.65	1.65	0.10	0.73	0.01	1.46	0.00
162.00	119.76	1.68	0.12	0.73	0.01	1.47	0.02
163.00	83.34	1.74	0.17	0.81	0.03	1.49	0.03
164.00	83.34	1.69	0.17	0.81	0.02	1.47	0.04

Table C.4   Standard Deviation Data No-Rotation of the Model – Closed Configuration

RUN DATE 19 OCT 89

00C	FX lbf	FY lbf	FZ lbf	MX in-lbf	MY in-lbf	MZ in-lbf	Q lbf/ft^2
117.00	0.44	0.55	0.38	4.36	3.90	1.07	5.34
118.00	0.75	0.93	0.64	8.37	7.33	1.86	8.56
119.00	0.79	2.04	0.98	20.87	7.12	3.26	10.74
120.00	1.04	3.68	1.13	37.63	9.75	3.36	13.33
121.00	1.26	8.79	1.38	84.78	11.63	4.72	15.98
122.00	1.18	6.13	1.39	60.27	10.84	4.67	15.98
123.00	0.96	2.22	0.94	21.61	9.32	5.03	13.33
124.00	0.75	1.77	1.04	17.06	6.15	2.25	10.74
125.00	0.77	1.06	0.75	9.77	7.45	2.10	8.56
126.00	0.59	0.44	0.39	3.40	5.66	0.92	5.34

00C	VEL ft/sec	CDX	CDY	CDZ	CMX	CMY	CMZ
117.00	68.46	0.19	0.23	0.16	0.23	0.21	0.06
118.00	86.70	0.20	0.24	0.17	0.28	0.24	0.06
119.00	97.15	0.17	0.43	0.21	0.55	0.19	0.09
120.00	108.29	0.17	0.62	0.19	0.79	0.21	0.07
121.00	118.61	0.18	1.24	0.19	1.49	0.20	0.08
122.00	118.61	0.17	0.86	0.20	1.06	0.19	0.08
123.00	108.29	0.16	0.38	0.16	0.46	0.20	0.11
124.00	97.15	0.16	0.37	0.22	0.45	0.16	0.06
125.00	86.70	0.20	0.28	0.20	0.32	0.24	0.07
126.00	68.46	0.25	0.18	0.16	0.18	0.30	0.05

Table C.5 Standard Deviation No-Rotation of the Model - Open 4" Configuration

RUN DATE 19 OCT 89

OOC	FX lbf	FY lbf	FZ lbf	MX in-lbf	MY in-lbf	MZ in-lbf	Q lbf/ft^2
129.00	0.80	0.59	0.49	5.95	7.65	2.69	5.71
130.00	0.89	0.74	0.75	6.96	8.17	3.49	8.20
131.00	0.85	1.11	1.04	10.67	7.22	6.02	11.00
132.00	0.97	0.94	1.25	7.86	6.18	12.79	13.49
133.00	1.43	1.80	1.61	18.22	12.90	9.77	16.24
134.00	1.36	1.66	2.97	15.23	8.95	13.28	18.94
135.00	1.44	1.56	2.80	13.89	9.34	11.63	18.94
136.00	1.73	1.55	4.84	13.79	9.59	10.10	21.64
137.00	1.77	2.06	4.99	18.97	10.75	13.97	21.64
138.00	2.27	2.04	2.96	18.48	10.32	13.32	24.44
139.00	2.11	1.53	2.63	11.61	12 36	11.58	24.44
140.00	2.38	2.20	3.13	18.86	.88	16.23	26.83
141.00	2.50	2.01	2.92	18.27	13.24	9.66	26.83
142.00	2.95	2.37	3.88	19.77	11.18	12.86	29.83
143.00	2.51	2.10	3.76	16.61	8.28	10.42	29.83
144.00	2.78	2.50	4.00	19.38	14.29	9.83	32.74
145.00	3.02	2.39	3.05	17.22	9.79	12.91	32.74
146.00	2.09	1.58	3.08	11.25	11.46	7.80	26.83
147.00	1.58	2.10	1.70	21.62	11.67	6.73	16.24
148.00	0.81	0.65	0.95	5.83	7.54	3.46	8.20

OOC	VEL ft/sec	CDX	CDY	CDZ	CMX	CMY	CMZ
129.00	70.84	0.32	0.23	0.19	0.29	0.38	0.13
130.00	84.94	0.25	0.20	0.21	0.24	0.28	0.12
131.00	98.43	0.17	0.23	0.21	0.27	0.18	0.15
132.00	109.06	0.16	0.16	0.21	0.16	0.13	0.27
133.00	119.72	0.20	0.25	0.22	0.32	0.22	0.17
134.00	129.34	0.16	0.20	0.35	0.23	0.13	0.20
135.00	129.34	0.17	0.19	0.33	0.21	0.14	0.17
136.00	138.31	0.18	0.16	0.50	0.18	0.12	0.13
137.00	138.31	0.18	0.21	0.52	0.25	0.14	0.18
138.00	147.07	0.21	0.19	0.27	0.21	0.12	0.15
139.00	147.07	0.19	0.14	0.24	0.13	0.14	0.13
140.00	154.15	0.20	0.18	0.26	0.20	0.08	0.17
141.00	154.15	0.21	0.17	0.25	0.19	0.14	0.10
142.00	162.65	0.22	0.18	0.29	0.19	0.11	0.12
143.00	162.65	0.19	0.16	0.28	0.16	0.08	0.10
144.00	170.48	0.19	0.17	0.28	0.17	0.12	0.08
145.00	170.48	0.21	0.16	0.21	0.15	0.08	0.11
146.00	154.15	0.18	0. 3	0.26	0.12	0.12	0.08
147.00	119.72	0.22	0.29	0.24	0.37	0.20	0.12
148.00	84.94	0.22	0.18	0.26	0.20	0.26	0.12

159

Table C.6 Standard Deviation Data No-Rotation of the Model - 8" Open Configuration

RUN DATE 20 OCT 89

OOC	FX lbf	FY lbf	FZ lbf	MX in-lbf	MY in-lbf	MZ in-lbf	Q lbf/ft^2
151.00	0.55	0.82	0.42	7.69	4.48	1.59	5.66
152.00	0.95	1.35	0.78	14.71	8.05	3.25	7.94
153.00	1.42	1.55	1.16	16.49	13.58	4.75	10.80
154.00	1.48	2.21	1.55	22.63	11.64	4.72	13.71
155.00	1.53	2.63	1.98	26.41	12.14	7.75	16.35
156.00	1.71	2.27	2.08	23.89	13.89	6.34	16.35
157.00	1.80	1.98	2.80	19.59	13.13	8.78	19.00
158.00	2.11	3.38	2.90	35.46	16.44	9.44	19.00
159.00	2.38	3.01	3.59	29.56	20.81	11.50	21.70
160.00	2.13	4.92	3.02	48.51	14.72	13.10	24.45
161.00	2.25	4.31	2.54	44.27	16.74	12.57	24.45
162.00	1.52	2.08	2.71	20.30	11.89	7.26	16.35
163.00	1.05	1.71	0.83	17.19	10.37	2.51	7.94
164.00	0.89	1.56	0.77	16.35	8.36	3.21	7.94

OOC	VEL ft/sec	CDX	CDY	CDZ	CMX	CMY	CMZ
151.00	70.32	0.22	0.33	0.17	0.38	0.22	0.08
152.00	83.34	0.27	0.38	0.22	0.52	0.29	0.12
153.00	97.22	0.30	0.32	0.24	0.43	0.35	0.12
154.00	109.58	0.24	0.36	0.26	0.46	0.24	0.10
155.00	119.76	0.21	0.36	0.27	0.45	0.21	0.13
156.00	119.76	0.24	0.31	0.29	0.41	0.24	0.11
157 00	129.15	0.21	0.23	0.33	0.29	0.19	0.13
158.00	129.15	0.25	0.40	0.34	0.53	0.24	0.14
159.00	138.09	0.25	0.31	0.37	0.38	0.27	0.15
160.00	146.65	0.20	0.45	0.28	0.56	0.17	0.15
161.00	146.65	0.21	0.40	0.23	0.51	0.19	0.14
162.00	119.76	0.21	0.29	0.37	0.35	0.20	0.12
163.00	83.34	0.30	0.48	0.23	0.61	0.37	0.09
164.00	83.34	0.25	0.44	0.22	0.58	0.30	0.11

Table C.7   Mean Data 45 Degree Rotation of the Model - Closed Configuration

RUN DATA 24 OCT 89

45C	FX lbf	FY lbf	FZ lbf	MX in-lbf	MY in-lbf	MZ in-lbf	Q lbf/ft^2
101.00	4.17	0.04	2.72	0.57	34.14	0.53	5.34
102.00	6.43	-0.47	4.24	5.11	52.54	0.80	8.19
103.00	8.64	0.46	5.58	-0.23	69.25	0.83	10.68
104.00	10.61	-0.34	7.05	6.68	85.87	0.99	13.48
105.00	13.05	-0.46	8.62	8.93	105.17	1.13	16.07
106.00	15.11	-0.33	10.00	9.44	121.14	1.21	18.98
107.00	17.59	-0.95	11.37	16.38	140.23	1.49	21.57
108.00	19.81	1.54	12.76	1.50	155.15	1.48	24.01
109.00	22.82	1.12	14.60	7.28	177.70	1.43	27.01
110.00	24.39	1.15	16.00	8.71	189.86	1.52	29.71
111.00	22.25	-0.08	14.31	15.83	174.05	1.66	27.01
112.00	13.25	-0.06	8.56	10.00	104.27	1.55	16.07
113.00	6.73	0.07	4.23	5.26	52.09	1.14	8.19

45C	VEL ft/sec	CDX	CDY	CDZ	CMX	CMY	CMZ
101.00	68.89	1.24	0.01	0.81	0.02	1.27	0.02
102.00	85.37	1.25	-0.09	0.83	0.13	1.28	0.02
103.00	97.52	1.29	0.07	0.83	-0.01	1.29	0.01
104.00	109.61	1.25	-0.04	0.83	0.10	1.27	0.01
105.00	119.74	1.29	-0.04	0.86	0.11	1.30	0.01
106.00	130.18	1.26	-0.03	0.84	0.10	1.27	0.01
107.00	138.85	1.30	-0.07	0.84	0.15	1.29	0.01
108.00	146.54	1.32	0.10	0.85	0.01	1.29	0.01
109.00	155.53	1.34	0.06	0.86	0.06	1.31	0.01
110.00	163.18	1.31	0.06	0.86	0.06	1.27	0.01
111.00	155.53	1.31	-0.01	0.84	0.12	1.28	0.01
112.00	119.74	1.32	-0.01	0.85	0.13	1.29	0.02
113.00	85.37	1.31	0.01	0.82	0.13	1.27	0.03

Table C.8 Mean Data 45 Degree Rotation of the Model - 4" Open Cavity Configuration

RUN DATE 24 OCT 89

45C	FX lbf	FY lbf	FZ lbf	MX in-lbf	MY in-lbf	MZ in-lbf	Q lbf/ft^2
116.00	5.02	0.14	1.88	0.77	34.90	0.46	5.60
117.00	7.50	0.54	2.84	-0.02	52.02	0.78	8.30
118.00	10.05	0.50	3.75	1.17	68.95	0.95	10.94
119.00	12.72	0.78	4.76	1.16	86.70	1.06	13.84
120.00	15.35	1.06	5.78	1.25	104.13	1.34	16.59
121.00	18.02	1.52	6.77	1.14	121.28	1.37	19.29
122.00	20.62	1.58	7.75	1.96	138.17	1.37	21.57
123.00	23.26	1.97	8.78	2.48	155.06	1.90	24.68
124.00	25.52	2.32	9.67	2.39	169.42	1.67	27.22
125.00	29.03	2.28	11.01	4.69	192.78	1.87	29.81
126.00	25.92	2.11	9.83	4.49	172.59	2.15	27.22
127.00	15.30	1.21	5.78	2.69	102.30	1.55	16.59
128.00	7.87	0.78	2.86	0.79	52.11	1.07	8.30

45C	VEL ft/sec	CDX	CDY	CDZ	CMX	CMY	CMZ
116.00	70.70	1.43	0.04	0.54	0.03	1.24	0.01
117.00	86.09	1.44	0.11	0.54	0.00	1.25	0.02
118.00	98.91	1.46	0.07	0.54	0.02	1.25	0.01
119.00	111.32	1.46	0.09	0.55	0.01	1.24	0.01
120.00	121.93	1.47	0.10	0.55	0.01	1.25	0.01
121.00	131.53	1.48	0.13	0.56	0.01	1.25	0.01
122.00	139.14	1.52	0.12	0.57	0.02	1.27	0.01
123.00	148.92	1.50	0.13	0.57	0.02	1.25	0.01
124.00	156.47	1.49	0.13	0.57	0.01	1.24	0.01
125.00	163.82	1.55	0.12	0.59	0.03	1.29	0.01
126.00	156.47	1.51	0.12	0.57	0.04	1.26	0.01
127.00	121.93	1.47	0.11	0.55	0.04	1.23	0.02
128.00	86.09	1.51	0.15	0.55	0.02	1.25	0.03

Table C.9 Mean Data 45 Degree Rotation of the Model - 8" Open Cavity Configuration

RUN DATE 24 OCT 89

45C	FX lbf	FY lbf	FZ lbf	MX in-lbf	MY in-lbf	MZ in-lbf	Q lbf/ft^2
131.00	5.95	0.26	1.22	0.10	34.67	0.87	5.55
132.00	8.77	0.64	1.88	-0.75	50.99	0.98	8.35
133.00	11.81	0.86	2.57	0.19	67.78	1.62	10.94
134.00	14.76	1.11	3.19	0.26	84.58	1.99	13.79
135.00	17.96	1.16	3.97	0.61	102.73	1.64	16.59
136.00	20.92	1.45	4.69	1.82	118.38	1.81	19.34
137.00	24.50	1.54	5.40	2.87	137.67	2.56	22.24
138.00	27.28	2.37	6.19	0.22	152.44	2.95	24.63
139.00	27.16	1.53	6.17	3.75	152.12	2.74	24.63
140.00	23.80	2.23	5.23	-0.23	132.79	3.03	22.24
141.00	18.02	1.31	3.76	-0.08	101.02	1.99	16.59
142.00	8.80	0.56	1.79	0.21	49.90	1.13	8.35

45C	VEL ft/sec	CDX	CDY	CDZ	CMX	CMY	CMZ
131.00	70.44	1.70	0.08	0.35	0.01	1.24	0.03
132.00	86.44	1.68	0.12	0.36	-0.02	1.22	0.02
133.00	99.00	1.72	0.13	0.37	0.00	1.23	0.03
134.00	111.22	1.71	0.13	0.37	0.01	1.22	0.03
135.00	122.04	1.73	0.11	0.38	0.01	1.23	0.02
136.00	131.83	1.73	0.12	0.39	0.01	1.22	0.02
137.00	141.45	1.75	0.11	0.39	0.03	1.23	0.02
138.00	148.90	1.76	0.16	0.40	0.00	1.23	0.02
139.00	148.90	1.75	0.10	0.40	0.03	1.23	0.02
140.00	141.45	1.70	0.16	0.37	0.00	1.19	0.03
141.00	122.04	1.73	0.13	0.36	0.00	1.21	0.02
142.00	86.44	1.68	0.11	0.34	0.01	1.19	0.03

Table C.10 Standard Deviation Data 45 Degree Rotation of the Model - Closed Configuration

RUN DATE 24 OCT 89

45C	FX lbf	FY lbf	FZ lbf	MX in-lbf	MY in-lbf	MZ in-lbf	Q lbf/ft^2
101.00	0.59	0.58	0.47	5.08	4.94	0.81	5.34
102.00	0.57	0.55	0.90	4.85	4.28	1.04	8.19
103.00	0.94	1.16	1.36	9.62	8.71	1.43	10.68
104.00	1.01	1.13	1.01	9.89	9.18	1.64	13.48
105.00	0.95	1.22	1.75	11.15	8.20	2.38	16.07
106.00	1.03	1.41	4.59	12.00	8.22	4.09	18.98
107.00	1.14	1.63	3.22	13.35	9.02	2.62	21.57
108.00	1.26	2.55	2.15	20.04	9.48	4.09	24.01
109.00	1.95	3.31	2.08	26.50	16.89	2.99	27.01
110.00	1.47	2.77	3.36	22.32	11.18	4.08	29.71
111.00	1.47	2.67	2.13	20.34	11.13	3.17	27.01
112.00	1.04	1.36	1.46	11.52	8.87	2.32	16.07
113.00	0.57	0.59	0.60	5.19	4.51	1.21	8.19

45C	VEL ft/sec	CDX	CDY	CDZ	CMX	CMY	CMZ
101.00	68.89	0.18	0.17	0.14	0.19	0.18	0.03
102.00	85.37	0.11	0.11	0.18	0.12	0.11	0.03
103.00	97.52	0.14	0.18	0.21	0.18	0.16	0.03
104.00	109.61	0.12	0.13	0.12	0.15	0.13	0.02
105.00	119.74	0.09	0.12	0.18	0.14	0.10	0.03
106.00	130.18	0.08	0.12	0.38	0.13	0.08	0.04
107.00	138.85	0.08	0.12	0.24	0.12	0.08	0.02
108.00	146.54	0.08	0.17	0.14	0.17	0.08	0.04
109.00	155.53	0.11	0.20	0.12	0.20	0.13	0.02
110.00	163.18	0.08	0.15	0.18	0.15	0.08	0.03
111.00	155.53	0.08	0.16	0.13	0.15	0.08	0.02
112.00	119.74	0.11	0.13	0.14	0.14	0.11	0.03
113.00	85.37	0.11	0.11	0.12	0.13	0.11	0

Table C.11   Standard Deviation Data45 Degree Rotation of the Model
- Open 4" Configuration

RUN DATE 24 OCT 89

45C	FX lbf	FY lbf	FZ lbf	MX in-lbf	MY in-lbf	MZ in-lbf	Q lbf/ft^2
116.00	0.05	0.42	0.49	4.03	3.78	1.22	5.60
117.00	0.71	0.63	0.87	5.76	5.53	1.82	8.30
118.00	0.98	0.74	0.91	6.06	8.74	4.04	10.94
119.00	1.25	1.20	1.22	11.50	11.28	5.22	13.84
120.00	1.70	1.57	2.12	15.89	15.29	7.27	16.59
121.00	1.63	1.75	3.08	14.67	11.67	9.66	19.29
122.00	1.47	1.70	3.44	12.07	8.47	12.12	21.57
123.00	1.78	1.82	3.06	12.62	12.01	8.85	24.68
124.00	1.95	1.85	3.20	11.05	10.16	8.36	27.22
125.00	2.50	2.56	3.68	20.41	15.41	8.78	29.81
126.00	2.20	2.35	2.71	16.23	10.37	9.49	27.22
127.00	1.23	1.25	2.20	10.97	9.56	5.66	16.59
128.00	0.74	0.68	0.95	6.73	6.20	2.22	8.30

45C	VEL ft/sec	CDX	CDY	CDZ	CMX	CMY	CMZ
116.00	70.70	0.01	0.12	0.14	0.14	0.13	0.04
117.00	86.09	0.13	0.12	0.17	0.14	0.13	0.04
118.00	98.91	0.14	0.11	0.13	0.11	0.16	0.08
119.00	111.32	0.14	0.13	0.14	0.16	0.16	0.08
120.00	121.93	0.16	0.15	0.21	0.19	0.18	0.08
121.00	131.53	0.13	0.14	0.25	0.15	0.12	0.10
122.00	139.14	0.11	0.13	0.25	0.11	0.08	0.11
123.00	148.92	0.11	0.12	0.20	0.10	0.10	0.08
124.00	156.47	0.11	0.11	0.18	0.08	0.08	0.06
125.00	163.82	0.13	0.13	0.20	0.13	0.11	0.06
126.00	156.47	0.13	0.13	0.16	0.12	0.08	0.08
127.00	121.93	0.12	0.12	0.21	0.13	0.11	0.08
128.00	86.09	0.14	0.13	0.18	0.16		

Table C.12   Standard Deviation Data 45 Degree Rotation of the Model
- Open 8" Configuration

RUN DATE 24 OCT 89

45C	FX lbf	FY lbf	FZ lbf	MX in-lbf	MY in-lbf	MZ in-lbf	Q lbf/ft^2
131.00	0.78	0.99	0.53	8.40	7.66	2.01	5.55
132.00	0.83	1.34	0.89	9.46	7.38	4.84	8.35
133.00	1.27	1.46	1.20	10.64	11.66	5.75	10.94
134.00	0.96	2.05	1.20	13.68	6.23	7.66	13.79
135.00	1.56	2.80	1.68	18.32	12.35	9.21	16.59
136.00	2.00	3.28	2.65	23.01	16.99	8.02	19.34
137.00	1.90	4.38	2.99	29.04	14.68	9.92	22.24
138.00	3.07	4.59	2.79	32.88	26.72	9.13	24.63
139.00	2.41	4.59	2.97	27.78	19.44	13.75	24.63
140.00	2.12	3.82	3.09	26.38	17.42	14.38	22.24
141.00	1.76	3.10	1.82	21.24	14.96	7.84	16.59
142.00	0.69	1.35	0.85	9.16	5.48	4.81	8.35

45C	VEL ft/sec	CDX	CDY	CDZ	CMX	CMY	CMZ
131.00	70.44	0.23	0.28	0.16	0.30	0.28	0.08
132.00	86.44	0.16	0.25	0.17	0.23	0.18	0.11
133.00	99.00	0.18	0.21	0.18	0.19	0.21	0.11
134.00	111.22	0.11	0.23	0.14	0.20	0.09	0.11
135.00	122.04	0.15	0.27	0.16	0.22	0.15	0.11
136.00	131.83	0.16	0.27	0.22	0.23	0.18	0.08
137.00	141.45	0.13	0.31	0.21	0.27	0.13	0.09
138.00	148.90	0.20	0.30	0.18	0.28	0.22	0.08
139.00	148.90	0.16	0.30	0.19	0.23	0.16	0.11
140.00	141.45	0.15	0.28	0.22	0.23	0.16	0.13
141.00	122.04	0.17	0.30	0.18	0.25	0.18	0.09
142.00	86.44	0.13	0.25	0.16	0.22	0.13	

Table C.13
Frequency Response Summary No-Rotation, Closed Cavity

Data Pt. 00C_ _ _	Local Vel. (ft/s)	Side Load Frequency (F_y)		Z-Moment Frequency (Mz)	
		Frequency (Hz)	Spectrum Magnitude	Frequency (Hz)	Spectrum Magnitude
117	68.5	12	0.3880	88	0.655
		16	0.2080	90	0.615
		22	0.1580		
118	86.7	15	0.7490	86	1.5780
		21	0.4320		
119	97.2	18	1.7210	87	2.9570
		21	1.0270		
120	108.3	19	3.6210	87	2.4860
		21	2.9550	21	0.6370
121	118.6	20	10.1278	87	4.5790
		21	4.4480	20	1.3520
122	118.6	19	3.2430	20	3.4900
		20	6.7416	87	0.8515
		21	2.9900	20	3.4900
123	108.3	17	1.1800	87	4.9090
		19	2.4000		
124	97.2	16	1.2600	88	1.830
		21	1.2200		
125	86.7	15	0.9900	88	1.590
		22	0.5740		
126	68.5	6	0.2690	90	0.466
		11	0.2330	426	0.462
		22	0.1750		

167

Table C.14
Frequency Response Summary No-Rotation, 4" Open Cavity

Data Pt. 00C_ _ _	Local Vel. (ft/s)	Side Load Frequency (F_y)		Z-Moment Frequency (Mz)	
		Frequency (Hz)	Spectrum Magnitude	Frequency (Hz)	Spectrum Magnitude
129	70.8	21	0.5440	86	1.98
130	84.9	19	0.3500	89	3.240
		22	0.4700		
		155	0.2200		
131	98.4	21	0.8120	87	4.930
		157	0.2800		
132	109.0	20	0.7310	87	11.670
		157	0.2400		
133	119.7	21	1.6800	87	10.000
134	129.3	21	1.5800	86	12.820
		161	0.4100		
135	129.3	21	1.1450	88	12.720
		159	0.594		
136	138.3	22	1.2700	86	10.510
		159	0.4420		
137	138.3	20	1.7800	87	14.190
		157	0.4200		
138	147.1	21	1.8300	87	11.500
		159	0.4560		
139	147.1	21	1.0700	86	8.410
		156	0.3800		
140	154.2	21	1.9500	87	13.08
		158	0.9300		
141	154.2	21	1.6200	87	9.480
		161	0.4700		
142	162.6	21	2.2800	87	10.770
		156	0.7600		
143	162.6	21	1.4140	85	7.700
		159	0.6810		

Table C.14 (Cont.)
Frequency Response Summary No-Rotation, 4" Open Cavity

Data Pt. 00C_ _ _	Local Vel. (ft/s)	Side Load Frequency (F_y)		Z-Moment Frequency (Mz)	
		Frequency (Hz)	Spectrum Magnitude	Frequency (Hz)	Spectrum Magnitude
144	170.5	21	1.4300	88	7.976
		157	0.9330		
145	170.5	21	1.0300	86	11.340
		160	0.8800		
146	154.2	21	0.8800	88	4.560
		158	0.5300		
147	119.7	22	1.8120	86	4.460
		151	0.3800		
		161	0.2900		
148	84.9	22	0.3860	87	2.880
		159	0.1690		

Table C.15
Frequency Response Summary No-Rotation, 8" Open Cavity

Data Pt. 00C_ _ _	Local Vel. (ft/s)	Side Load Frequency (F_y)		Z-Moment Frequency (Mz)	
		Frequency (Hz)	Spectrum Magnitude	Frequency (Hz)	Spectrum Magnitude
151	70.3	13	0.2800	87	0.9455
		21	0.7600		
152	83.3	21	1.1000	88	1.9800
153	97.2	22	1.4900	89	3.8100
154	109.6	21	1.4900	85	2.0400
155	119.8	13	0.9600	87	6.4260
		22	2.3500		
156	119.8	21	1.6500	85	4.6800
157	129.2	22	1.3100	87	5.4000
		159	0.3900		
158	129.2	21	4.1400	88	5.5300
159	138.1	20	2.2000	87	11.5200
		159	0.4100		
160	146.6	22	3.2500	87	10.6400
161	146.6	21	4.9800	87	9.6100
162	119.7	20	1.6400	86	5.1000
163	83.3	21	1.3900	88	1.5700
164	83.3	20	1.1500	87	2.3100

Table C.16
Frequency Response Summary 45 Degree Rotation, Closed Cavity

Data Pt. 45C_ _ _	Local Vel. (ft/s)	Side Load Frequency (F_y)		Z-Moment Frequency (Mz)	
		Frequency (Hz)	Spectrum Magnitude	Frequency (Hz)	Spectrum Magnitude
101	68.9	1	0.5750	89	0.36
		24	0.3950	406	0.46
102	85.4	3	0.4550	87	0.60
		20	0.2130	405	0.51
		22	0.1890		
		152	0.0780		
103	97.5	1	1.1030	86	0.63
		22	0.5110	91	0.65
104	109.6	4	0.7350	88	1.29
		25	0.4700		
		153	0.3060		
105	119.7	3	0.5190	85	1.59
		8	0.4900		
		22	0.5600		
		141	0.1850		
106	130.2	1	1.0000	92	3.03
		5	0.5700		
		24	0.6170		
107	138.8	8	0.7690	89	1.49
		22	0.7160		
108	146.5	3	2.3800	88	4.26
		21	1.1100		
109	155.5	1	2.9800	87	1.81
		23	1.5400		
110	163.2	1	1.8500	89	2.99
		24	1.2200		
111	155.5	2	1.4400	88	2.56
		22	0.7810		
112	119.7	1	0.5800	88	1.81
		4	0.5900		
		25	0.6100		
113	85.4	2	0.3150	89	1.04
		25	0.3180		

171

Table C.17
Frequency Response Summary 45 Degree Rotation, 4" Open Cavity

Data Pt. 45C_ _ _	Local Vel. (ft/s)	Side Load Frequency (F_y)		Z-Moment Frequency (Mz)	
		Frequency (Hz)	Spectrum Magnitude	Frequency (Hz)	Spectrum Magnitude
116	70.7	2	0.1700	88	0.826
		4	0.1700		
		21	0.2400		
		25	0.2000		
		151	0.0900		
117	86.1	19	0.3350	87	1.32
		22	0.4670		
		151	0.1310		
118	98.9	4	0.2260	89	4.14
		20	0.3160		
		25	0.4510		
		153	0.1700		
		159	0.2300		
119	111.3	22	0.8900	88	4.80
		25	0.6700		
		155	0.3650		
120	121.9	21	0.6600	88	6.45
		25	0.9700		
		152	0.5800		
121	131.5	22	0.9920	89	8.74
		153	0.5140		
122	139.1	22	1.2230	88	12.11
		150	0.5000		
123	148.9	7	0.5440	88	8.21
		24	0.9728		
		150	0.5900		
124	156.5	4	0.4510	88	8.56
		24	0.6220		
		150	0.8389		
125	163.8	23	1.8200	88	6.96
		149	0.9600		
126	156.5	23	1.3130	89	9.69
		150	1.2170		

Table C 17 (Cont.)
Frequency Response Summary 45 Degree Rotation, 4" Open Cavity

Data Pt. 45C_ _ _	Local Vel. (ft/s)	Side Load Frequency (F_y)		Z-Moment Frequency (Mz)	
		Frequency (Hz)	Spectrum Magnitude	Frequency (Hz)	Spectrum Magnitude
127	121.9	6	0.4740	86	3.90
		22	0.6210		
		155	0.3790		
128	86.1	25	0.4970	88	2.26
		152	0.1620		

173

Table C 18 (Cont.)
Frequency Response Summary 45 Degree Rotation, 8" Open Cavity

Data Pt. 45C_ _ _	Local Vel. (ft/s)	Side Load Frequency (F_y)		Z-Moment Frequency (Mz)	
		Frequency (Hz)	Spectrum Magnitude	Frequency (Hz)	Spectrum Magnitude
141	122.9	7	2.6300	88	6.05
		21	1.0000		
		25	1.1300		
		153	0.3850		
142	86.4	4	1.0500	87	3.83
		21	0.4300		
		155	0.1400		

Table C.18
Frequency Response Summary 45 Degree Rotation, 8" Open Cavity

Data Pt. 45C_ _ _	Local Vel. (ft/s)	Side Load Frequency (F_y)		Z-Moment Frequency (Mz)	
		Frequency (Hz)	Spectrum Magnitude	Frequency (Hz)	Spectrum Magnitude
131	70.4	3	0.6800	88	1.50
		25	0.5700		
132	86.4	3	0.8700	89	4.36
		8	0.5300		
		21	0.4500		
133	99.0	4	0.8400	88	4.64
		7	0.6900		
		21	0.4800		
		26	0.5300		
134	111.2	6	1.3500	89	5.83
		3	1.1800		
		21	0.6400		
		155	0.4900		
135	122.0	6	1.4300	88	9.05
		24	0.9400		
		153	0.4000		
136	131.8	6	2.0000	87	5.02
		22	1.3100		
		150	0.7700		
137	141.4	7	2.9400	88	8.15
		22	1.6600		
		151	0.39		
138	148.9	8	2.8700	86	5.59
		20	1.6300		
		24	1.5200		
139	148.9	5	2.5000	89	10.61
		8	2.5100		
		14	1.5100		
		22	1.0300		
		151	1.0000		
140	141.4	5	2.0100	88	15.37
		21	1.4400		
		154	0.5100		
		150	1.2170		

Vita

Captain Brian W. King ████████████████████████████████████
████████ the third son of ████████████████████████ He
graduated from Red Land High School, in Lewisberry, Pennsylvania in June
1980. The following September, Captain King matriculated at the Penn-
sylvania State University, State College, Pennsylvania with a four year
ROTC scholarship. He graduated from PSU on 19 May 1984 with a Bachelor
of Science degree in Aerospace Engineering and was recognized as a dis-
tinguished graduate in ROTC. On the same day, he was commissioned a
Second Lieutenant of the United States Air Force. His first assignment,
before entering AFIT was at the Aero-Propulsion Laboratory at Wright-
Patterson AFB, OH. He also completed Squadron Officers School in resi-
dence in March 1988. His new bride, whom he married in December 1988, is
the former ██

REPORT DOCUMENTATION PAGE

1a. REPORT SECURITY CLASSIFICATION UNCLASSIFIED	1b. RESTRICTIVE MARKINGS
2a. SECURITY CLASSIFICATION AUTHORITY	3. DISTRIBUTION/AVAILABILITY OF REPORT Approved for Public Realease; Distribution Unlimited
2b. DECLASSIFICATION/DOWNGRADING SCHEDULE	
4. PERFORMING ORGANIZATION REPORT NUMBER(S) AFIT/GAE/ENY/89D-19	5. MONITORING ORGANIZATION REPORT NUMBER(S)

6a. NAME OF PERFORMING ORGANIZATION School of Engineering	6b. OFFICE SYMBOL (If applicable) AFIT/ENY	7a. NAME OF MONITORING ORGANIZATION
6c. ADDRESS (City, State, and ZIP Code) Air Force Institute of Technology Wright-Patterson Air Force Base, OH 45433		7b. ADDRESS (City, State, and ZIP Code)

8a. NAME OF FUNDING/SPONSORING ORGANIZATION Air Force Weapons Laboratory	8b. OFFICE SYMBOL (If applicable) AFWL/ARDC	9. PROCUREMENT INSTRUMENT IDENTIFICATION NUMBER

8c. ADDRESS (City, State, and ZIP Code) AFWL/ARDC Kirtland Air Force Base NM 87117	10. SOURCE OF FUNDING NUMBERS			
	PROGRAM ELEMENT NO.	PROJECT NO.	TASK NO	WORK UNIT ACCESSION NO.

11. TITLE (Include Security Classification)

Fluctuating Wind Forces Measured on a Bluff Body Extending from a Cavity

12. PERSONAL AUTHOR(S)
Brian W. King, CAPT, USAF

13a. TYPE OF REPORT MS Thesis	13b. TIME COVERED FROM _____ TO _____	14. DATE OF REPORT (Year, Month, Day) 1989 December	15. PAGE COUNT 196

16. SUPPLEMENTARY NOTATION

17. COSATI CODES			18. SUBJECT TERMS (Continue on reverse if necessary and identify by block number)
FIELD	GROUP	SUB-GROUP	Bluff bodies Vortex Shedding Wind effects
01	01		Fluid-solid interaction Vibration
14	02		Dynamic structures Subsonic Wind Tunnels

19. ABSTRACT (Continue on reverse if necessary and identify by block number)

Thesis Advisor: Lt Col Paul I. King
                   Assistant Professor
                   Department of Aeronautics and Astronautics

20. DISTRIBUTION/AVAILABILITY OF ABSTRACT ☒ UNCLASSIFIED/UNLIMITED ☐ SAME AS RPT. ☐ DTIC USERS	21. ABSTRACT SECURITY CLASSIFICATION UNCLASSIFIED
22a. NAME OF RESPONSIBLE INDIVIDUAL Paul I. King, Assistant Professor	22b. TELEPHONE (Include Area Code) (513) 255-2362 22c. OFFICE SYMBOL AFIT/ENY

DD Form 1473, JUN 86   *Previous editions are obsolete.*

Abstract

The effect of wind forces measured on a bluff body extending from a cavity was investigated. This was accomplished by measuring wind induced vibratory inputs to a plexiglas bluff body model. The model extended from a ground board cavity installed in the AFIT 5-Foot Wind Tunnel.

Forces and moments were measured from an 8 element load cell unit (LCU) built and installed in the base of a plexiglas model. Three different size cavity openings were tested for both a no-rotation and 45 degree rotation referenced to the wind. Data was taken at individual speed points between 55 ft/s and 180 ft/s, producing Reynolds number based on model width in the range of 1.5×10^5 to 5.0×10^5. Baseline data for a closed cavity configuration was collected and compared to previous studies conducted at the USAF Academy. Force and moment coefficient data are presented, comparing cavity opening and model rotation effects. Results of shedding frequency analysis are presented based on transient data recorded.